Optical characterization of luminescent silicon nanocrystals embedded in glass matrices

Dissertation

zur Erlangung des akademischen Grades
doctor rerum naturalium (Dr. rer. nat.)

vorgelegt dem Rat der Physikalisch-Astronomischen Fakultät
der Friedrich-Schiller-Universität Jena

von Diplomphysiker Olivier Debieu
geboren am 19. März 1975 in Avranches, Frankreich

Gutachter

1. Prof. Dr. Friedrich Huisken, Friedrich-Schiller Universität Jena.
2. Prof. Dr. Rob Elliman, the Australian National University, Canberra.
3. Prof. Dr. Blas Garrido, Universitat de Barcelona.

Tag der letzten Rigorosumsprüfung: 9. 12. 2008
Tag der öffentlichen Verteidigung: 16. 12. 2008

1. Introduction

Interstellar dust in nebulae and in the Diffuse Interstellar Medium (DISM) of galaxies contains a component which exhibits efficient visible-near infrared luminescence ranging from 500 to 1000 nm, known as Extended Red Emission (ERE). The ERE, which was first detected by Cohen *et al.*[1] in the spectrum of the Red Rectangle nebula more than 30 years ago, generally appears as a broad structureless emission band. The ERE has been observed in many different dusty environments that are illuminated by ultraviolet photons. Therefore, this Vis-NIR emission is probably due to the interaction of ultraviolet photons with dust grains through photoluminescence (PL). The ERE carrier is a component of interstellar dust that must consist of the most abundant refractive elements in the cosmos (C, O, Si, Fe and Mg), and, once formed, the carrier must survive under a wide range of astrophysical conditions.

Silicon nanocrystals (nc-Si) are discussed as possible carriers of the ERE.[2, 3] Indeed, nc-Si can emit intense PL in a wide spectral range from 600 to 1100 nm. Interestingly, the emission energy depends on the nanoparticle size. This effect has been explained by the quantum confinement model proposed first by Canham.[4, 5] Ledoux *et al.*[2] have shown that the properties of the PL of free oxygen-passivated nc-Si could satisfy the observational constraints of the ERE in terms of spectral variability and luminescence yield. However, the recent model calculations of Li and Draine[6] revealed that heated (~100 K) free-flying oxygen-passivated nc-Si should give rise to an emission feature around 20 μm, which in fact is not observed in ERE regions. A possibility to overcome this objection is to assume that the oxygen-passivated nc-Si are not free nanoparticles, but instead attached to or embedded in larger grains of some other material, as for instance, silicates which have already been identified in space.[7, 8, 9] Another way to overcome the objection of Li and Draine is to consider other forms of passivation.

As has been shown by several authors,[10, 11, 12, 13, 14] nc-Si embedded in SiO_2 (nc-Si/SiO_2) reveal strong PL. Ion implantation is a promising technique to produce nanoparticles in solid matrices. We employed the accelerator facilities of the Institute of Solid State Physics of the University of Jena to implant Si ions into fused silica windows. An excess concentration of silicon atoms is thus produced in the host SiO_2 matrix which, by applying an annealing at 1100 °C, condensates to silicon nanoparticles and crystallizes. Although the condensation and crystallization occur after an annealing of one minute,[10, 15] the samples were annealed during one hour in order to well-passivate the nc-Si, that means, to reduce effectively the number of Si-dangling bonds at the nc-Si surface that are efficient non-radiative recombination centers.[10, 16] Upon excitation with UV light, most of our nc-Si/SiO_2 samples revealed strong PL.

We implanted into our luminescent nc-Si/SiO_2 systems other atomic elements, as for instance magnesium and calcium, which form silicates if their oxide is combined with SiO_2. The purpose is to simulate the conditions for silicates containing nc-Si. In order to understand the effect of the incorporation of foreign atoms on the PL properties of our nc-Si/SiO_2 systems, we proceeded to similar experiments with Er and Ge. As has been demonstrated by several authors,[17, 18] the presence of nc-Si in a glass matrix enhances considerably the emission of Er^{3+} ions at 1.536 μm. At the same time, the PL of nc-Si is considerably quenched. Since the solu-

bility of Er in crystalline silicon is about 2 orders of magnitude lower than in SiO_2,[19] the optically active Er^{3+} ions are believed to be localized outside the nc-Si core, demonstrating that ions present in the host SiO_2 matrix influence the PL properties of embedded nc-Si. Proceeding to Ge implantation, we are convinced to synthesize for the first time luminescent alloy nc-$Si_{1-x}Ge_x$ with this technique. Taking into account this result, one can reasonably put forward the assumption that not only pure nc-Si can exhibit PL.

In the following chapter, an overview of the astrophysical aspect of this work is given. It concerns the characteristics of the ERE and the constraints for its possible carriers, as well as the properties of photoluminescence of nc-Si, the origin of which is still controversely discussed (quantum confinement or interface defects). Interestingly, the size dependence of the PL, which is predicted by the quantum confinement model, appears to depend on the synthesis techniques.

Chapter 4 deals with the optical and structural properties of free O-passivated nc-Si and nc-Si/SiO_2 systems synthesized by laser pyrolysis of silane and ion implantation, respectively. We were particularly interested in the formation nc-Si/SiO_2 systems and their PL properties, the purpose of which is to obtain efficient luminescent samples into which additional atomic elements will be incorporated.

In the last chapter, we focus on the effect of the incorporation of additional atomic elements into our nc-Si/SiO_2 systems on their optical properties. Motivated by the desire to synthesize luminescent alloy nc-$Si_{1-x}Ge_x$, we also applied our incorporation procedure to Ge.

2. State of the art

In the first part of this chapter, which concerns the astrophysical aspect of this work, an overview of the Extended Red Emission (ERE) is reported, as well as the candidates of its carriers, including silicon nanocrystals (nc-Si), which have also been proposed to explain spectroscopic observations of the inner corona of the sun. The second part deals with the photoluminescence (PL) of nc-Si, its origins, and, in order to debate about the size dependence of the PL of nc-Si, the various nc-Si synthesis methods will be summarized.

2.1. Astrophysical aspect

2.1.1. Extended Red Emission

Interstellar dust in nebulae and in the Diffuse Interstellar Medium (DISM) of galaxies contains a component which responds to ultraviolet photons radiation with efficient Vis-NIR luminescence ranging from 500 to 1000 nm, known as ERE. In 1975, Cohen et al.[1] detected first the broad luminescence band in the spectrum of the Red Rectangle nebula, which was followed by the observations of Schmidt et al.,[20] who suggested that a molecular emission could be on the origin for the broad band of excess radiation. ERE is a common phenomenon observed in many objects containing dusty environments that are illuminated by UV photons. Detections of the ERE in reflection nebulae (NGC 2023, NGC 7023, NGC 2247, and NGC 7035)[21, 22, 23], has been followed by the discovery of the presence of ERE in the continuum spectrum of planetary nebulae (NGC 7027 and NGC 6790).[24, 25] Similar spectral features have also been detected in spectroscopic measurements performed in the HII regions of the Orion nebula,[26] in the Bubble nebula (NGC 7635),[27] in the 30 Doradus nebula in the Large Magellanic Clouds,[28] and more recently in the HII region Sh 152.[29] The ERE has been detected in other external galaxies include the halo of M82[30] and in the Evil Eye galaxy (NGC 4826).[31]The detection of ERE in the DISM of the Milky Way Galaxy[32] demonstrated that the ERE carrier is a component of interstellar dust that is present in a wide range of astrophysical conditions. A good overview of the ERE properties may be found in the article of Witt et al.[3] and in the more recent review of Witt and Vijh.[33]
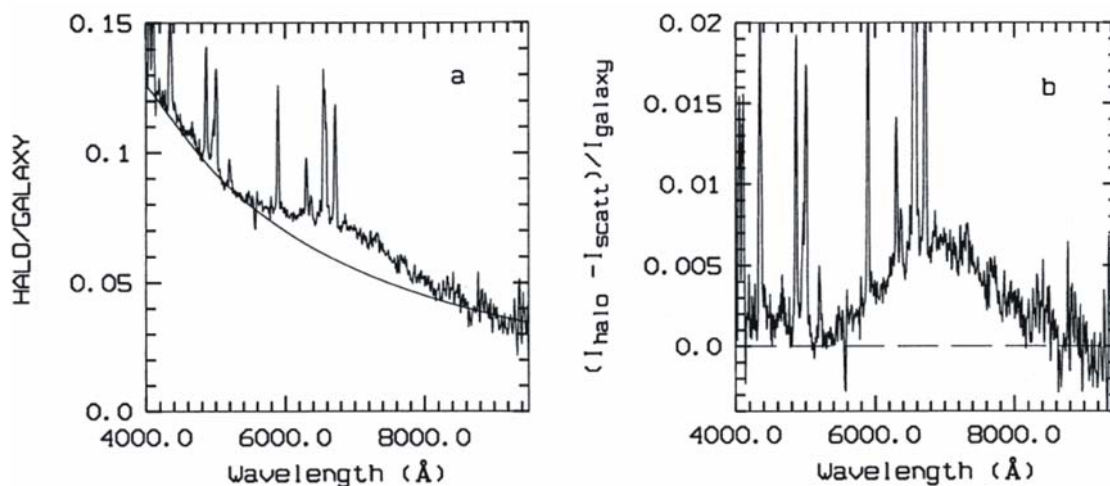
Fig. 2.1. Extended red emission observed in a galaxy of the halo of M82 according to Perrin et al.[30] a) The spectrum is well fitted in its blue and red part by a scattering continuum. b) The ERE is obtained by subtracting the calculated scattering continuum from the observed spectrum.
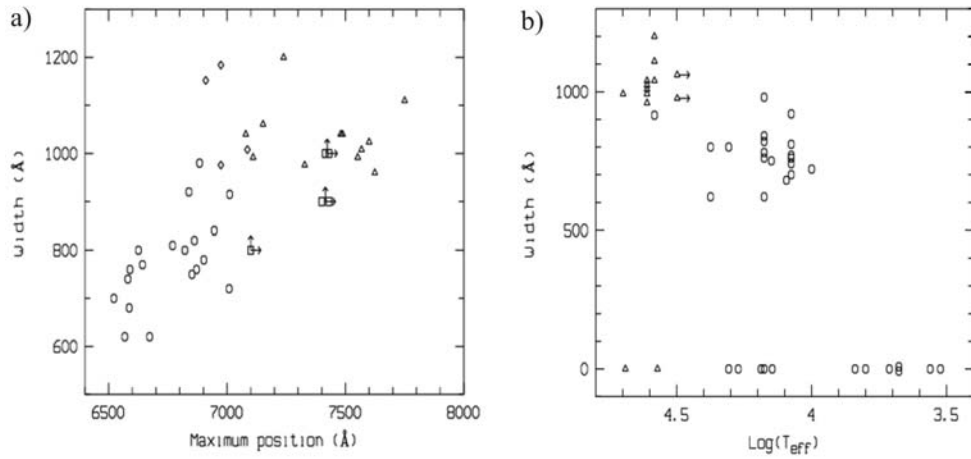
Fig. 2.2. a) Position of the maximum emission spectrum versus the width of the ERE band for a number of objects of various types: HII regions (Δ),[26, 27, 28, 29] planetary nebulae (□),[25] reflection nebulae (○),[22] and the halo of M82 (◊).[30] b) Width of the ERE band as a function of the logarithm of the effective temperature of the exciting and/or illuminating star as measured on HII regions (Δ) and reflection nebulae (○), according to Darbon *et al.*[34]

2.1.1.1. Characteristics of the ERE

The ERE generally appears as a broad structureless emission band of excess of radiation superposed on a scattering continuum, as it is shown in Fig. 2.1 according to the measurements of Perrin *et al.*[30] of the halo of M82. The position of the maximum of the band varies from source to source and within a given source ranging from 600 to 850 nm (see Fig. 2.2 and Fig. 2.3). The full width at half maximum of the ERE bands is found to change from 120 to 210 nm. This corresponds to a range from 60 to 120 nm if we consider the width in which half of the total PL energy is concentrated. As it has been demonstrated by the analysis of various objects by Darbon *et al.*,[34] the bandwidth increases with the position of the maximum of the band (see Fig. 2.2.a). The authors also showed that only environments illuminated by near stars with temperature color $T_{eff} \geq 7000$ K exhibited ERE, while sources with illuminating stars with lower temperature color did not (see Fig. 2.2.b). This result suggests that photons with energies $E \geq 7.25$ eV ($\lambda \leq 170$ nm), which corresponds to the approximate UV-cut-off of $T_{eff} = 7000$ K, are required for ERE excitation. This result is supported by the preceding observations of Witt and Schild[35] who found a correlation between the UV absorption occurring at wavelength
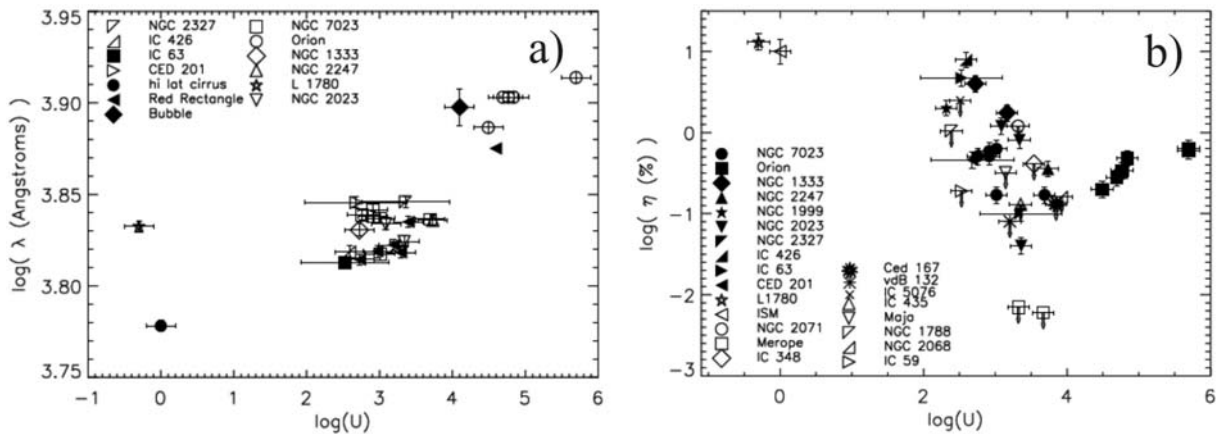
Fig. 2.3. a) Peak wavelength of ERE for a variety of sources plotted as a function of radiation field density which are normalized to the reference value $U_{ref} = 9.7 \ 10^{14}$ ergs/cm^3. b) ERE efficiency plotted as a function of the radiation field density according to Smith and Witt.[36]

$\lambda \leq 150$ nm and the ERE process. In nebulae where ERE is observed, peak of the ERE band shifts to longer wavelengths with increasing density of the local far-ultraviolet radiation field (see Fig.2.3.a).[36] In addition, photon conversion efficiency decreases strongly with increasing density of the UV radiation field (see Fig.2.3.b).[36] The maximal photon conversion efficiency of the luminescence process leading to ERE has been detected under low radiation density conditions in the DISM.[32].This yield approached 10%.

2.1.1.1. Silicon nanocrystals as carriers of the ERE?

Carriers of the PL that leads to the ERE must consist of the most abundant refractory elements in the cosmos that are able to form photoluminescent materials. Such elements include C, O, Si, Fe, and Mg. The atomic abundances of the solar system are plotted in Fig. 2.4. Hydrogenated amorphous carbons were first believed to be responsible for the ERE but it seems finally that they cannot reproduce simultaneously the spectral features and the photon conversion efficiencies of the ERE.[37] Since PAH molecules are considered likely candidates to explain the unidentified emission bands in the DISM in which ERE is observed as well, they have been proposed as possible source of the ERE. However, PAH exhibit luminescence predominantly in the optical spectra ranging from 300 to 600 nm where no emission in the DISM has been detected.

nc-Si have emerged as an interesting alternative to the carbonaceous carriers to explain the ERE. They have been first proposed by Ledoux *et al.*[2] and later strongly supported by Witt *et al.*[3] Recently, our laboratory studies on oxygen-passivated free silicon nanocrystals have shown that all ERE spectra known so far can be perfectly matched by laboratory spectra, suggesting that nc-Si are responsible for this astrophysical luminescence phenomenon.[37] However, in their recent model calculations Li and Draine[6] revealed that free-flying oxygen-passivated Si nanocrystals should give rise to an emission feature around 20 µm, which in fact is not observed in ERE regions (see Fig. 2.5). This objection may be overcome if silicon nanoparticles are either agglomerated or embedded in larger grains of some other material. Indeed, it has been several times experimentally demonstrated that the production of nc-Si embedded in SiO_2
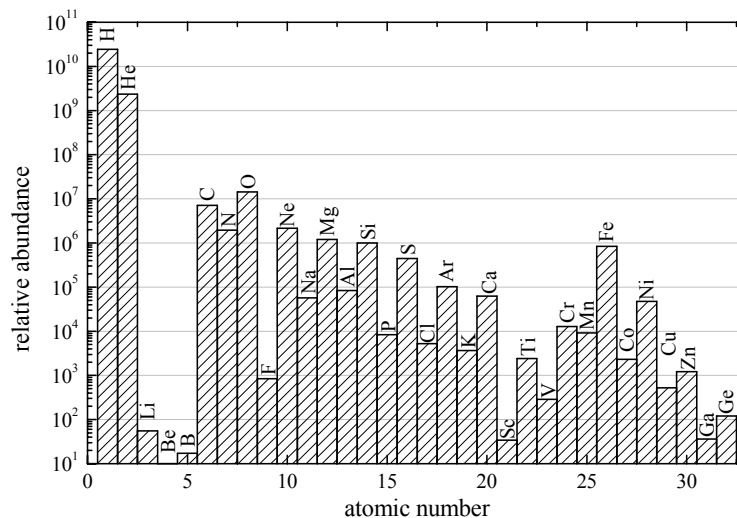
Fig. 2.4. Relative atomic abundances of the 32 first elements of the periodic table of the solar system according to Lodders.[38] Atomic abundances are normalized to the number of silicon atoms of $N(Si)=10^6$.
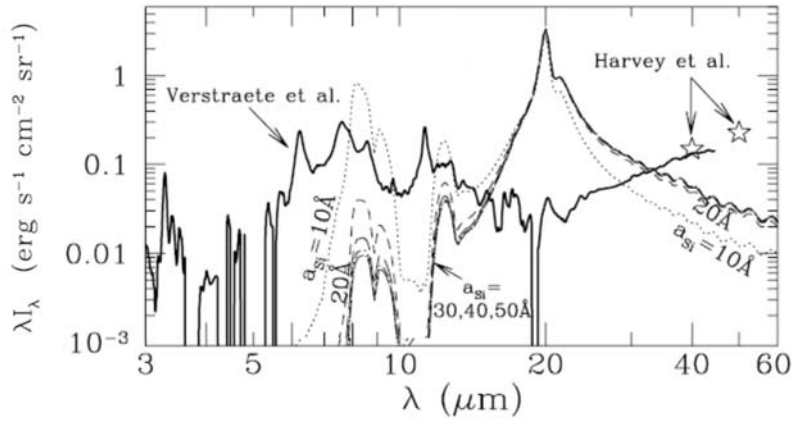
Fig. 2.5. Predicted IR emission spectra for neutral nc-Si/SiO$_2$ grains containing Si/H = 15 ppm, for various values of the Si core radius a_{Si} (a_{Si} = 0.8 $a_{core+shell}$) of 20, 30, 40, and 50 Å according to Li and Draine.[6] Spectra for a_{Si} = 30, 40, and 50 Å are nearly indistinguishable. For comparison the authors showed astronomical observations: ISO SWS spectrum (*Heavy solid line*) and KAO photometry (*Stars*).

by either ion implantation,[10] plasma-enhanced chemical vapor deposition,[39] sputtering,[40] or reactive evaporation of SiO[13] leads to strong PL ranging from 710 to 1100 nm (see Sec. 2.2.4. and Sec. 4.2.1.7.). Another way to overcome the objection of Li and Draine is to consider other forms of passivation, in particular by hydrogen.

Furthermore, the ERE carriers should be associated with a few micrometers-sized grains or larger grains since the ERE is observed in absence of scattering.[33]

In their study on the synthesis of nc-Si in phosphosilicate glasses synthesized by sputtering technique, Fujii *et al.*[41] observed an enhancement of the PL with the increasing of the phosphorus concentration. Further experiments revealed *a contrario* that the PL is significantly quenched for higher concentrations of phosphorus.[42] This behaviour – enhancement with lower concentrations of P and quenching with higher concentrations of P – has been also observed on samples produced by ion implantation.[43, 46] An explanation of the enhancement of the PL has been partly given by electron spin resonance measurements, which proves that P atoms passivate the nc-Si by reducing the number of silicon dangling bonds at the nanoparticle surface, while the PL quenching is explained by the inclusion of foreign atoms in the nc-Si volume, which is supposed to inhibit seriously the PL.[41, 45] However, Kachurin *et al.*[44] suggested that, at lower concentrations, impurities contribute to the promotion of crystallisation of nc-Si and thus improve the luminescence, whereas, at higher concentrations, inclusion of foreign atoms is on the origin of structural imperfections that quench the luminescence. Anyway, only a few studies have been carried on the doping impurities in nc-Si/SiO$_2$ systems, which represent a new investigation field for the understanding of luminescence properties of nc-Si. However, they rarely concerned atomic elements that have a relevant astrophysical aspect. One can notice that a similar behavior of the PL intensity has been observed for nc-Si/SiO$_2$ doped with CeF$_3$,[46] and for nc-Si embedded in indium doped SiO$_2$,[47] whereas boron atoms seems to only quench the luminescence.[42, 46] However, it has been demonstrated that it is possible to recover the PL intensity of boron doped nc-Si/SiO$_2$ by the addition of low concentration of P.[48] Recently, red PL spectra peaking at 750 nm have been observed in GeO$_2$ and in sapphire (Al$_2$O$_3$) after Si implantation and subsequent high temperature annealing, which, by analogy with SiO$_2$, should

give rise to the formation of nc-Si. The PL emanating from the GeO_2 samples could be attributed to nc-Si,[49] whereas the luminescence emanating from the crystalline Al_2O_3 samples was not clearly explained and could arise from defects although the presence of nc-Si has been clearly demonstrated in those samples.[50] The existence of luminescent nc-Si in other matrices than SiO_2, as for instance, silicates that have already been identified in space,[7, 8, 9] are supported by all these promising results regarding doped SiO_2 systems or other host matrices.

Recently, in their new observations in the Red Rectangle, which is famous for its red luminescence, Witt and co-workers discovered a new kind of luminescence in the blue (centered at 375 nm) that they associated with the emission from small PAH.[51, 52] However Nayfeh *et al.*[53] bring nc-Si into play again. They suggest that ultrasmall Si nanoparticles with diameters of 1 nm could be the origin of the blue luminescence as well.

Very recent observations of the nebula NGC 7023 with the Hubble Space Telescope provided new constraints for the character of the ERE carrier. Witt *et al.*[54] suggested that ERE excitation results from a two-step process. The first, involving far-UV photons with $E > 10.5$ eV, leads to the creation of the ERE carrier, most likely through photoionization or photodissociation of an existing precursor. The second, involving more abundant near-UV/optical photons, consists of the optical pumping of the previously created carrier, followed by subsequent deexcitation via PL. However nc-Si are photoionized when exposed to photons with energies in excess of 5.1 eV, with the result that PL from subsequent excitations is quenched.[55, 36] Consequently, this new constraint regarding ERE initialization does not favor the nc-Si model.

2.1.1.2. Luminescent defect centers in silicates as carrier of the ERE?

Koike *et al.*[196] observed a broad PL band peaking at 1.9 eV emitted by forsterite single crystals that were irradiated by γ-rays. The authors[197] proposed that forsterite could be responsible for the ERE since their laboratory spectra were similar to astronomical observations of ERE in the Red Rectangle.[22] It should be kept in mind that forsterite has already been detected in space. Interestingly, we have observed an identical PL band from our fused silica windows subjected to He irradiation (Fig. 4.11). The occurrence of this luminescence is due to the formation of defect centers in glassy SiO_2 (non bridging oxygen hole centers, see Sec. 2.2.2.4.). However, it has been demonstrated that this defect PL disappears completely at low temperature (~6 K).[198] Another formation of luminescent defects should be evoked, since Mühlig *et al.*[199] have observed an identical 1.9-eV PL band from windows that were subjected to an intense UV radiation.

2.1.2. Silicon nanocrystals in the inner corona of the sun?

In their recent observation during the total eclipse of 2001 June 21, Habbal and co-workers found in their polarization measurements in the Fe XIII line at 1074.7 nm the signature of interplanetary dust in the inner corona. They observed an emission feature that they attributed to silicon nanoparticles dust grains PL.[56] Motivated by these observations, Singh *et al.* performed some new spectroscopic measurements of the solar corona.[57] But, the authors found no indication of emission around 1074.7 nm.

Mann and Murad have considered laboratory studies which have shown that the nc-Si generation conditions do not resemble those in the inner solar system.[58] They studied the sublimation sequence of silicate dust and demonstrated that silicon sublimates at moderate temperature. Therefore, they concluded that it is not reasonable to suggest the presence of nc-Si near the sun. Besides, they also concluded that it is improbable that nanoparticles of different materials could be confined to very narrow size intervals in the vicinity of the sun.

2.2. Silicon nanocrystals

2.2.1. From bulk to nanosized crystalline silicon

Crystalline silicon structure is the same as diamond which consists of two interpenetrating face-centered cubic Bravais lattices, displaced along the body diagonal of the cubic cell by one quarter of the length of the diagonal. The lattice constant is 5.42 Å and the interatomic distance is 2.35 Å. Each silicon atom is covalently bonded to its four nearest neighbours by the sharing of electron pairs by *sp3* tetrahedral hybridization of one s-orbital and three p-orbitals. As a result, the energy levels of each orbital split and, as a consequence, a quasi-continuum of energy levels is formed describing the energy bands. Figure 2.6 shows a theoretical calculation of these energy levels by Kane[59] within the irreducible Brillouin zone. A transformation of the polyhedron formed by the silicon atoms disposed in the cubic cell (Fig. 2.6.a) by all the symmetry elements of the crystal forms the first Brillouin zone. The energies are evaluated here by the pseudo potential method as a function of wave vectors along the LΓΔXW path (Fig. 2.6.b). In the diagram showing the state density associated with the band diagram, the structure of the valence and conduction bands is depicted (see Fig. 2.6.c). The bands are separated by a band gap energy E_0 of 1.13 eV at room temperature and 1.17 eV at 0 K. The band gap is an indirect band gap because the maximum of the valence band (Γ) and the minimum of the conduction band (X) are not located at the same position. Semiconductors with indirect band gap are inefficient in emitting light. This is because any electrons present in the conduction band quickly thermalize to the lowest energy states of this band. In this way, a transition is only feasible with a source of momentum supplied by a lattice vibration, called pho-
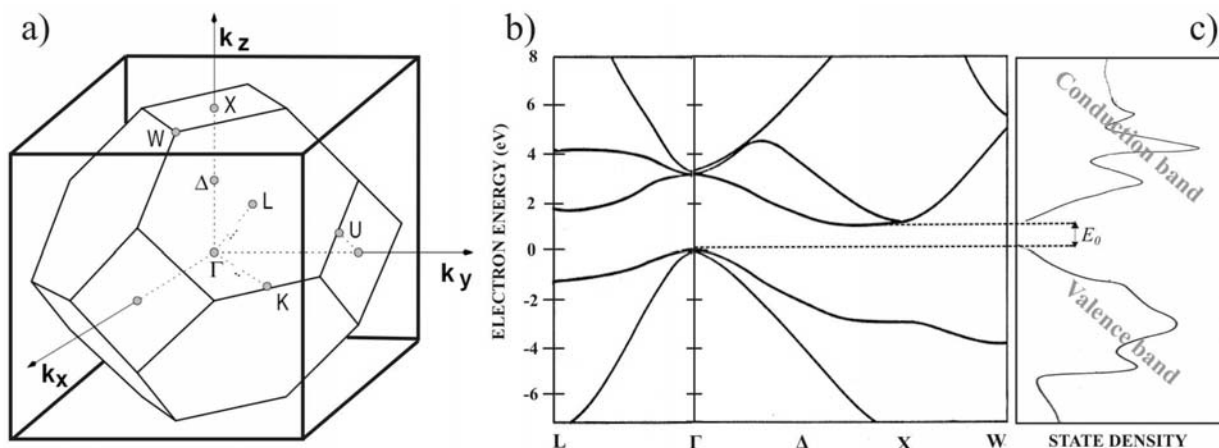
Fig. 2.6. a) Schematic of the first Brillouin zone within an elementary crystalline silicon lattice, b) and the relative band structure evaluated on the LΓΔXW path. The band gap is indirect since the maximum of the valence band and the minimum of the conduction band are not located at the same position. The band gap energy E_0 is displayed in the right frame displaying the density of state.

non. Therefore, the probability of a so-called phonon-assisted transition, which can occur both in emission or absorption, is close to zero at room temperature. As a result, the PL yield of bulk silicon is close to zero at room temperature.

In 1990, Canham[4] observed an intense visible PL from porous silicon exposed to UV light ranging from green to red in color. He synthesized 1D confined structures – nanowires – by electrochemical etching of crystalline silicon wafers. Independently, Lehmann and Gösele[60] reported on the optical absorption properties of porous silicon. They observed an increase in the absorption band gap of 2D structures – nanowells – compared to bulk silicon. Size dependence of the PL emission energy and absorption energy was also found for silicon nanocrystals – 0D confined structures – where smallest particles emit light at shorter wavelengths (higher energies). PL properties of nc-Si are now well described in the literature, but its origin is still under debate. nc-Si can emit light from 1.13 to 2.15 eV with a broad spectrum (300 to 400 meV). The temperature dependence of PL is singular with a maximum of intensity around 75 K. The lifetimes are quite long (from a few microseconds at room temperature up to several milliseconds at temperature lower than 50 K) and increase exponentially with the emission wavelength. Signatures of transversal optical (TO) phonons (56 meV) and transversal acoustic (TA) phonons (18 meV) were observed in resonant PL spectra[61] or in PL spectra at low temperature.[62] Two trends have been perceived in the size dependence of PL emission. They will be discussed at the end of this chapter in section 2.2.4.

2.2.2. On the origin of photoluminescence of silicon nanocrystals

Optical properties of nc-Si have been the subject of numerous studies, since it was realized that they can constitute bright light sources in the visible range, leading to potential applications in optoelectronics. Various models have been proposed to describe the mechanism of luminescence of nc-Si. It is generally accepted that quantum confinement effect, which is intrinsic to the nanosized crystalline silicon, is the most accurate theory, but it cannot alone explain all the characteristics reported in the section before. Passivation mode, spatial confinement effect, participation of localized surface states or interface states, defects in silicon dioxide, and the effect of compression have also been suggested to influence the PL spectra of nc-Si.

2.2.2.1. Quantum confinement

i) Principle

This model was first proposed by Canham[4] in 1990 to explain the visible PL of porous silicon. Its principle, outlined in Fig. 2.7 can be explained as follows: when the structure size becomes sufficiently small, *i.e.* in the same order of magnitude or inferior to the Bohr radius (~5 nm), photogenerated excitons (electron hole pairs) are trapped into a quantum well. The solution of the Schrödinger equation gives discrete energy levels with energies inversely proportional to the square of the width of the well, *i.e.* the size of the nanoparticle, the smaller the nanoparticle the higher the energy band gap. A first approach is given by the calculation of the energy levels in the effective mass approximation of a spherical quantum well
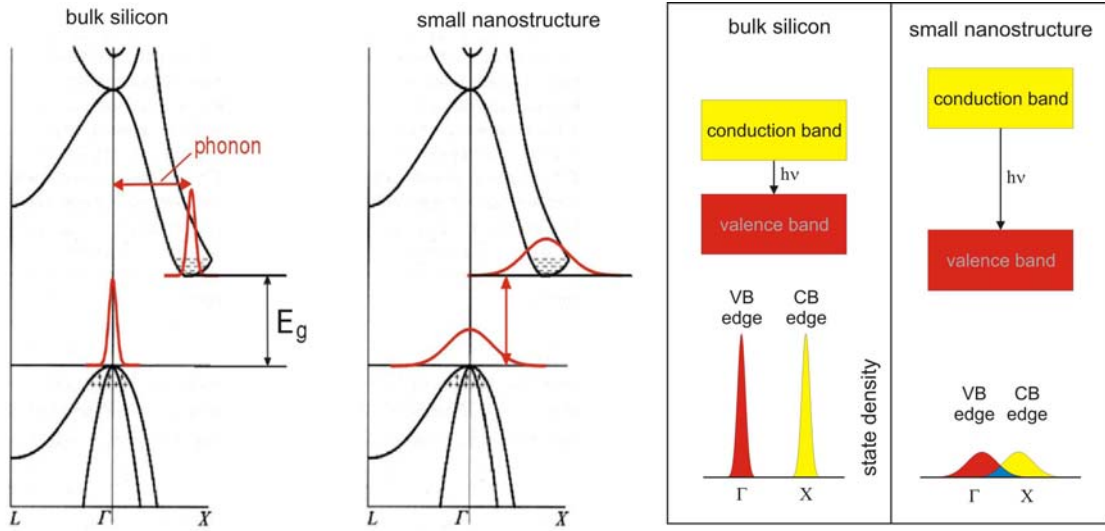
Fig. 2.7. Schematic of quantum confinement in silicon.

$$E(d) = E_0 + \frac{\hbar^2 \pi^2}{2d^2}\left(\frac{1}{m_e^*} + \frac{1}{m_h^*}\right) - \frac{1.8e^2}{\varepsilon_i d} \tag{1}$$

where d is the nanoparticle diameter expressed in nanometer, m_e^* and m_h^* are respectively the effective masses of electron and hole; e is the charge of electron, ε_i is the electric permittivity of silicon, and E_0 is the bank gap of bulk silicon. The third term is the Coulomb interaction energy between electron and hole. The space confinement results also in a broadening of the wave vectors and the band structure is said to become more direct-like, *i.e.* no phonon is needed. The probability of radiative transitions is now increased and thus more efficient. Quantum confinement consequences are as follows: a widening of the band gap and a rise of emission intensities with the confinement.

Equation 1, plotted in Fig. 2.8, displays that the band gap energy of nc-Si varies inversely with the diameter of the particle. This trend is generally observed in experiments and supports the theory of quantum confinement. Nevertheless, this simple approach does not exactly fit with measurements. It has been mentioned that the presence of dangling bonds at the nc-Si surface[5] quenches considerably the luminescence since they are expected to be very efficient non-radiative recombination centers. The presence of hydrogen and/or oxygen atoms in the nc-Si surroundings is known to contribute to a good passivation of the dangling bonds which results in a sensible increase of the PL intensity. Efforts are made by many researchers to obtain more accurate theoretical evaluations of the behavior of the emission band gap as a function of the size by using computational calculations which take into account the nc-Si passivation mode.

ii) Computational calculations: H-passivated and O-passivated nc-Si

In Fig. 2.8 are summarized the results of theoretical calculations of the PL emission energy as a function of particle size for nc-Si passivated with either hydrogen (red) or oxygen (blue). It is generally admitted that theoretical results of H-passivated nc-Si evaluated by tight-binding method,[5, 63, 64, 65] which are in a good agreement with those evaluated by pseudopotential method,[66] are the most accurate. The solid red curve corresponds to the theoretical tight-
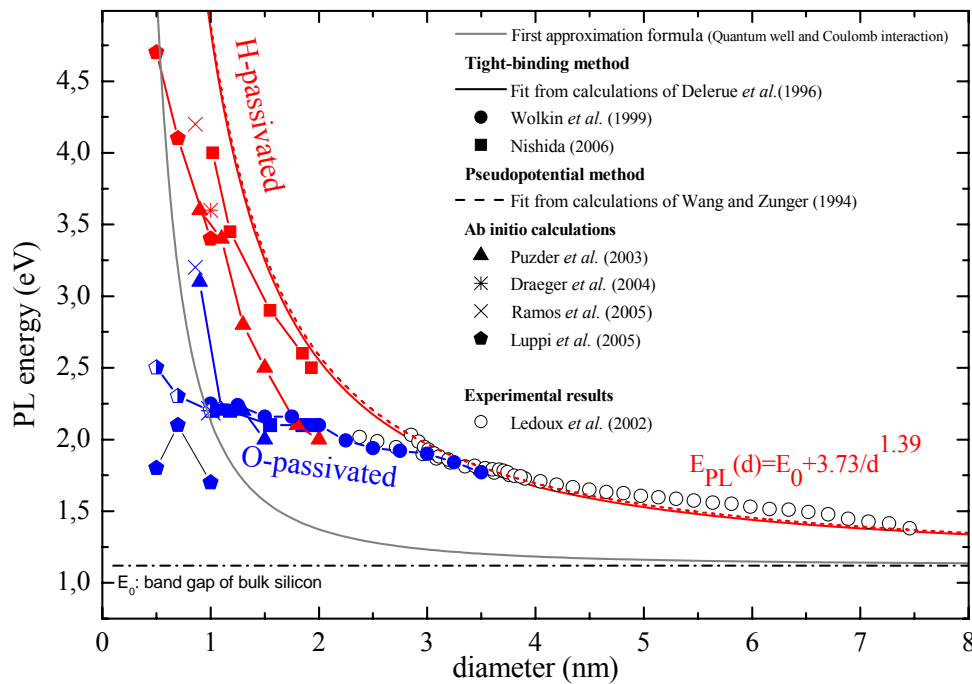
Fig. 2.8. Theoretical results of PL emission energy of free nc-Si as a function of the size. The grey curve corresponds to a first approximation of quantum confinement given in Eq. (1). Other theoretical results regarding H-passivated free nc-Si, and O-passivated free nc-Si, are depicted in red and blue, respectively. They are classified according to their calculation method; see the legend within the frame. In addition experimental results from Ledoux et al.[72] are displayed in black open circles.

binding calculations of Delerue et al. which is represented by an inverse power law $E_{PL}(d) = E_0 + 3.73\, d^{-1.39}$, where E_0 is the band gap energy of bulk silicon. But, as it can be seen in Fig 2.8, these results differ significantly from *ab initio* calculations,[67, 68, 69, 70] which, however, can only be evaluated for particles smaller than 2 nm.

The effect of oxidation on preliminary H-passivated nc-Si has been studied by Wolkin et al.[71] who have observed a red shift – an energy loss – in the PL spectra for particles smaller than 3 nm. This was explained by the fact that hydrogen atoms were replaced by oxygen atoms at the surface by forming Si=O bonds which are more likely to be formed and passivate the nc-Si. Their observations were in a good agreement with theoretical calculations performed by the same authors on O-passivated nc-Si displayed in blue circle symbols. The formation of Si=O bonds provides new electronic states in the band gap of the smaller quantum dots. A loss in the emission energy of nc-Si passivated with one Si=O bond, compared with H-passivated nc-Si, is usually found for particles smaller than 2 nm whichever computational method is employed (see Fig. 2.8).[67, 68, 69, 70]

Moreover, the results from Luppi and Ossicini,[67] which are depicted by full and half-full blue pentagons that correspond to nc-Si passivated with, respectively, two and six Si=O bonds, indicate that the energy loss depends on the number of oxygen bonds. This effect is limited by saturation as previously demonstrated by Draeger et al.[68] Another illustration of the effect of oxidation is given in Fig. 2.8, by the experimental data from Ledoux et al. depicted with open circle symbols. They studied the PL of oxidized free nc-Si preliminarily passivated with hydrogen and/or an amorphous layer of polysilane. It is clearly seen that their results comply partially with the theory of Delerue et al. and also with the calculations of Wolkin et

al. and Nishida.[65] This can be simply understood in terms of difference between the oxidation states of samples.

But, other types of silicon oxygen bonds at the nc-Si surface must be considered. In their photoinduced absorption spectra of nc-Si embedded in quartz, Sa'ar *et al.*[12] found the signature of the vibrational mode of Si-O-Si groups, where the oxygen atom vibrates in parallel to the line joining the two silicon atoms that are believed to belong to the silicon nanostructure.

2.2.2.2. Spatial confinement

Spatial confinement does not modify the band gap structure of the material that is intrinsic. In this model, silicon still remains an indirect material and a phonon is still needed to assist the radiative transition. The emission yield is given by $\eta = R_{rad} / (R_{rad} + R_{non-rad})$, where R_{rad} and $R_{non-rad}$ are respectively the radiative and non-radiative rates of the transition. This formula expresses the fact that, when non-radiative rates are faster than radiative rates, the emission yield is rather weak. This can be also interpreted in terms of capture volumes around defects, which are the most important centers of non-radiative transition in crystalline structure. A photo-excited electron-hole pair generated within this volume is trapped by the defect and recombines non-radiatively. The emission yield is thus given by the ratio between the non-covered crystalline volume and the total volume. In bulk silicon, the capture radius is so large that it does not allow luminescence (see Fig. 2.9.a).

For crystalline particles with a diameter smaller than the mean distance between two defects, Fig. 2.9.b, the fraction of defect-free particles will vary inversely with the size. The probability that a nanocrystal with a volume V_{nc} will contain k defects in the presence of a uniform concentration of defects N_d, is given by the Poissonian distribution[74]

$$P(k) = \frac{e^{-V_{nc}N_d}(V_{nc}N_d)^k}{k!}.$$

Assuming that a single defect inside a nanocrystal completely quenches all the PL emission of that nanocrystal, all nanocrystals containing at least one defect will not emit light. Hence, the probability that a nanocrystal will be optically active in a sample with defects is given by the probability of having no defects inside this nanocrystal
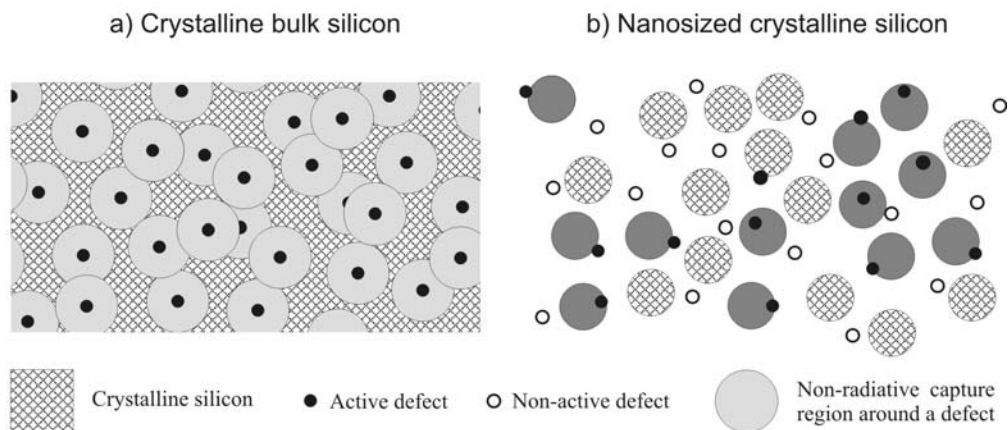
Fig.2.9. Schematic of luminescence yield in bulk (a) and nanosized crystalline silicon (b), adapted from Wehrspohn *et al.*[73] Black dots represent radiative defects and grey areas the capture volume of the defect.
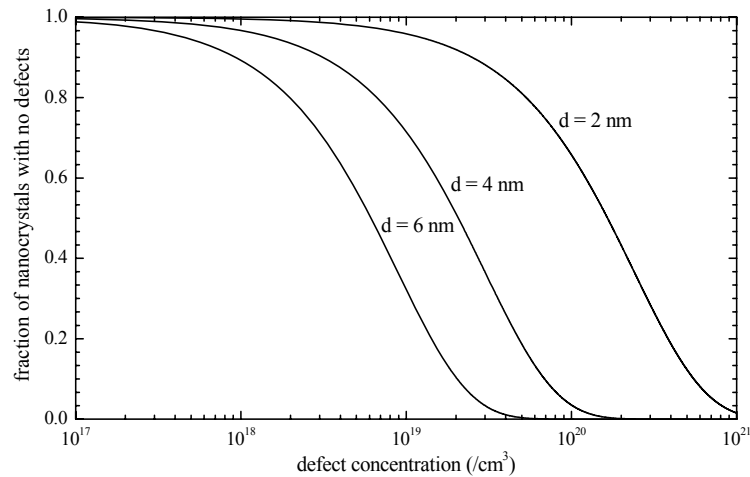
Fig. 2.10. Calculated probability that a spherical nanocrystal contains no defects as a function of the defect concentration. Data are shown for nanoparticle diameters of 2, 4 and 6 nm.

$$P(k = 0) = e^{-V_{nc}N_d}.$$

This probability calculated for spherically shaped nanocrystals is plotted in Fig. 2.10 as a function of defect concentration for different nanoparticles diameters ranging from 2 to 6 nm. This graph demonstrates that for a given concentration of defects, smaller nanoparticles have less defects than larger ones. As a result, smaller particles can give rise to higher intensity light emission than larger ones.

In an interesting article, Wehrspohn *et al.*[73] reported on the study of optical properties of crystalline and amorphous nanosized silicon structures which were produced separately by electrochemical etching of silicon wafers. PL spectra, displayed in Fig. 2.11, were measured *in situ* during the etching process. For crystalline silicon (Fig. 2.11.a), it is seen that while the porosity increases, *i.e.* while the sizes of the structure is reduced, the PL peak is shifted to shorter wavelengths and the PL intensity increases. Whereas, for amorphous silicon (Fig. 2.11.b), the PL peaks remain at the same position as the PL intensity decreases. The blue shift observed for crystalline silicon is a confirmation of quantum confinement that affects the band gap structure of crystalline silicon. Whereas, for amorphous silicon, the emission energy is fixed and does not depends on the size. In an amorphous structure, the energy band gap is only determined by the disorder-induced localized states that are believed to be independent of the size. The PL arising from amorphous silicon is generally observed at energies ranging from 1.3 to 1.5 eV (820 to 950 nm). Quantum confinement can take place together with spatial confinement that can partially explain the increase of PL intensity observed in Fig. 2.11.a in accordance with the fact that the probability of presence of defects is smaller for smaller particles. In Fig. 2.11.b, the decrease of PL intensity was associated with the loss of material during the etching process. However, in this model, defects within the volume of the nanoparticles are only considered. But, it is known that defects at the surface, like dangling bonds, are important non-radiative transition centers and contribute to the quenching of PL emission. The spatial confinement model is also relevant for the study of doping of nc-Si where a dopant atom can be simply considered as a defect while it is present inside the crystalline structure.
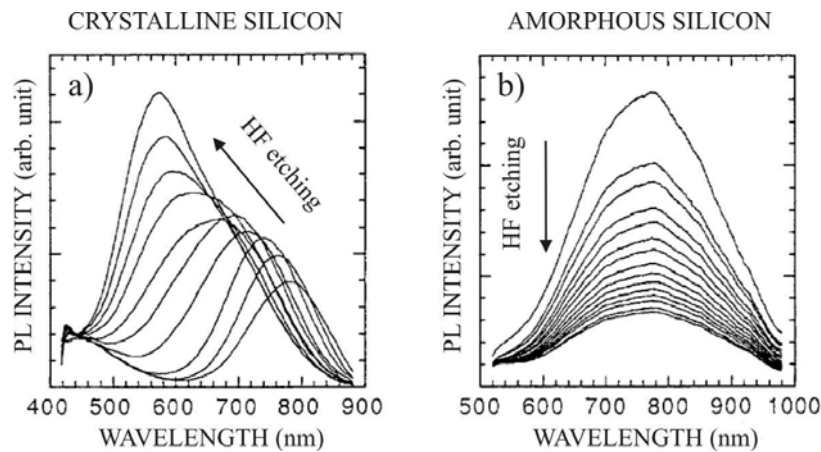
Fig. 2.11. Evolution of the *in situ* PL of (a) crystalline porous silicon and (b) amorphous porous silicon in HF solution, extracted from Wehrspohn *et al.*[73]

2.2.2.3. Quantum confinement and surface states or interface states models

The surface states model has been proposed by Koch *et al.*[75] to explain the luminescence observed at one fixed emission energy (~1.7 eV) independently of the sizes of the silicon particles. Others groups,[76, 77, 78, 79] which studied the optical properties of either oxidized free silicon nanostructures or nc-Si synthesized within a quartz matrix, reported on analogous observations. In this model, quantum confinement and surface states coexist. The latter creates localized states in the band structure of nc-Si. Photon absorption still takes place inside the nc-Si, but, the photo-generated exciton can recombine according to three different processes E_i, displayed in Fig. 2.12.a. The subscript i points the number of surface states involved in the recombination: E_0 band-to-band recombination within the nc-Si volume (quantum confinement), E_1 quick band-to-surface states transition (electron is trapped in the surface), E_2 slow surface-to-surface state transition (electron and hole are trapped in two different surface states). Nevertheless, the weight of every process depends on the size of the particles. A smaller size favours E_1 and E_2 transitions to the disadvantage of E_0 transitions, since excitons are believed to be easily trapped in smaller clusters than in largest ones, and since the band gap increases inversely with the cluster size.

Kanemitsu[78] proposed a slightly different model to interpret the luminescence observed
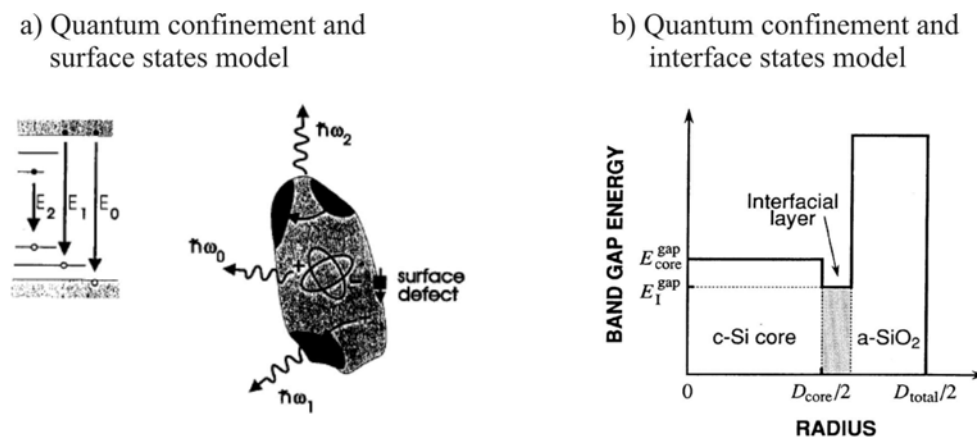
Fig. 2.12. a) Radiative transition mechanisms involving three different recombination processes, according to the quantum confinement and surface states model, from Koch *et al.*[75] b) Three regions bands schematic proposed by Kanemitsu.[78] In this model, excitons are confined in the interface region between the nc-Si core and the SiO$_2$ matrix.

at 1.7 eV. Excitons are still generated within the nc-Si core by absorption, but after that, they move to the suboxide interface ($SiO_{x<2}$) between the nc-Si and the SiO_2 matrix, where they will recombine radiatively. Based on *ab initio* calculations, they showed that the presence of a $SiO_{x<2}$ interface layer creates a potential well between the nc-Si and the host matrix (see Fig. 2.12.b). The band gap of this potential is believed to be independent of the nc-Si size. As a consequence transitions take place at the same energy that, according to their calculations, corresponds to 1.65 eV.

Recently, López *et al.*[79] probably found why other researchers observed PL spectra at a fixed position (~1.7 eV) for either several annealing durations[77] or several oxidation temperatures,[76] which are both susceptible to modify the size distribution of nc-Si. As a result, it has been believed that emission energy was independent of the size of the nanoparticles. The authors were interested in the relation between PL and Si dangling bonds at the nc-Si surface (*Pb* defects, see Fig. 2.14) in samples produced by Si implantation in fused silica. Si dangling bonds are very efficient non-radiative recombination centers that kill the PL. *Pb* defects were identified by electron spin resonance (ESR). The excess of silicon in SiO_2, supplied by Si implantation, nucleates during an annealing performed at high temperature to form nc-Si. Particles growth is caused by Ostwald ripening and takes place mainly during the first minutes of the annealing, as it was reported elsewhere.[10,15] They revealed that PL intensity steadily increased and reached saturation after 3 - 4 hours of annealing time. Such behavior showed an inverse correlation with the amount of Si dangling bonds at the interface between nc-Si and the host SiO_2 matrix. Besides, they reported that a post-annealing performed in a forming gas (95% N_2 + 5% H_2) significantly enhance the PL intensity, due to a reduction of the number of Si dangling bonds, without modifying the position (~1.7 eV) and shape of the PL spectra. It seems that, for nc-Si embedded in SiO_2, the PL is not wavelength dependent for smaller nanocrystals ($\leq$ 3 nm).[10, 158] In this regime, the recombination of excitons would originate from interface states in the band gap of nc-Si.
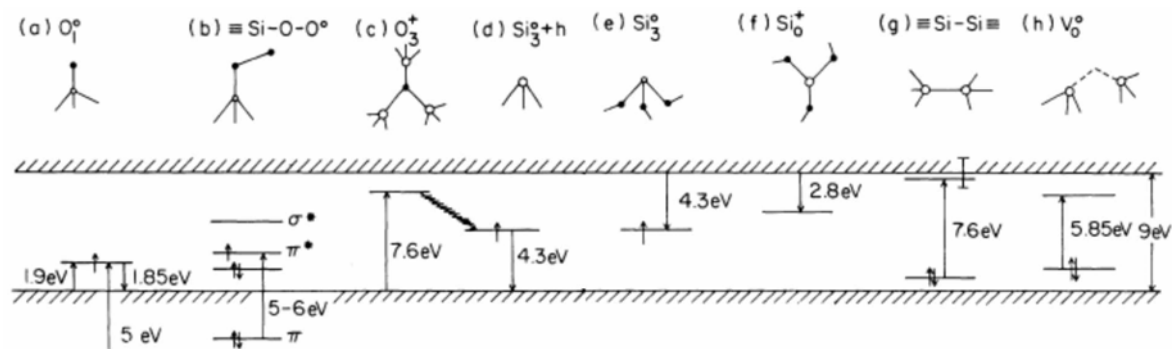
Fig. 2.13. Calculated optical transitions due to defects in SiO_2: (a) excitations at non-bridging oxygens, (b) excitations at peroxyl radicals, (c) excitation of an electron into the shallow state of O_3^+, followed by its relaxation to (d) Si_3^0 and (e) recombination with 4.3 eV luminescence, and (f) other transitions at Si_3^0 an Si_3^+, and (g) $\sigma \rightarrow \sigma^*$ transition at Si-Si bond, and (h) possible transition at a neutral oxygen vacancy, according to O'Reiily and Robertson.[80]

2.2.2.4. Radiative emission from defects in SiO$_2$

Defects in quartz induce localized states in the band gap of SiO$_2$ that are possible sources of radiative recombination. In Fig 2.13, several optical transitions due to defects in SiO$_2$ evaluated by O'Reiily and Robertson are shown.[80] According to their calculations, two radiative transitions are present in the visible range precisely at 2.8 eV (440 nm) and 1.85 eV (670 nm). The 1.85 eV transition corresponds to an isolated non-bridging oxygen atom ($\equiv$ SiO$^{\bullet}$) that acts as hole-trap center, hence the name Non Bridging Oxygen Hole Center (NBOHC); see Fig. 2.14. On the other hand, Tohmon *et al.*[81] showed in their *ab initio* calculations that neutral oxygen vacancy defects ($\equiv$ Si-Si$\equiv$) are responsible for the 2.7 eV in quartz which was repeatedly observed by various authors.[82] Experimentally, two intense peaks at 2 and 1.9 eV (620 and 650 nm) were observed by Munekumi *et al.*,[83] in PL spectra of various quartz samples. The 1.9 eV emission peak was attributed to a NBOHC whereas the 2 eV transition was expected to arise from NBOHC partially passivated with a hydrogen atom. Interestingly, strong visible PL, with a maximum at 1.9 eV, attributed to NBOHC, was also observed from originally non-luminescent free nc-Si powders after treatment in water.[85] This treatment induced a transformation of the nc-Si into hollow silica nanoparticles.

Prokes and Carlos[84] compared PL spectra and ESR measurements (ESR reveals the evolution of density of NBHOC) of porous silicon as a function of the oxidation temperature. They clearly showed a good correlation between PL intensity and the amount of NBOHC. Therefore, they proposed that NBHOC are responsible for the main emission mechanism in their samples. However, they underlined that no particle size dependence on the PL emission energy has been found with this model. Indeed, the position of the maximum of the PL spectra was fixed at ~1.7 eV. However, this energy does not correspond to the values reported before. Therefore, we rather believe that, in this regime, the recombination of excitons would originate from surface states in the band gap of nc-Si.

In a crystalline silicon core and SiO$_2$ shell structure, various emissions mechanisms can be active. Radiative defects in the SiO$_2$ surrounding can coexist with quantum confinement effect that will act on the PL spectra properties.
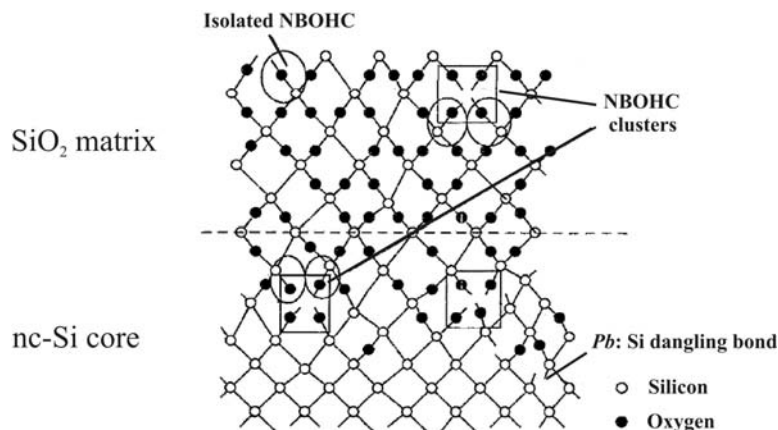
Fig. 2.14. Schematic of defects present at the surface of the silicon nanostructure (*Pb*: silicon dangling bonds) or in the SiO$_2$ surrounding layer (NBHOC).

2.2.2.5. Other origins

Hydrogenated amorphous silicon, surface hydrides (Si-H$_x$) and molecules (siloxene) have been proposed as luminescent species present in porous silicon passivated with hydrogen.[86] Indeed, several studies showed the existence of tuneable visible light due to these species. Nevertheless no size dependence on the PL has clearly been demonstrated. But, these models can be especially questioned since they cannot explain why PL subsists after the desorption of hydrogen.

2.2.2.6. The effect of compression

In their very interesting work, Sood *et al.*[87] measured PL spectra of porous silicon under various pressures. Powder containing Si nanostructures were introduced in paraffin oil as pressure transmitting medium. They observed a significant red shift with the increase of the pressure. The PL maximum position varied in a roughly linear relationship with a proportional factor f = -40 meV/GPa. The pressure dependence of PL properties seemed to be independent of the nc-Si size. Independently, Hofmeister *et al.*[88] measured the {111} lattice plane fringes of nc-Si covered with an amorphous SiO$_2$ shell that was formed after synthesis by an exposition to ambient air. They observed that lattice distances shrink with the particles sizes. They proposed that the state of compression on the nc-Si, monitored by the lattice spacing, could be interpreted in terms of the formation of an oxide layer at the particle surface, since the oxide shell thickness was found to be larger for larger core dimensions. In the article of Ledoux *et al.*,[89] these observations of the lattice shrinking as a function of the size were associated with the effect of compression on the PL spectra mentioned by Sood *et al.* Their resulting formula is plotted in Fig 2.22. A red shift, which increases with the size, was expected for diameters larger than 3.5 nm for their samples containing free nc-Si that were oxidized in ambient air. Hyeonsik *et al.*,[90] who were interested in nc-Si embedded in SiO$_2$ produced by ion implantation, observed a similar red shift of PL spectrum with increasing hydrostatic compression. For high pressure measurements, their samples were thinned down to ~25 µm by mechanical lapping and then cleaved to dimensions of ~150×150 µm^2. He was used as the pressure medium. The PL maximum position varied in a linear relationship with the pressure. However, they found a proportional factor eight times lower than Sood *et al.* (f = -5 meV/GPa).

In their theoretical calculations, Draeger *et al.*[68] demonstrated that the band gap of nc-Si is sensibly reduced with the increase of hydrostatic compression which was simulated by a uniform Si-Si distances rescaling. They made it evident that band gaps decrease more significantly for structures that undergo larger distortions. Moreover, they suggested that, in O-passivated nc-Si, the distortion of silicon bonds at the surface is caused by oxygen atoms in different geometries. Indeed, one can easily conceive that silicon atoms involved either in a double Si=O bond or in a Si-O-Si bond joining the silicon nanocrystal to its silicon oxide surrounding are distorted. The geometry of these bonds should directly influence the distortion of the Si-Si bonds localized close to the surface.

2.2.2.7. Conclusion

The various models related in this section arise from the interpretations of several experimental results. As a consequence, no one can explain the totality of the observations. However, the models based on hydrogenated amorphous silicon, surface hydrides and molecules should be excluded since they can not predict the PL exhibited by samples which do not contain any hydrogen atoms, for instance nc-Si embedded in SiO_2. The most likely accurate theory, which best describes the size dependence of the PL emission energy, the large width of the PL spectra (300 to 400 meV) and the emission energy dependence on the luminescence lifetime, remains the model of quantum confinement proposed first by Canham to explain the luminescence of porous silicon. Nevertheless, the spatial confinement, the radiative surface states and interface states, the radiative and non-radiative defects, and the effect of compression should be taken into consideration to explain the nature of the PL of nc-Si.

2.2.3. Production techniques of silicon nanocrystals

In the following sections, the most-employed techniques to produce free or embedded nc-Si are synthetically described. The sample's qualities are briefly compared according to their production techniques in terms of size distribution and PL yield. Finally, some results concerning the size dependence of the PL emission energy, which are discussed in Sec. 2.2.4., are summarized, and, since it seems to influence the PL properties significantly, some comments on the passivation process will be made. For more details on the PL and size measurements of these reported results, a summary is shown in Appendix. A.

2.2.3.1. Pulsed laser ablation

This technique consists in focusing a laser beam of high power density on a target, generally a single silicon crystal, to eject ions, atoms or aggregates of atoms that form a hot and dense plasma which expands in the form of a plume perpendicular to the target surface, as illustrated in Fig. 2.15. Adiabatic expansion and cooling of the plasma lead to cluster condensation inside the plume. The size and spatial distributions of the free nc-Si depend on the pressure and the nature of the ambient gas as well as the laser power density. In Fig. 2.16, the flux of material is shown as a function of time after the short laser pulse by taking advantage of the plasma thermoluminescence resulting from the laser ablation. During expansion, the leading part of the plume, formed by rapid particles, pushes and compresses the background gas. Be-
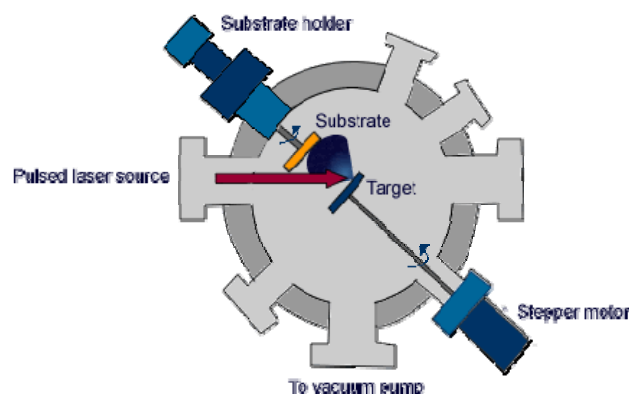
Fig. 2.15. Schematic showing the principle of pulsed laser ablation system.[92]

cause of the opposite pressure gradient, the plume expansion slows down and stops, and the particles within the plume form a flux flowing back towards the target. A size separation can be achieved by using the fact that, due to collisions with the ambient gas molecules, smaller clusters are scattered at higher angles whereas higher mass clusters undergo a smaller angle scattering. As a result, a longitudinal gradient of nc-Si sizes can be obtained by positioning the substrate perpendicularly to the target, whereas a deposit with a radial dispersion of sizes can be produced with a substrate placed opposite of the target. Nevertheless, the size distribution of the so-obtained deposits is of average quality, to the point that some PL curves showed even a clearly three-modal distribution.[91]

In the work of Orii et al.[14], the clusters were annealed at 900°C immediately after production and separated in size by a differential mobility analyser in order to improve the size distribution quality. Si nanoparticles were finally deposited on a substrate. Because of exposure to air after synthesis, the so-produced Si-clusters were found by high resolution transmission microscopy (HRTEM) to be covered by an amorphous SiO_2 layer. The diameters of the crystalline core and oxide shell were measured by the analysis of HRTEM images. The shell thickness was quite important and represented from 29% for the largest particles to 51% for the smallest ones of the diameter of the core-shell structure. As a result it can be affirmed that the nc-Si were strongly oxidized in this case. On the other hand, Patrone et al.[91] studied the PL spectra of their deposited samples directly after production. nc-Si accordingly should be considered as slightly oxidized mainly because of transportation in air ambient. The sizes of the nanostructures were evaluated by atomic force microscopy (AFM). It is interesting to mention that they obtained some samples doped with gallium nitride. This was not expected and was explained by the fact that they also performed some experiments meanwhile on the synthesis of gallium nitride nanocrystals in the same apparatus chamber. It seems that it is difficult to control the doping with this technique that was accidental in this case. Nevertheless, it reveals the importance of purity of the environment, since the synthesis of nc-Si is not performed in a high vacuum chamber. For this reason, the quality of samples should be considered as low.
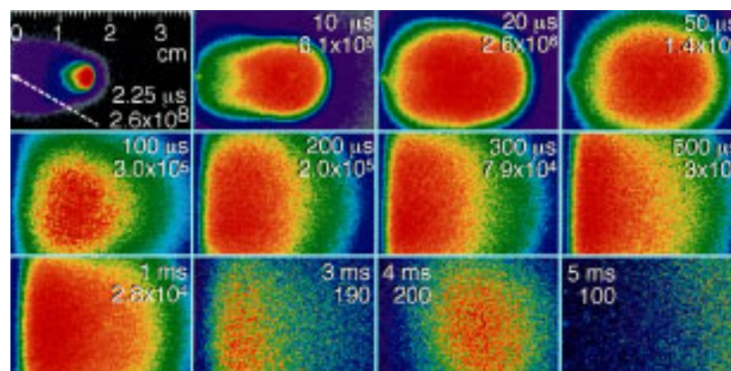
Fig. 2.16. Photographs of the nascent visible plasma luminescence observed when a silicon target is laser-ablated (KrF laser, 28 ns FWHM pulse, incident at 30° as shown), by Geohegan et al.[93] The time delay after ablation and the maximum intensity (red) of each image are listed.

2.2.3.2. Laser pyrolysis of silane

This technique will be described in more detail in Sec. 3.1.1., since it was employed in this work. It has been extensively employed by previous co-workers of our group. A number of articles has been published and their contents are summarized thereafter. Note that this technique allows the synthesis of free nc-Si with an efficient size selection, and the PL yield is quite strong and can reach up to 30%.

In studies reported by Ehbrecht et al.[94] and later by Ledoux et al.,[37, 72, 89] nc-Si were synthesized by laser pyrolysis of silane in a gas flow reactor. The nc-Si were subsequently extracted through a conical nozzle into a high-vacuum chamber. Nanoparticles in the resulting aerosol beam were size selected by a molecular beam chopper and were deposited on a dedicated substrate. The aerosol beam was analyzed by time-of-flight mass spectrometry (TOFMS) to determine the size distribution of the silicon clusters. Raman spectroscopy,[94] proved that the nc-Si produced by this technique were crystalline, and confirmed the size measurements obtained by TOFMS. The PL of the silicon films kept in a neutral argon atmosphere was measured by Ehbrecht et al., whereas Ledoux et al. were interested in the PL of the films gently oxidized by exposition to air. But, in spite of precautions taken by Ehbrecht et al. to avoid exposition to air, the first films studied were certainly already oxidized. A good agreement between size measurements obtained by TOFMS and AFM on fresh deposited samples was found by Ledoux et al.[89, 37] TEM images of oxidized deposits,[72] which also confirmed the crystallinity of the so-produced clusters, demonstrated that the latter films were actually surrounded by a thin silicon oxide layer with a thickness representing around 8% to 16% of the cluster volume. This observation was taken into account in order to correct the average diameters of the nc-Si obtained by TOFMS evaluation.

2.2.3.3. Aerosol technique

In this technique, the synthesis of free nc-Si is done by the pyrolysis of either silane[95, 96] or disilane[97, 98] at 700 - 1000° C in a high temperature gas flow reactor shown in Fig. 2.17. Silicon atoms resulting from the decomposition of silane or disilane nucleate rapidly, and the nanoparticles continue to grow by vapour deposition and coagulation in the flow of diluent gas (He or N_2). The pyrolysis reactor must be oxygen-free to prevent the formation of silicon oxides instead of crystalline Si. The as-obtained aerosol flows through a quartz tube where the clusters are sintered to produce dense, spherical, crystalline nanoparticles. Once formed, the

Fig. 2.17. Schematic of a high-temperature aerosol apparatus allocated for silicon particle synthesis according to the work of Ostraat et al.[95]

nc-Si can be removed from the aerosol or be led trough an oxidation reactor dedicated to the thermal growth of an oxide shell around the Si nanoparticles. Because of the relative high in-homogeneity in sizes observed directly after production, the so-produced nc-Si are generally separated in size either by a dynamic technique[95] or by precipitation of a nanocrystalline colloid.[97]

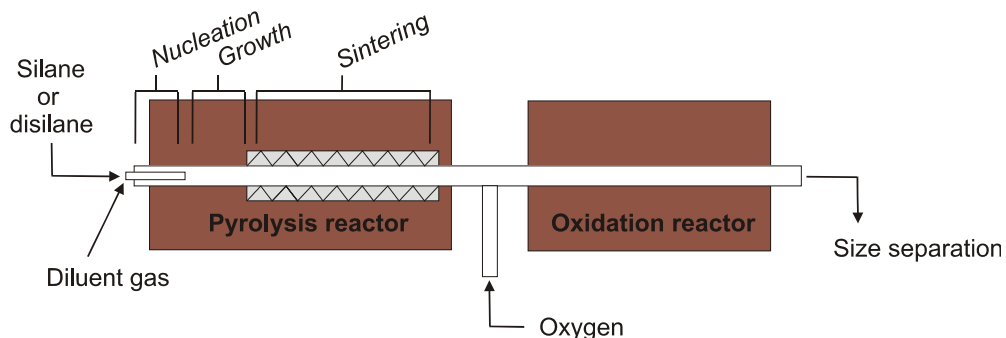Schuppler *et al.*[97] studied oxidized nc-Si produced by pyrolysis of disilane in a high-pressure flow of He subsequently oxidized in O_2 between at 700 and 1000 °C during 30 ms. The resulting aerosol was bubbled through ethylene glycol to be finally separated in size by precipitation. TEM images of the so-obtained nanoclusters revealed a core-shell structure (crystalline silicon - amorphous SiO_2) separated by an intermediate layer of incompletely oxidized silicon SiO_x. The thickness of the external layer was found to be relatively constant and represented from 29% to 9% of the cluster diameter, for the smallest and the largest nc-Si respectively. More recently, Ostraat *et al.*[95] produced nc-Si by nucleation of silicon resulting from the decomposition of silane in a free oxygen furnace at 950 °C. Si nanocrystals formed during 30 ms in a gas flow of N_2 and were extracted out of the reactor. Nanoparticles in the so-formed aerosol were subsequently positively charged with a Kr ion gas, and migrated radially in the presence of a negative electric field. A size separation was realized according to the principle that the particles mobility depends only on the nc-Si mass. Ostraat *et al* were interested in the oxidation of nc-Si by various thermal treatments. They could observe a PL emission at 1.13 eV, close to the emission band gap of silicon, arising from strongly oxidized nc-Si with diameters of 8 and 12 nm that were determined by transmission electronic microscopy (TEM).

2.2.3.4. Chemical vapor deposition

Silicon oxide films containing nc-Si were studied before the discovery of the visible PL of porous silicon. In 1984, DiMaria *et al.*[99] realized electroluminescence studies on Si-rich SiO_2 films produced by CVD. They detected a weak electroluminescence between 1.7 and 2.0 eV. This discovery, not completely understood at this time, did not excite a lot of interest until the PL properties of porous silicon were revealed. Then many groups improved this production method and increased the luminescence yield of the films. This method has the advantage to produce silicon quantum dots homogenously distributed on a large scale. One can distinguish two principal techniques that derive from this method, which are commonly used to create thin films of nc-Si. The low-pressure chemical vapor deposition (LPCVD) and the plasma-enhanced chemical vapor deposition (PECVD). In the former technique the so-produced clusters are free nc-Si covered with a thin polysilane layer whereas, in the latter one, nc-Si are generally embedded in SiO_2. However, PECVD has the advantage of making it possible to produce numerous layers containing nc-Si separated by an oxide film.[39]

i) Low pressure chemical vapor deposition (LPCVD)

Hitchman and Kane[100] were among the firsts to develop this technique to grow nc-Si. The method, as described by Fukuda *et al.*[101], consists in the spontaneously growth of nc-Si on a substrate, usually a silicon oxide layer thermally grown on a silicon wafer, by the pyrolysis of pure silane at a temperature around 600°C, as illustrated in Fig. 2.18. The most likely mecha-

T ~ 600°C

SiH₄   H₂

| SiO₂ |
| Silicon wafer |
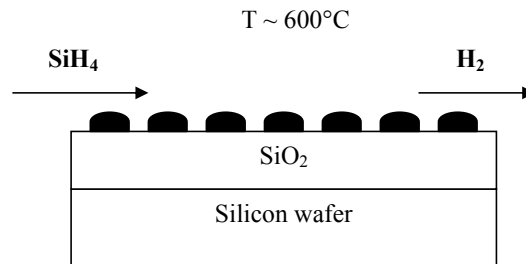
Fig. 2.18. Schematic of the synthesis of silicon clusters by low pressure chemical vapor deposition

nism involved in the growth of silicon nanoparticles is described by the following reactions: $SiH_4(g) \rightarrow Si(s) + 2\,H_2(g)$. The deposition rate of this technique varies from 0.3 to 10 nm/min and depends principally on the deposition temperature and the SiH_4 pressure, which is typically below 0.2 bar. The cluster sizes can be consequently controlled with the deposition time. The crystallinity of the silicon dots obtained with this technique has been confirmed by X-ray measurements as well as TEM images, which revealed that nc-Si cores were covered with a thin polysilane shell.[102] Similar nc-Si films with the same crystalline Si core and polysilane shell structure can be also obtained by microwave plasma CVD[103] or PECVD[104] technique, where silane and H_2 are decomposed in a oxygen-free atmosphere. Generally the crystalline fraction of the so-obtained film is relatively high, around 30%, but the low passivation efficiency of this technique does not permit high PL intensities. The amorphous polysilane shell can be replaced by a thin amorphous SiO_2 structure after oxidation by a simple exposition to air or by a thermal oxidation.[101, 103] These results in an increase of the PL intensities due to a better passivation, but with efficiencies still lower than those observed with ion implantation or porous silicon for instance.

Takagi *et al*.[103] produced free nc-Si by means of microwave plasma CVD of SiH_4 and H_2. After the synthesis, the nanoparticles were extracted through a nozzle that enable a better size separation, and were successively deposited on a substrate to form a thin film. The determination of the nc-Si size was performed by X-ray diffraction. A thin amorphous layer constituted mostly of polysilane was found by TEM to surround the nc-Si. This layer was replaced by a SiO_2 shell by an oxidation performed in a humid atmosphere (85%) at 60 °C. As a result it can be affirmed that the nc-Si were strongly oxidized in this case. It is interesting to mention that PL could be only seen in oxidized samples.

ii) Plasma-enhanced chemical vapor deposition (PECVD)

This technique consists in the precipitation of excess silicon atoms in a substoichiometric silicon oxide layer ($SiO_{x<2}$); see Fig. 2.19. The deposition process utilizes a plasma in a high vacuum chamber to enhance chemical reaction rates of the precursors. They are mostly SiH_4 and N_2O, but SiH_4 and O_2 can be used as well.[105] The reaction is as follows: $SiH_4(g) + x\,N_2O(g) \rightarrow SiO_x(s) + 2\,H_2(g) + x\,N_2(g)$ After deposition, the SiO_x films are annealed at high temperature between 700 °C and 1100 °C in an ultrapure nitrogen atmosphere to separate SiO_x into silicon nanostructures which crystallize and amorphous SiO_2. Iacona *et al*.[106] clearly showed that the gas flow ratio of the two precursors, the deposition temperature, which both determine the excess of Si in the layer, and the annealing temperature induce relevant

N₂O →
SiH₄ →   T ~ 600 °C   H₂ →   N₂ →

| SiOₓ₍x<2₎ |
| SiO₂ |
| Silicon wafer |

annealing ~ 1100 °C
→
N₂

| (nc-Si layer) |
| SiO₂ |
| Silicon wafer |
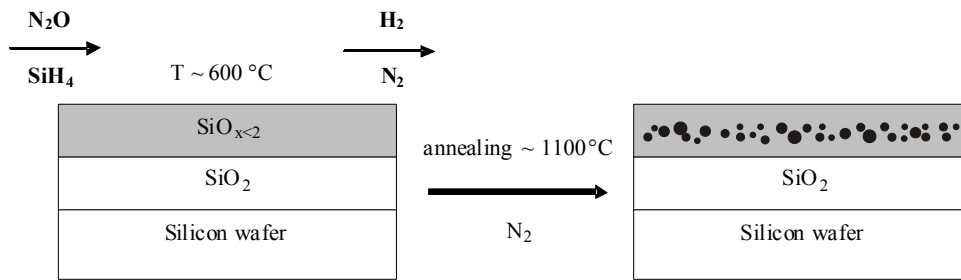
Fig. 2.19. Schematic of the synthesis of embedded nc-Si by plasma-enhanced chemical vapor deposition

changes in the concentration, size and dispersion of the nc-Si. Producing nc-Si embedded in a silicon oxide matrix by PECVD has many advantages. The so-obtained layers are chemically and thermally very stable. It is also possible to control the size distribution of the nc-Si as well as in the ion implantation technique, but the PL yields are, however, clearly lower than those observed with porous silicon or nc-Si produced by ion implantation.

2.2.3.5. Ion implantation

Ion implantation is a promising technique to produce embedded photoluminescent nc-Si because of an easy control of the size distribution that is relatively narrow compared to the others techniques and its high PL efficiency. This technique will be explained in more detail in Sec. 3.1.2., since it is the main synthesis method employed in this work. Si nanoparticles are synthesized by condensation of excess of silicon formed by Si-implantation in a fused silica plate or in a thermally grown SiO_2 layer on a silicon wafer. This is generally achieved by annealing in neutral atmosphere at high temperature, typically between 650 °C and 1100 °C. Because of their large thickness, the films must be prepared to be imaged by TEM, generally by the cross section method. This requires experience, especially for transparent films (see Sec. 3.2.4.). But even this stage completely fulfilled, the nc-Si dots are very difficult to distinguish from the host SiO_2 matrix, and consequently to measure their sizes, because of the small differences of the densities of Si and SiO_2, in spite of the nc-Si crystalline feature. The uncertainty of the size measurement inherent to this method is typically between 0.1 nm for the smallest particles and 0.8 nm for the largest particles (< 6 nm). Besides, the authors[10, 107, 108, 109, 110, 110] relate that no quantum dots smaller than 1.2 nm can be seen, this is explained by the TEM resolution on the one hand and the difficulty to distinguish the nc-Si on the other hand. As a result, the size distribution may be shifted to higher diameters, but this observation still remains below the uncertainty of the measurements itself. Furthermore, embedded nc-Si resulting from the condensation of suboxide silicon films produced either by PECVD[39, 105] or by reactive evaporation of SiO[13] or by cosputtering techniques are usually difficult to image by TEM.[11, 12, 40, 42, 112, 113,114]

2.2.3.6. Sputtering

This technique consists in extracting atoms or molecules from a target, which acts as an electrode, by an argon ion bombarding, and subsequently depositing them on a substrate that acts as counter electrode. In the intense electromagnetic field (~kV/cm²) created between the target and the substrate, which face each other, a glow discharge is initiated and maintained.
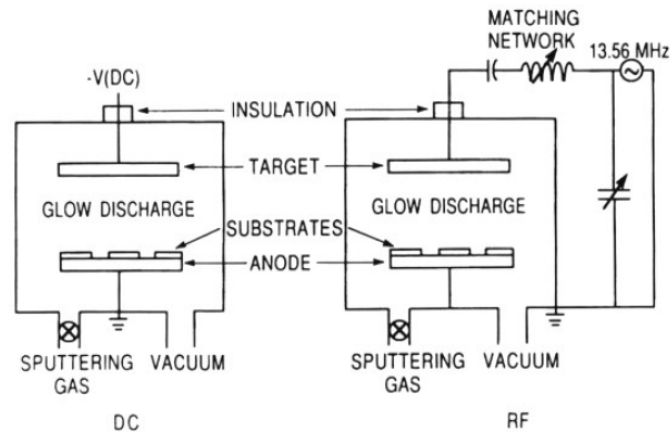
Fig. 2.20. Schematic showing the principles of DC and RF sputtering systems.[115]

Free electrons are accelerated, and if their energy is sufficient, they ionize argon atoms introduced in the low pressure system. The resulting positive ions then strike the cathode (source target) and lose their charge. Neutral atoms are ejected from the target and pass through the discharge and are deposited on the substrate to grow a film. The duration of this process controls the thin film thickness. In order to maintain the discharge and consequently to generate a plasma between the two electrodes, an alternative radio frequency generator (RF) – typically in the range of 5 to 30 MHz – is applied to the target (see Fig. 2.20). In this case, a RF sputtering system allows the deposition of non-conductive materials what DC cannot. Magnets are also used to enhance the sputtering rate, by increasing the ionizing effect of magnetically trapped electrons. Their use provides the advantage of trapping not only electrons, but also charged species at the target, so that they do not hit the substrate, with an improvement of the film quality.

i) Free nc-Si produced by sputtering

Furukawa and Miyasato[116] produced free nc-Si by RF magnetron sputtering in hydrogen gas onto a cooled (~100 K) substrate using a silicon disk target. The thin films were characterized by Raman spectroscopy which proved that the Si dots were crystalline and by infrared absorption spectroscopy which showed that nc-Si are certainly passivated by polysilane. But no PL could be observed.
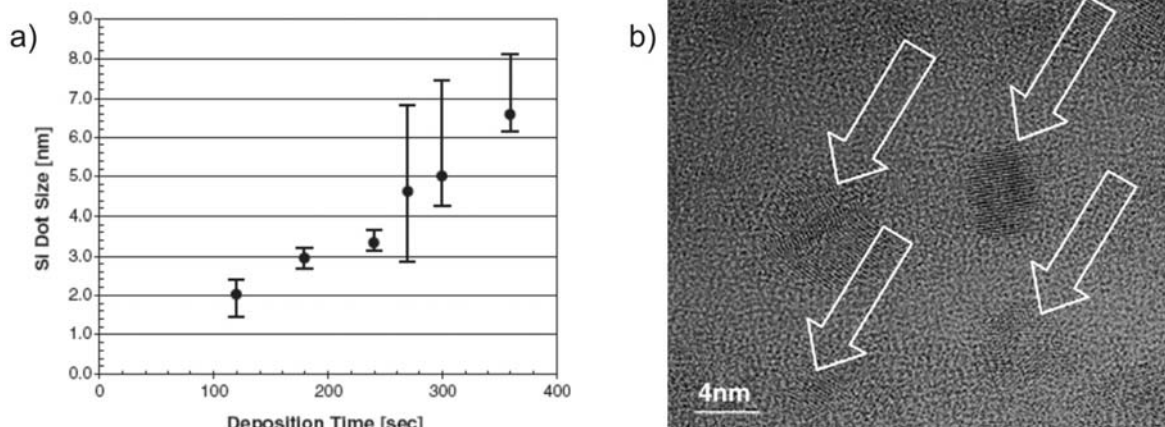
Fig. 2.21. a) Dependence of quantum dot size distribution on deposition time as measured by HRTEM. b) HRTEM images showing individual Si nanocrystals by Conibeer *et al.*[114]

ii)   Embedded nc-Si produced by cosputtering or reactive sputtering

Embedded nc-Si can be synthesized by precipitation of excess Si contained in a non-stoichiometric $SiO_{x<2}$ film. This is achieved by an annealing at a high temperature in the range of 500 °C to 1150 °C. Two methods are generally employed to produce these films. The first one uses two target plates of SiO_2 and Si, which are simultaneously sputtered (cosputtering).[40, 114, 117] With this method, the nc-Si size obtained after annealing depends directly on the thickness of the thin $SiO_{x<2}$ films which can be simply controlled by the sputtering duration. Fig. 2.21.a shows the dependence of nc-Si size on deposition time, where diameters were evaluated by the analysis of HRTEM images as displayed in Fig. 2.21.b. This method has also the advantage that it ispossible to fabricate doped nc-Si/SiO_2 films by addition of a third target plate containing, for instance, erbium,[118] phosphorus[41] or boron.[42] The second method uses only one target (silicon) but in an Ar/O_2 atmosphere. The oxidation of silicon is taking place in the sputtering phase and can be controlled by the flow of O_2 in the system chamber (reactive sputtering).[119, 120] These techniques have many advantages, like the possibility to dope the samples directly in the preparation and to fabricate a sandwich structure of nc-Si layers separated by a thin SiO_2 layer, but the size distribution is not narrow and the PL yield is fairly weak.

2.2.3.7.   Other techniques

Free nc-Si arising from porous silicon were investigated since Canham[4] demonstrated in 1990 that this material can emit bright red PL at room temperature when illuminated with UV light. Although the PL efficiency of such prepared nc-Si is rather high, one can question the quality of the silicon nanostructures that are intensively chemically attacked. Von Behren *et al.*[121] produced porous silicon by electrochemical etching of a crystalline silicon wafer in an aqueous HF solution that consisted of ethanol, water, and 10% hydrofluoric acid (HF). Free nc-Si were removed from the porous silicon film from the substrate by an electropolishing step. The samples were gently oxidized by exposure to air, but, as it has not been explicitly mentioned, the PL and size measurements were probably not performed directly after production.

Synthesis of thin suboxide $SiO_{x<2}$ films by reactive evaporation of SiO in a high vacuum chamber followed by a high temperature annealing is a straightforward method to produce nc-Si embedded in SiO_2. In their study, Kahler and Hofmeister[13] demonstrated for the first time a clear correlation between the presence of nc-Si and the luminescence properties of such films. Their intense luminescent films were imaged by HRTEM after a combined mechanical and ion beam thinning preparation. The so-evaluated size distributions were found to be similar to or even narrower than those observed in films prepared by ion implantation.

2.2.3.8.   Conclusion

The various techniques described here enable one to produce either free nc-Si (laser ablation, laser pyrolysis of silane, MPCVD, aerosol technique, sputtering, and nc-Si originated from porous silicon) or nc-Si embedded in SiO_2 (PECVD, ion implantation, cosputtering, and reactive evaporation of SiO). Since the main criterion to estimate the quality of the produced samples should be their PL yield and size distribution, laser pyrolysis of silane seems thus to be

the most effective technique to synthesize free nc-Si. Its efficiency yield is higher than that of other methods. It can be partly explained by the fact that silicon atoms nucleation is done within a gas flow, which expands in a high vacuum chamber preventing the insertion of impurities, as opposed to laser ablation, sputtering, and MPCVD, which require the presence of gas inside the reaction chamber. Besides, in this technique, the size separation is performed directly through the dynamics of the gas flow in contrast to the aerosol technique and nc-Si arising from porous silicon which both require some more complex methods, during which impurities can be inserted at least at the nc-Si surface.

Production of nc-Si embedded in SiO_2 by ion implantation is believed to be the most effective method and it presents many advantages. The luminescence yield of the samples is close to those produced by laser pyrolysis of silane. Silicon ions are implanted in vacuum in contrast to the cosputtering technique, or the reactive evaporation of SiO. Si nanoparticles can be homogeneously distributed on a large surface with a narrow size distribution. Moreover, the reproducibility of this method as well as the possibility to dope the samples were essential in this work.

2.2.4. Size dependence of PL emission energy

PL from nc-Si has been observed by many authors between 575 and 1095 nm (2.15 and 1.13 eV) for diameters ranging from 1 to 10 nm. But no PL has been seen for smaller and larger particles. In Fig. 2.22, various experimental results of maximum positions of PL spectra of nc-Si in terms of energy compared to their size are reported. They are classified according to their production techniques. For more details on the PL and size measurements, and the production techniques, these results are summarized in Appendix A. In spite of the fact that the behavior of the PL energy of nc-Si as a function of size is apparently separated in two trends, the decrease of the energy with the size, observed in both cases, remains a confirmation of the quantum confinement model. The existence of these two trends was already noticed elsewhere but remains unexplained.[122]

The upper trend comprises the measurements of Sa'ar et al.[12] (nc-Si embedded in SiO_2) and the measurements of Patrone et al.[91] and those from our group[37, 72, 89, 94] (free O-passivated nc-Si oxidized by a simple exposition to air) that are depicted in red in the graph. This trend is in accordance with theoretical calculations of H-passivated free nc-Si.[5, 66] One can notice that some values reported by Patrone et al. and Ledoux et al., for sizes below 3.2 nm, follow the dashed line that represents the effect of oxidation reported by Wolkin et al.[71] In smaller free nc-Si, the recombination of excitons would originate new electronic states in the band gap of nc-Si induced by surface states caused by the formation of Si=O bonds (see Sec. 2.2.2.1.).

The lower trend (*gray curve*) is composed of either free nc-Si strongly oxidized or nc-Si embedded in SiO$_2$ which are all depicted in blue. The strong oxidation of free nc-Si was achieved either by annealing in O$_2$ at high temperature (700 - 1000°C),[97] or by exposition to a humid atmosphere (85%) at 60 °C,[103] or by an original method where particles were passivated with a tetraethylorthosilicate-derived oxide at high temperature (300 – 1000 °C),[95] or probably during the production process.[14] Anyhow, in these cases, the relative thicknesses of the SiO$_2$ shell observed by TEM were generally found to be larger (25 to 50% of the total diameter) than those observed with free nc-Si softly oxidized in air (8 to 16%);[72] see Appendix A. The particle with a 7.8 nm-diameter crystalline core from Schuppler *et al.* was found to have only a relative SiO$_2$ thickness of 9% and it is thus depicted in red. Suboxide silicon films SiO$_{x<2}$ produced either by cosputtering, PECVD, evaporation of SiO, and ion implantation techniques, were
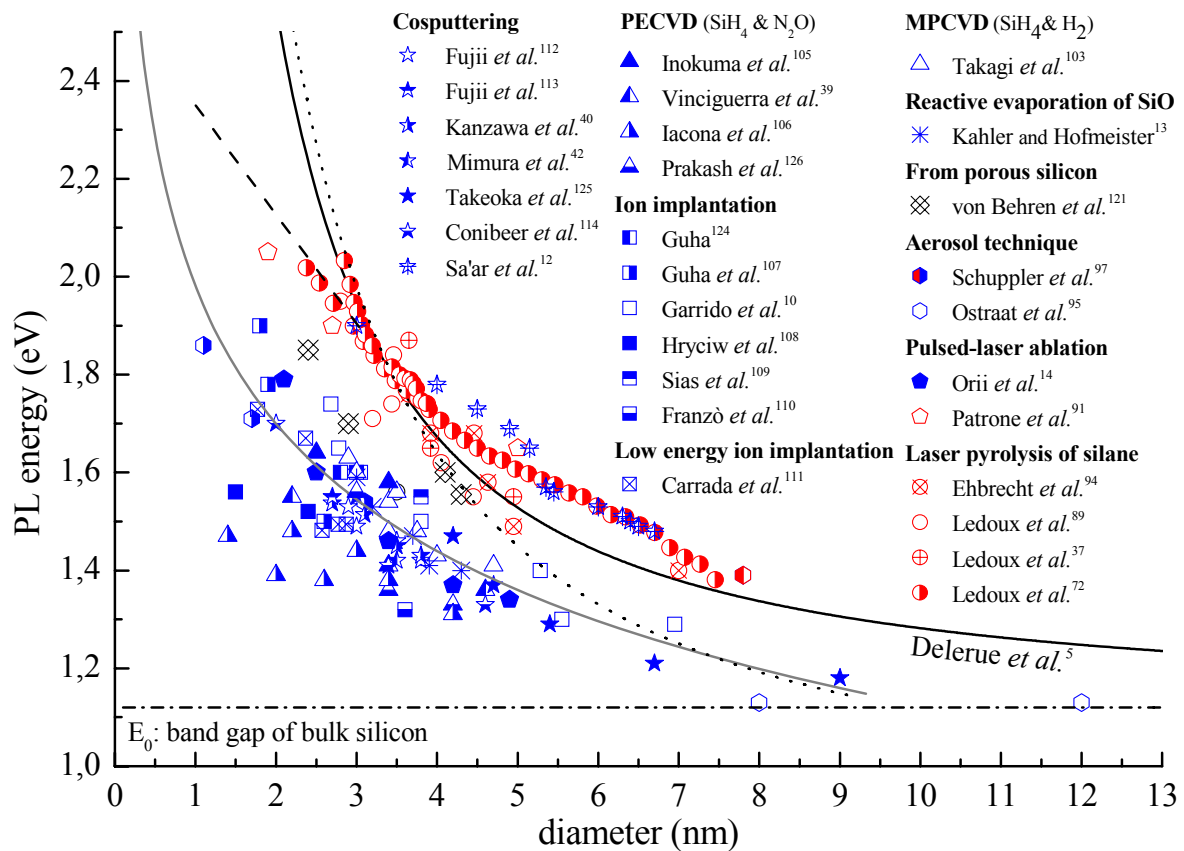
Fig.2.22. Maximum positions of PL curves of nc-Si in terms of energy as a function of the diameter of the crystalline core as obtained in various experiments. The values are sorted by production techniques: the stars refer to cosputtering, the triangles to chemical vapor deposition (PECVD and MPCVD), the squares to ion implantation, the asterisks to reactive evaporation of SiO, the diamonds to nc-Si resulting from porous silicon, the hexagons to aerosol technique, the pentagons to pulsed laser ablation, and the circles to laser pyrolysis of silane. PL and size measurements of free nc-Si resulting from fresh samples, gently oxidized after preparation, are plotted in red, whereas values regarding nc-Si embedded in SiO$_2$ or resulting from strongly oxidized samples are plotted in blue. The black curves arise from a fit of theoretical calculations of H-passivated nc-Si from Delerue *et al.*[5] (*continuous line*), whereas the gray curve that concerns the lower trend is shown to guide the eye. The horizontal dash-doted line displays the band gap of silicon E_0 at room temperature. The dashed line, which comes off the theoretical curve of Delerue *et al.*, depicts the effect of oxidation on free nc-Si preliminarily passivated with hydrogen reported by Wolkin *et al.*[71] Their observations were in good agreement with the calculations of Delerue for nc-Si passivated with a Si=O bond that were described in the same article. But no decrease of the emission energy has been noticed for sizes larger than 3.2 nm. The dotted curve depicts the effect of compression induced by the presence of an SiO$_2$ layer, which surrounds the nc-Si core, on the PL emission energy as evaluated by Hofmeister *et al.*[88]

annealed at high temperature to form nc-Si embedded in SiO_2 that are generally found to be separated from each other by a SiO_2 layer with a thickness of a few nanometer. A grey curve is displayed in Fig. 2.22 to show the second trend, which is formed by more than 70 values that are all depicted in blue. Nevertheless, it seems that some divergent measurements should be excluded (PECVD).[106] Values resulting from porous silicon samples studied by von Behren *et al.*[121] are depicted in black because the degree of oxidation has not been clearly expressed, for the sake of completeness.

For identical sizes, nc-Si that belong to the lower trend emit light with lower energy than those in the upper trend, and the energy losses seem to be more pronounced for smaller nc-Si than for larger ones. For instance, the energy loss is about 0.4 eV for nanoparticles size of 3 nm whereas it is only about 0.13 eV for nc-Si with a diameter of 7 nm. Strikingly, for the same emission energies, nc-Si of the upper trend are apparently about two times larger than in the lower trend.

One can first suggest that these two trends result from systematic errors in the determination of the nc-Si sizes and/or the PL peaks maxima. It has already been observed[39, 123] that the PL of larger nc-Si becomes saturated more quickly when the excitation intensity increases. This effect result in a blue shift up to ~0.1 eV in the PL spectra (see Sec. 4.2.2.3.). Nevertheless, in every reported article, it seems that PL measurements were performed at low excitation energy density regime to avoid this effect (see Appendix A). However, most of the measurements were performed with a continuous source excitation which could result in the same effect (see Appendix A). However, one can definitively dismiss this assumption since the values reported by Ledoux *et al.*,[72] which belong to the upper trend, were obtained with a low excitation intensity with a pulsed excitation source in order to avoid any shift to high energies. The PL of nc-Si depends also on the excitation emission energy as described by Guha.[124] PL peaks shift to higher wavelengths with increasing the excitation wavelength. The position of the PL peaks varies in a roughly linear relationship with a proportional factor $k = 0.1$ nm/nm. In the reported articles, the excitation wavelengths are ranging from 266 to 514 nm, which would correspond to a maximal deviation of the peak positions of only 70 meV. Moreover, no correlation between the excitation energy and the maximum emission energy is seen (see Appendix A). In conclusion, we exclude any systematic error on the PL measurements regarding the excitation energy and excitation intensity dependence on the PL.

For the greater part, nc-Si diameters were determined by TEM (see Appendix A), which implies a delicate preparation of the samples, especially for nc-Si embedded in SiO_2 films (see Sec. 1.2.3.5. and 4.1. and 4.2.1.4.). The size distribution can be easily shifted to higher diameters because of the fact that smaller clusters are more difficult to be imaged than larger ones. Besides, it has been several times reported that clusters smaller than 1.2 nm could not be observed by TEM, which should accentuate the shift to larger sizes. Nevertheless, the assumption of a systematic error caused by the TEM preparation and/or imaging should be dismissed. On the contrary, the lower trend that is mainly composed of nc-Si embedded in SiO_2 should be logically shifted to larger size compared to the upper trend.

As the lower trend is only constituted of strongly oxidized free nc-Si, *i.e.* with a relative thick SiO_2 surrounding layer, and nc-Si embedded in SiO_2, one can suggest that the SiO_2 embedding is responsible for the red shift in the emission spectra compared to the upper trend that is, *a contrario*, mainly composed of gently oxidized free nc-Si. The SiO_2 embedding should imply three inextricable aspects. The formation of silicon-oxygen bonds at the nc-Si surface, the presence of a SiO_2 matrix in the surrounding, and the compression induced by the silicon-oxygen bonds and/or the presence of a SiO_2 matrix. Wolkin *et al.*[71] have demonstrated experimentally and theoretically that the oxidation of pre-H-passivated nc-Si causes an energy loss in the PL emission spectra (dashed line) but only for sizes smaller than 3 nm. It has been attributed to the formation of Si=O bonds at the nc-Si surface. This effect has been confirmed by other theoretical studies, which concerned unfortunately only particles smaller than 2 nm.[67, 68, 69, 70] Besides, Draeger *et al.*[68] have shown that the energy loss increases with the number of Si=O bonds. In their *ab initio* study, Luppi and Ossicini[67] have demonstrated that the presence of an embedding SiO_2 structure induces also a significant energy loss of the band gap of nc-Si. Finally, it has been theoretically[68] and experimentally[87] shown that compression of nc-Si induces a significant decrease of the PL emission energy. Moreover, a lattice distance shrinking, which accrues with the SiO_2 layer thickness, was observed by Hofmeister *et al.*[88] and was understood as an effect of compression. In the article of Ledoux *et al.*,[89] they associated these observations with the effect of compression on the PL spectra reported elsewhere[87] to evaluate the effect of the SiO_2 layer thickness on the PL spectra maximum. It is striking to note that the resulting formula seems to be in good agreement with the lower trend from particles with diameters larger than 7 nm; sizes which had the largest SiO_2 shell thickness. One can suppose that in a host matrix the compression on nc-Si is independent of the nc-Si size and remains close to the maximal value.

Surprisingly, nc-Si embedded in SiO_2 seems to be also present in the upper trend.[12] But, one can reasonably question those values since they are in contradiction with the results of more than 10 different research groups, among which some groups have employed the same synthesis technique (cosputtering).

The quality of the production technique acts certainly on the defect concentration of nc-Si that influences the position of the PL spectra. Since, for a fixed homogenous defect concentration, the probability of defected-free nc-Si is higher for smaller nc-Si than for larger ones (see Fig. 2.10) an increase of the defect concentration will consequently shift the PL spectra to the blue (higher energies). This argumentation seems to be incompatible with the fact that samples produced by laser pyrolysis of silane have a strong PL yield, and with the fact that it cannot explain the presence of two distinct trends, *i.e.,* in other words, two distinct defect concentrations.

Finally, it can be asserted that neither systematic errors, nor the quality of the studied samples seem to be responsible for the presence of two trends in the behavior of the size dependence of the PL of nc-Si. We rather think that the SiO_2-embedding strongly affects the PL energy of nc-Si.

2.2.5. Conclusion

Many researchers are trying to clarify experimentally and theoretically the origin of the strong Vis-NIR PL of silicon nanostructures. However, the mechanism of the PL is still unclear. From the various models that were briefly exposed in Sec. 2.2.2., the quantum confinement effect remains the most believed theory to explain the luminescence properties of nc-Si, in particular the size dependence of the energy emission. Nevertheless, this theory remains a first approach to explain the experimental observations which were done on samples where several phenomena can simultaneously occur. And the existence of two experimental trends in the size dependence of the energy emission can have many reasons.

The discovery of luminescent silicon nanostructures opened new fields on optoelectronics based on silicon. Attempts have been made to produce lasers based on nc-Si,[127] but it seems that no light amplification has been yet clearly established. The optical properties of nc-Si are expected to be used in the fabrication of quantum memory devices,[128] for luminescent biological labelling,[129, 130, 131] in the fabrication of photovoltaic solar cells,[114] and in the fabrication of optical amplifier media of the 1535 nm erbium emission that is employed in telecommunication technology.[18, 132]

3. Experimental methods

3.1. Production techniques of luminescent silicon nanocrystals

Free silicon nanocrystals and nc-Si embedded in quartz were produced by two different techniques. Free nc-Si were produced by laser pyrolysis of silane in a gas flow reactor. In this technique, nc-Si were extracted from the reaction volume through a conical nozzle to form a cluster beam. The nanoparticles were either deposited on quartz substrates that were placed directly into the cluster beam or they were deposited on a paper filter. An example of a paper filter covered with nc-Si is given in the Fig. 3.3, where two photos of the same filter illuminated by normal and UV light are presented. Embedded nc-Si were produced by Si implantation in fused silica windows and subsequent annealing at high temperature by using the facilities provided by the Institut für Festkörperphysik in Jena. Some samples were also implanted by the Ion Beam Service company in Marseille.

3.1.1. Laser pyrolysis of silane

The free nc-Si were synthesized by nucleation of silicon atoms generated by CO_2-laser-induced decomposition of silane (SiH_4) in a gas flow reactor, as described by Ehrbrecht et *al.*[94] Figure 3.1 shows a schematic view of the experimental setup consisting of the cluster beam source and the elements used for deposition. The apparatus contains a laser-driven flow reactor incorporated into the source chamber of a molecular beam machine and a time-of-flight mass spectrometer (TOFMS). A stainless steel tube admits the reactant gas (SiH_4) to the center of the flow reactor where it is crossed with a focused pulsed CO_2 laser beam. A coaxial outer tube with a larger diameter drives a helium gas flow that enables a confinement of the reactant gas to the apparatus axis and a laminar circulation. The pressure in the source chamber is about 5×10^{-3} mbar. In the flame resulting from the pyrolysis of silane, silicon atoms condense and nucleate rapidly to form nc-Si with a typical size of 3–7 nm. The clusters are extracted perpendicularly to the plane formed by the gas flow and the CO_2 laser beam through a conical nozzle. Finally, a skimmer placed in the entrance of a pressure-reducing differential chamber ($\sim 10^{-5}$ mbar) makes it possible to form a molecular beam of freely propagating nanoparticles.
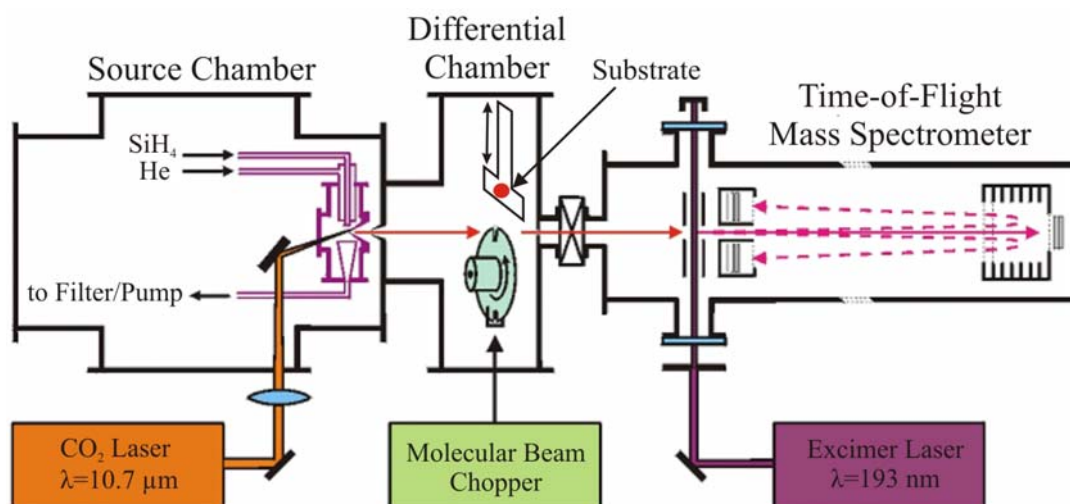
Fig. 3.1. Schematic view of the silicon cluster beam reactor.
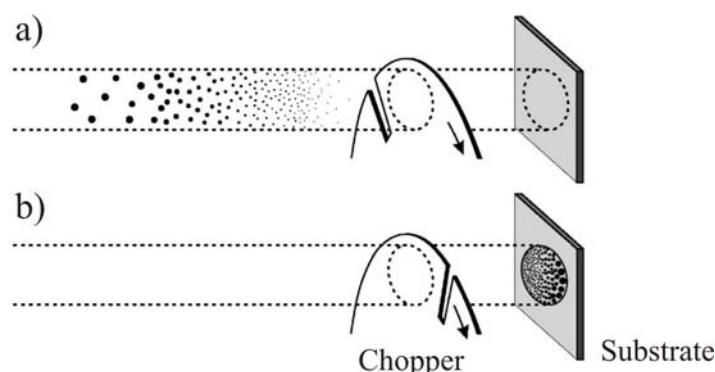
Fig. 3.2. Schematic of the size selection of nc-Si resulting from a cluster beam, according to Ledoux *et al.*[72] Upper panel (a) displays the size separation of particles according to the different velocities in the pulsed beam. Lower panel (b) reflects the situation when the particles have already passed the chopper slit.

The nc-Si are generated during the short pulse (20 ns) of the CO_2 laser, and as a result, the particle beam is emitted in a pulsed mode. Due to the size-dependent velocity of the extracted particles, a separation of the different sizes occurs, as displayed in Fig. 3.2.a. Thus, employing a molecular-beam chopper with proper synchronization to the CO_2 laser, it is possible to select a specific size from the entire cluster pulse so that only this size can be transmitted and subsequently deposited on a quartz substrate. In this way, due to the continuous rotation of the chopper slit, the different sizes are deposited at different locations on the substrate. The sizes continually change from small particles on the left to large particles on the right as shown in Fig. 3.2.b.

If the substrate is moved out of the cluster beam, the particles reach a Whiley-McLaren-type TOFMS chamber ($\sim 10^{-8}$ mbar), where they are ionized by the 193 nm-radiation of an ArF-excimer laser and subsequently accelerated between two series of high voltage plates. Finally after passing another accelerating grid at the end of the chamber, the ionized particles are detected by a pair of microchannel plates. Time-of-flight mass spectra are obtained by storing the detected ion signals as a function of their arrival time at the detector in a multichannel scaler (EG+G ORTEC, model T914). The flow rates of silane and helium, the vacuum pressures of the different chambers, the position of the focused CO_2 laser beam as well as its energy density, are important parameters that influence the synthesis of the nc-Si. The size distribution of nc-Si on the substrate, which depends also on the substrate position, as well as the rotation frequency of the molecular beam chopper, can be evaluated by the con-
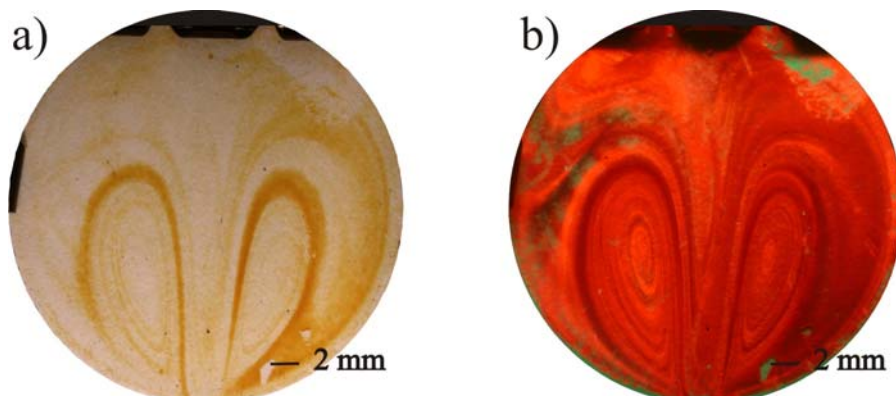
Fig. 3.3. Photos of a paper filter covered with silicon nanoparticles. The left picture (a) was taken under normal sunlight while, for the right picture (b), UV light illumination ($\lambda = 254$ nm) was used.

version of the measured time-of-flight distributions as reported in the previous articles dedicated to the study of the optical properties of nc-Si carried out by the Huisken group.[94, 37, 72, 89]

Directly after production, the samples exhibit no PL under UV radiation, and they must to be exposed to air for several months before they show strong luminescence which is visible with the naked eye, as presented in Fig. 3.3. Moreover, Ledoux *et al.*[72] have shown that a full passivation is reached after approximately 6 months. During this period a silicon oxide shell is formed and, as a consequence, the diameter of the crystalline core is reduced by a factor of about 90% compared to its original value.

3.1.2. Ion implantation

The ROMEO implanter (High Voltage Engineering Europa B. V.) of the Institut für Festkörperphysik, Friedrich-Schiller-Universität Jena, was employed to perform the Si implantation in two different kinds of SiO_2 samples: (1) 0.2 or 0.5-mm-thick fused silica quartz windows (Heraeus Suprasil 1) and (2) 300 nm-thick silicon dioxide layers thermally grown on silicon wafers (Crystec). The silicon isotope ^{28}Si has been used for the implantations which were performed at room temperature in a high vacuum chamber ($\sim 10^{-7}$ mbar). In the ion beam source, silicon atoms are produced in three steps: (*i*) silicon tetrafluoride (SiF_4) is decomposed by heating, (*ii*) the resulting atoms and molecules are ionized by a high-voltage discharge, which are subsequently accelerated by a high-voltage plate (30 keV). Then, (*iii*) a mass separation is performed by a magnetic analyzer. However, as the N_2 molecule has the same mass as the silicon isotope ^{28}Si the ion beam source has to be completely leakproof to avoid an unwanted implantation of nitrogen. After that, the charged ions are accelerated by a second high-voltage grid where the voltage can be adjusted up to a maximun of 400 keV. The charged ions penetrate into the samples with high energy and create a current (around 3 µA in the present study) in the target which is directly measured to determine the ion fluence. The target is oriented at an angle of 7° with respect to the ion beam axis. After implantation, the transparent fused silica windows are slightly darkened. This can be explained by the creation of damages in the SiO_2 structure and also by the presence of an excess of silicon.

The implanted samples were subsequently annealed at high temperature in neutral nitrogen ambient to avoid oxidation. The temperature and duration were typically 1100 °C and one hour, during which the excess Si condensed rapidly and nucleated to form nc-Si. Annealing represents a thermal process, the purpose of which is to prevent the formation of undesirable stress inside glass, and, especially in this case, to remove the stress resulting from ion implantation. Figure 3.4 shows the temperature measurements of the oven and the sample holder during an annealing cycle that consists of three stages: (*i*) the temperature rises (product heating) to the upper-limit annealing temperature. (*ii*) The temperature is extended (annealing and stabilization) over the sample for a certain time at the upper limit annealing temperature. The temperature variations inside the sample must be equalized and the stress decreased. (*iii*) The temperature drops (cooling) at a slow annealing speed up to the ambient temperature. This period is essential to avoid the formation of constant residual stress.
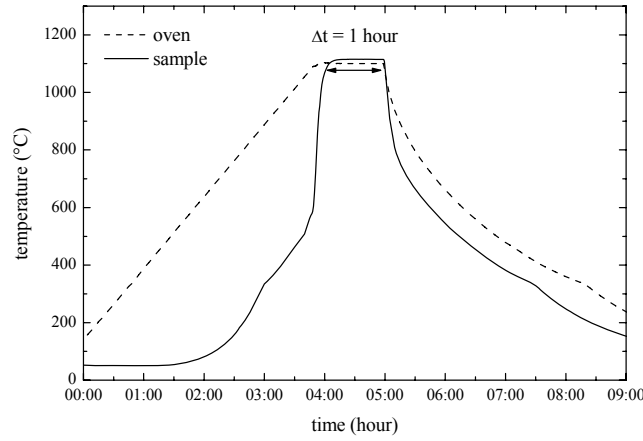
Fig. 3.4. Temperature behavior of the sample holder and the oven during an annealing cycle performed at 1100 °C in a constant N_2 gas flow with a duration $\Delta t = 1$ hour.

The excess silicon atoms concentration profile in the implanted SiO_2 layers was simulated by Monte Carlo calculations (SRIM-2003 code[133]). For an implantation energy of 100 keV, the concentration profile peaks at 150 nm with a full width at half maximum of 110 nm. And, for a fluence of 1×10^{17} ions/cm^2, a maximal of Si excess atomic concentration of 8.5×10^{21} atoms/cm^3 is expected. During the subsequent high-temperature annealing, the extra Si atoms redistribute and some fractions precipitate into nc-Si which exhibit PL under UV illumination. Note that the average size of the nc-Si can be evaluated by following the relation of the lower trend of the size dependence of the emission energy (see Fig. 2.22), since samples produced by ion implantation partly follow this trend. For instance, a fused silica window implanted with Si at 100 keV with a fluence of 1×10^{17} ions/cm^2 and subsequently annealed at 1100°C during one hour gives rise to luminescence with a maximum position of the spectrum at 1.55 eV, which corresponds to an average size of 2.9 nm. Since the number N of silicon atoms, which constitute one silicon nanoparticle with the diameter d (nm), can be evaluated following the relation $N = 4/3 \, \pi \, (d/2)^3 \, V/8$ where $V = 0.1601$ nm^3 is the volume of a unity cell in bulk silicon which is composed of 8 atoms, the nc-Si concentration then corresponds to 1.3×10^{19} /cm^3. This represents 17% in the SiO_2 volume.

3.2. Characterizations

Among the various characterization techniques employed in this work, PL measurements were used for all samples, whereas Rutherford backscattering spectrometry (RBS) and optical transmission spectroscopy were used only for some samples produced by ion implantation. Some samples were imaged by transmission electron microscopy (TEM) to evaluate the size distribution of the nc-Si.

3.2.1. Photoluminescence

Crystalline silicon nanoparticles are photoluminescent because they are able to emit photons after they have been excited with photons having sufficient energy. The different processes involved in the physics of PL are sketched in Fig. 3.5. The absorption of a photon the energy of which is higher than the band gap of silicon will enable the transition of an electron from the valance band to the conduction band, which creates as a consequence a hole in the valence band. Because of the rapid ($\sim 10^{-13}$ s) thermalization of photoexcited carriers, the
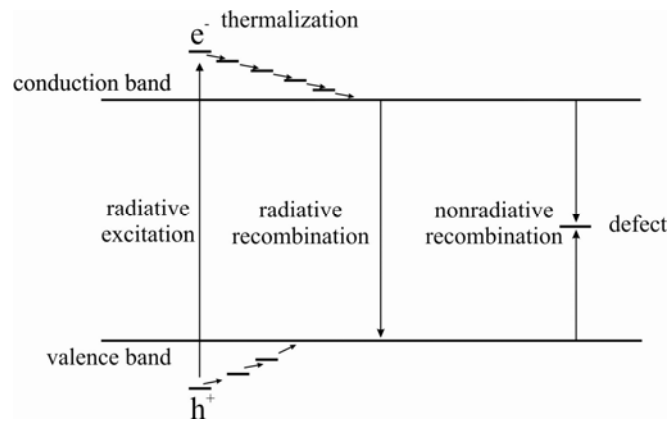
Fig. 3.5. Schematic of photoluminescence process

electron and the hole will subsequently reach the minimum of the conduction band and the maximum of the valence band, respectively. Because of the band structure of silicon, the minimum of the conduction band does not occur at the same wavevector as the maximum of the valence band (see Sec. 2.2.1.). The recombination of the electron-hole pair (exciton) requires a third entity (lattice vibration called phonon) to overcome the offset of momentum. However, such combined transition (phonon-assisted recombination) has a very low probability. Therefore, silicon (indirect band gap semiconductor) is inefficient at emitting light. When carriers are confined, their wave functions spread out and the band structure is said to become more direct-like, and thus luminescence more efficient. However, non-radiative recombination can still take place at point defects or at dangling bonds at the nanoparticle surface. PL radiation of nc-Si is isotropic and takes place in a few µs at room temperature.

The schematic of the dedicated self-made PL spectrometer used to study the PL behavior of nc-Si under UV excitation is presented in Fig. 3.6. The fourth harmonic ($\lambda = 266$ nm) of a pulsed Nd:YAG laser (Continuum Minilite II, pulse width: 4 ns, maximum energy at 266 nm: 4 mJ per pulse) is used as excitation source. In order to avoid saturation effects, the UV laser beam is always attenuated to energy values below 10 µJ/pulse by using a polarizing prism. The energy of the laser beam is detected by an energy sensor (Coherent, model J5-09) which is coupled with a joulemeter (Coherent, model EPM1000). A UV color filter (UG5) is employed to block the remaining fundamental and second harmonic emission wavelengths of the laser at 1064 and 532 nm, respectively. Since, for homogenous samples the PL intensity can be simply increased by increasing the irradiated surface, the laser spot size is adjustable by the use of a removable pinhole. Otherwise a spot size of 1 nm is generally employed.

The PL emanating from the excited spot is collected by a 60-mm diameter lens with a focal length of $f_1 = 50.8$ mm – *i.e.* with a large lens aperture of $f / 0.85$ – and imaged by another lens with a focal length of $f_2 = 300$ mm on the 4-mm-wide entrance slit of a Czerny-Turner-type monochromator (McPherson, model 218-VUV-Vis-IR). The focal length f_2 is equal to the focal length of the parabolic mirrors of the monochromator to respect the fact that the light which falls into the grating should be collimated. The grating equation $n \lambda = g (\sin\theta_i - \sin\theta_r)$ describes the dispersing property of the grating where n is an integer (the order), λ the wavelength, g the distance between two grooves in the grating, θ_i and θ_r are respectively the angle of the incident and reflected ray to the grating normal. Since this equation
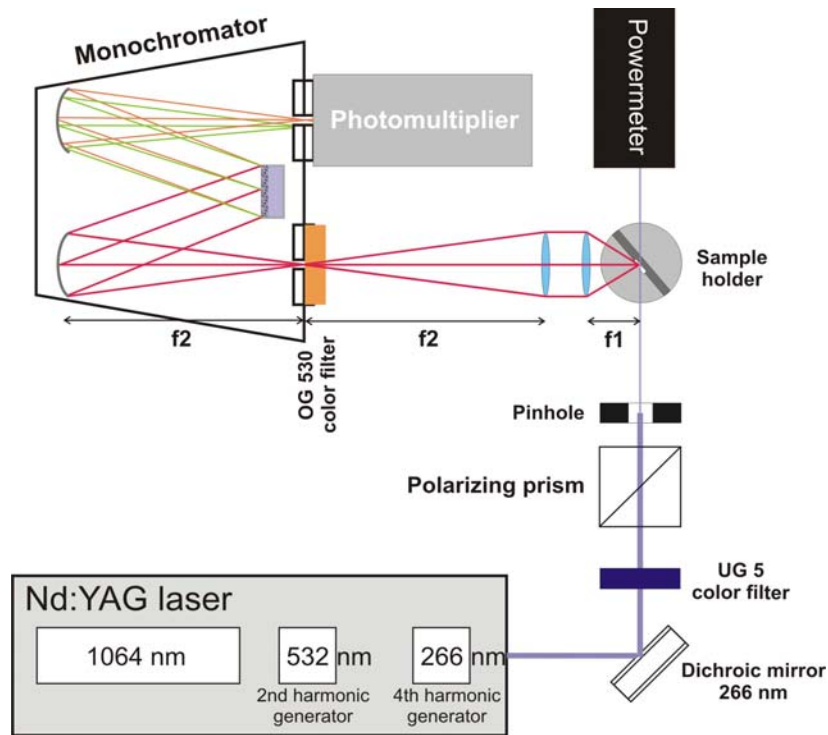
Fig. 3.6. Schematic of the apparatus dedicated to photoluminescence measurements

is fulfilled for different wavelengths, the higher orders have to be suppressed. A second-order effect occurs when light with twice the desired wavelength falls onto the grating. This light is reflected into the same angle as the desired light; hence it comes out of the output slit. Therefore, an orange color filter (OG 530) is placed at the entrance of the monochromator to prevent the occurrence of artefacts in the PL spectra which originate from luminescence at shorter wavelengths.

The dispersed PL is detected by a liquid-nitrogen-cooled photomultiplier (Hamamatsu, model R5509-72) with a spectral response ranging from 300 nm to 1.7 μm and with a detection efficiency maximum in the near-IR (around 1.6 μm). The PL of the nc-Si has been studied in both the spectral and temporal domain. PL spectra are recorded by step-scanning the monochromator and collecting the signal in a computer-controlled gated integrator incorporated into a CAMAC module. The decay of the luminescence upon excitation is measured with a digital oscilloscope (Tektronix TDS520). During the decay measurement, the monochromator is parked at a distinct wavelength.

In order to study the PL on various positions of the samples, the sampler holder is mounted on three micro-positioning stages which enable displacements in all direction. In order to study the temperature dependence of the PL, the sample is mounted on the cold finger of a closed-cycle helium cryostat (ADP DE-204-SL) in a high vacuum chamber ($P \leq 10^{-5}$ mbar). The lowest temperature achieved is 6.5 K.
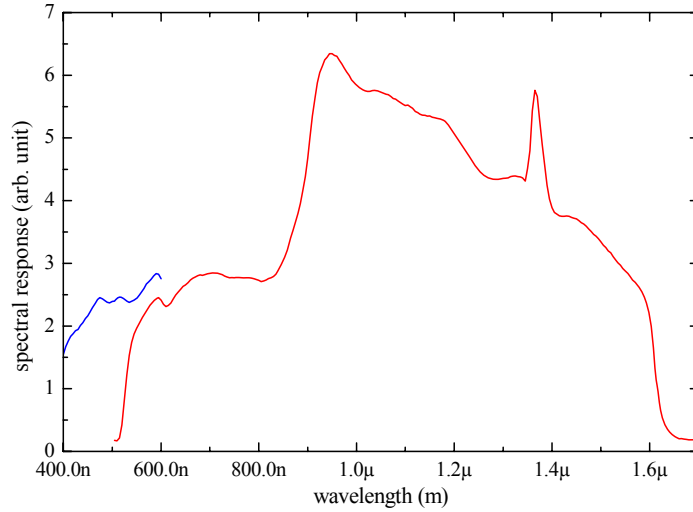
Fig. 3.7. Spectral response $F(\lambda)$ of the PL apparatus using a long-pass filter OG 530 (*red*), and without this filter for blue PL measurements (*blue*).

3.2.1.1. Spectral measurements

The PL spectra are obtained by integrating the area under the PL decay curve for a fixed period of 6 ms. This operation is repeated at every wavelength position determined by the monochromator. The scanning step is 5 nm whereas the theoretical resolution of the monochromator with 4-mm wide open slit approaches 20 nm. The spectra are subsequently corrected by the spectral response of the system shown in Fig. 3.7. The calibration $F(\lambda)$ is obtained by measuring the spectrum $M(\lambda)$ of a halogen lamp (OSRAM HLX 64611, 12 V, 50 W, color temperature of 3200 K) the spectrum of which follows the Planck's law of black body radiation

$$B(\lambda, T) = \frac{8\pi}{hc} \frac{1}{\lambda^5} \left(e^{\frac{hc}{kT\lambda}} - 1 \right)^{-1}.$$

The Planck's law of black body radiation is written here in terms of spectral energy density, where T is the color temperature of the lamp, c is the speed of light, k is the Boltzmann constant, h is the Planck constant, and λ the emission wavelength. The spectral response is finally obtained by dividing the measured spectrum by the theoretical spectrum $F(\lambda) = M(\lambda) / B(\lambda,T)$.

3.2.1.2. Temporal measurements

The time-resolved PL decays are measured by a digital oscilloscope while the monochromator is parked at a distinct wavelength. The decay is averaged over $\sim 10^4$ laser excitations to improve the signal to noise ratio and subsequently digitalized to be analyzed. The temporal resolution is about 5 µs. In Fig. 3.8, a typical time resolved PL decay curves of nc-Si normalized to the initial PL intensity is shown. The non-exponential behavior (notice the logarithmic scale of Fig. 3.8a) is always observed, *i.e.* for all samples, temperatures, and emission energies. The multi-exponential feature of the decay curves seems to be intrinsic for a single nc-Si. Single nc-Si show an emission intermittency, also called blinking, where the PL intensity fluctuates temporally.[134] Similar properties have been observed by Fisher *et al.*[135] and Schlegel *et al.*[136] for the luminescence of CdSe (covered ZnS) and ZnS (covered CdSe) quantum dots, respectively. Besides, they noticed that the decay lifetimes correlated strongly
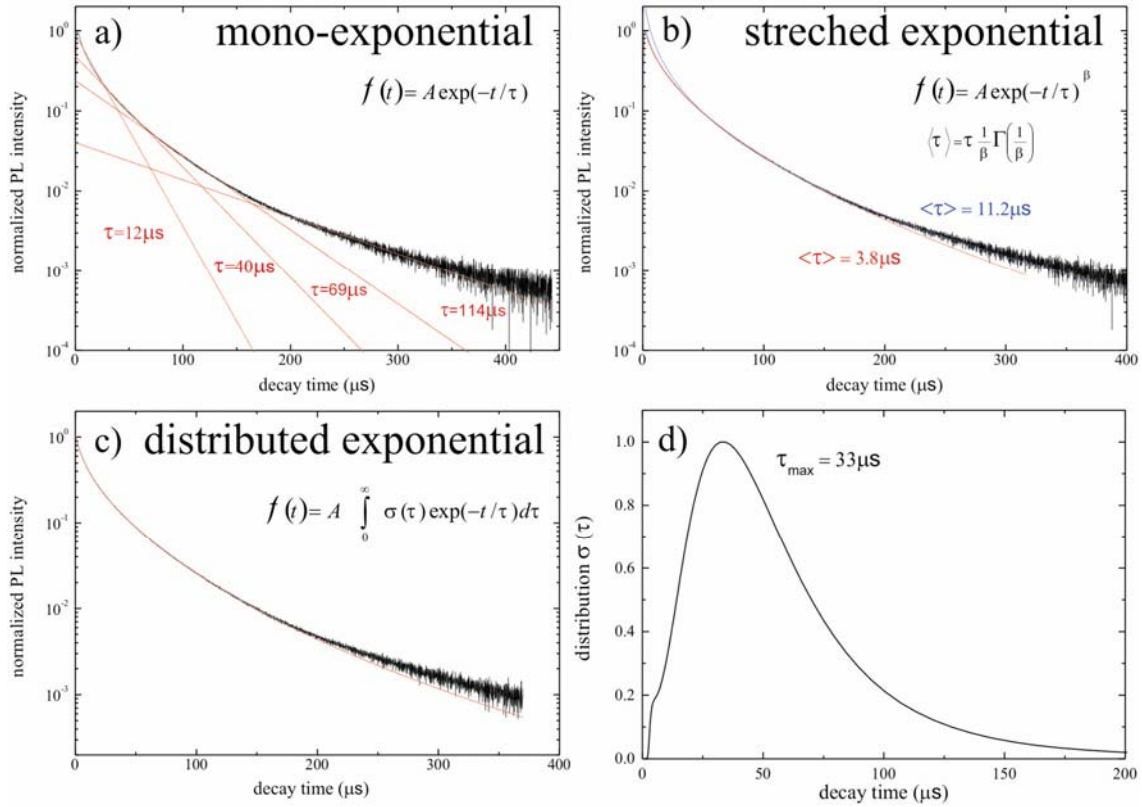
Fig. 3.8. A time resolved photoluminescence decay curve fitted by a) four different mono-exponential functions, b) by two different stretched exponential functions, and c) a distributed exponential function. The corresponding distribution of lifetimes τ is plotted in (d).

with the PL intensity fluctuations where a high fluorescence yield is associated with a long fluorescence lifetime. In particular, at the highest fluorescence intensity, the decay curves were found to approach a single exponential behavior.

In order to analyze the PL temporal behavior, the decay curves are usually fitted by a Kohlrausch function $I(t) = I_0 \exp[-(t/\tau)^{\beta}]$, also called stretched exponential function, where τ is the lifetime and β the dispersion factor.[123, 137, 138] However, it becomes difficult to fit the complete decay curve when the PL decay is measured for 3 or more decades, as it was mostly the case in this work (see Fig. 3.8.b). This problem has already been mentioned by other researchers, and it seems that the use of a distribution of lifetimes gives higher quality fit.[139] Therefore, the decay lifetimes have also been evaluated by fitting log-normal decay rate distributions to the measured data using the maximum entropy method of data analysis (Fig. 3.8.c).[140] However, it must be underlined that there is by no means a unique solution (Fig. 3.8.d) and that the decay curves can be fitted by different distributions of lifetimes.

3.2.2. Rutherford backscattering spectroscopy

Rutherford backscattering spectroscopy (RBS) is based on the measurement of energy of backscattered particles when a material is bombarded with a high-energy ion beam (1 to 5 MeV). This quantitative method enables us to identify and evaluate the different elements present in a thin layer. The JULIA 12-MeV accelerator of the Institut für Festkörperphysik in Jena was employed to generate a high-energy ^{4}He$^+$ ion beam. The direction and energy of backscattered helium ions are modified because of the elastic collision with the atoms of the
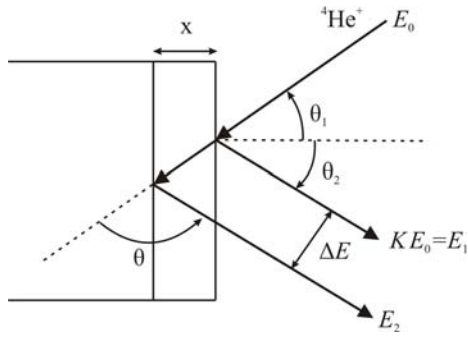
Fig. 3.9. Schematic of Rutherford backscattering spectroscopy. E_0 represents the energy of the incident helium atoms, E_1 is the energy of atoms backscattered at the surface, and E_2 is the energy of atoms backscattered at a penetration depth x.

thin layer. For each element detected, the spectrum gives rise to a peak at different energy, the width of which is proportional to the thickness of the layer and the area is proportional to the density of atoms. The principle of Rutherford backscattering is explained in Fig 3.9. The two important parameters involved in the elastic collision are the kinematic factor

$$K = \frac{E_1}{E_0} = \left\{ \frac{cos\theta + \sqrt{(M_2/M_1)^2 - sin^2\theta}}{1 + M_2/M_1} \right\}^2,$$

and the energy loss

$$\Delta E = KE_0 - E_2 = \left\{ \left(\frac{K}{cos\theta_1}\right) \left[\frac{dE}{dx}\right]_{in} + \left(\frac{K}{cos\theta_2}\right) \left[\frac{dE}{dx}\right]_{out} \right\} Nx.$$

M_1 and M_2 are respectively the masses of the incident atom (helium) and the target atoms, N is the number of atoms per surface unity and $\left[\frac{dE}{dx}\right]_{in}$ and $\left[\frac{dE}{dx}\right]_{out}$ are respectively the energy losses when incident He atoms cross the thin layer x before the collision and after the collision. The implantation profiles were evaluated by the analysis of the RBS spectra using the WiNDF software.

3.2.3. Transmission electron microscopy

Silicon nanocrystals were imaged by Dr. C. Jäger using the JEOL JEM-3010 electron microscope of the Institut für Materialwissenschaft und Werkstofftechnologie in Jena. The determination of the sizes of the crystalline cores of the silicon nanoparticles was made by the analysis of the transmission electron microscopy (TEM) pictures with the Digital Micrograph software from Gatan. The core is easily recognizable and, as a consequence, it is measurable since high resolution TEM enables to visualize the lattice fringes from crystalline silicon structure.

Since the quartz layer containing nc-Si should be thin enough (a few micrometer) to be investigated by electron transmission, the implanted fused silica windows should be prepared. Two different preparation techniques were employed, plane-view and cross-section. The plane-view preparation technique, which was performed in Jena, consists of four steps. At first (i) the samples are cut into some slices (diameter of 6 mm) using a circular diamond saw, (ii) the non-implanted side of the quartz pieces is subsequently polished down to a thickness around 100 μm, (this is done by a surface containing diamonds of 10 μm in diameter), (iii) then the non-implanted side of the samples are dimple-grinded up to a 30-μm deep dimple (GATAN 656 dimple-grinder), (iv) and finally, the resulting dimpled samples are milled by

an argon atom beam up the occurrence of a small hole in the center of the dimple (BAL-TEC RES 100 ion milling apparatus). The third step is very critical since the occurrence of the hole is difficult to control for transparent samples. The hole must be very small in order to obtain some very thin layer (a few micrometers) on its surrounding where nc-Si can be imaged.

Since no silicon nanocrystals were seen with this preparation, some samples were prepared at the Technische Universität Ilmenau by the cross-section technique which consists of five similar steps. At first (*i*) the implanted fused silica plates are cut into two pieces of $1.6 \times 10 \times 0.5$ mm^3 which are subsequently glued together so that the two implanted layers are faced, (*ii*) the resulting samples are cut in some $1.6 \times 0.5 \times 0.5$-mm pieces which are strengthened by a titanium ring, (*iii*) the piece thickness is subsequently reduced to 100 μm by polishing both sides, (*iv*) then each sides are dimple-grinded up to 1 μm, (*v*) and finally the resulting dimpled samples are milled by an argon atom beam up to the occurrence of a small hole in the center.

Free nc-Si produced by laser pyrolysis of silane do not require such a complicated preparation. Powder of nc-Si formed by deposition during the production process are simply scratched off the substrates and subsequently dissolved in a chloroform solution to be finally spread on a copper grid dedicated to TEM measurements.

3.2.4. Optical transmission spectroscopy

Optical transmission spectra were obtained with a Shimadzu 3101 PC double beam automatic scanning spectrophotometer covering the range from 190 to 3200 nm. Optical transmission measurements were performed on ion-irradiated fused silica windows using the facilities of the Otto-Schott Institut für Glaschemie in Jena.

3.2.5. Raman spectroscopy

Raman spectra were obtained by Prof. Paillard from the CEMES-CNRS and the University of Toulouse. The spectra were recorded with a UV-specified Dilor XY spectrometer equipped with a 2400-groves/mm gratings and a liquid-nitrogen-cooled CCD detector. The excitation wavelength was the 363.8-nm line (3.34 eV) of an argon-ion laser which is very close to the first direct electronic transition in silicon (Γ_{25} - Γ_{15} = 3.37 eV). The light was focused to a spot of about 500 μm in diameter and the laser power was fixed to 5 mW, resulting in a power of 1 mW on the sample. No laser heating effects should occur under such condition. In order to detect the weak Raman signal arising from a single thin layer of nc-Si embedded in an amorphous SiO$_2$ matrix, the enhancement of the signal resulting from the nc-Si and the minimization of parasite signal resulting from the amorphous host matrix, are crucial. Raman rules can be exploited as follows. Since the signal resulting from the matrix is polarized, it is greatly reduced when the spectra are recorded in the backscattering configuration and crossed polarization for incident and scattered light, respectively. A single crystal wafer was used as reference to calibrate the spectrometer.

4. Free and embedded photoluminescent nc-Si

4.1. O-passivated free nc-Si produced by laser pyrolysis of silane

4.1.1. Photoluminescence of O-passivated free nc-Si

Figure 4.1.a shows a photo taken under UV illumination of size-selected luminescent free nc-Si produced by laser pyrolysis of silane and deposited on a quartz substrate which was placed into the path of the cluster beam. The size selection was achieved by a molecular beam chopper placed before the substrate (see Sec. 3.1.1.). As can be seen in the PL graph in Fig. 4.1.b, the PL peak maxima vary from 736 to 770 nm while the laser spot is moved from left to right. The widths of the PL spectra are relatively narrow, with a full width at half maximum (FWHM) of about 130 nm, which indicates that the size distribution of nc-Si excited in the 0.5-mm laser spot is rather narrow. Measuring PL spectra on different positions makes it possible to evaluate the horizontal dispersion of the PL peak positions, which is about 24 nm per millimeter. This result is in good accordance with measurements reported by Ledoux *et al.*[72] on a similar deposit, selected in size, where a dispersion of 26 nm per millimeter was ob-
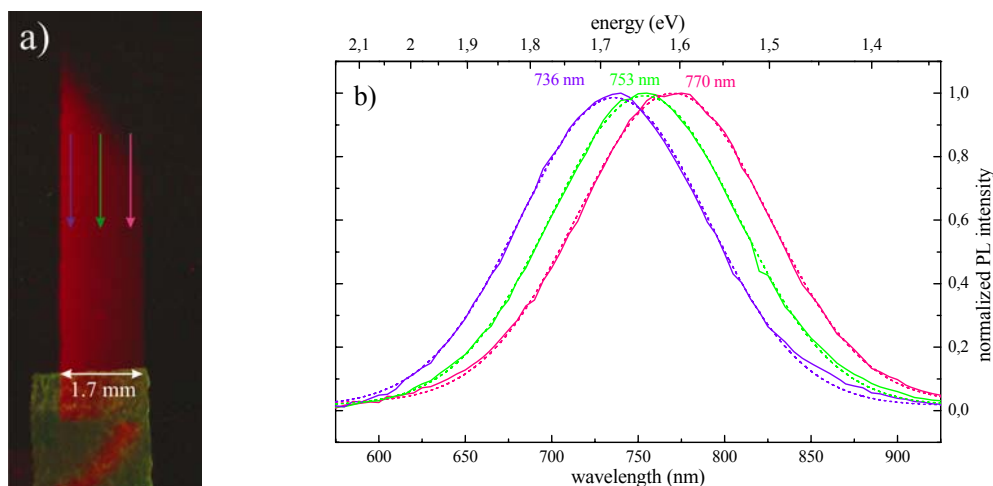
Fig. 4.1. a) Photo taken under UV light illumination ($\lambda = 254$ nm) of free nc-Si deposited on a quartz substrate placed into the cluster beam of the apparatus after a molecular beam chopper (size selection; see Sec. 3.1.1.). The PL was measured on three different positions depicted on the photo by the purple, green, and pink arrows. b) The corresponding PL spectra (*continuous lines*) were fitted with a Gaussian function (*dotted lines*). The sample was excited with the 266 nm light of a Nd:YAG laser with a spot of 0.5 mm in diameter. The excitation energy density was fixed at 130 μJ/cm^2 with a relative standard deviation of 3%.
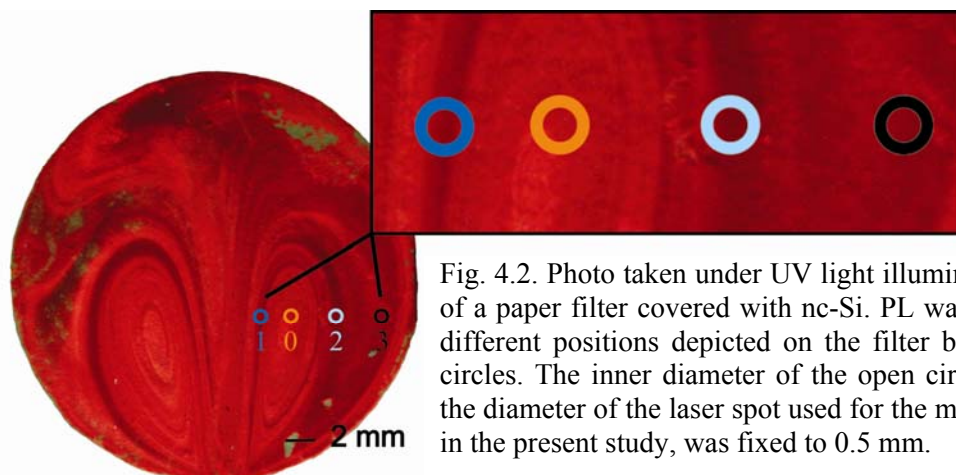
Fig. 4.2. Photo taken under UV light illumination ($\lambda = 254$ nm) of a paper filter covered with nc-Si. PL was measured on four different positions depicted on the filter by the colored open circles. The inner diameter of the open circles corresponds to the diameter of the laser spot used for the measurements which, in the present study, was fixed to 0.5 mm.
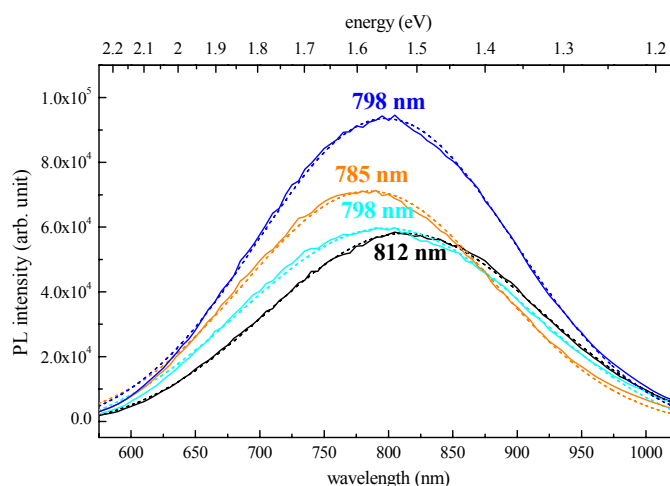
Fig. 4.3. PL spectra (*continuous lines*) measured on the four different positions depicted by the colored open circles in the photo shown in Fig. 4.2. Each spectrum was fitted with a Gaussian function (*dashed lines*) to determine its maximum position and its width.

served. In their measurements, the FWHMs were larger (~ 175 nm) which could be due to the use of a larger excitation area, but the laser spot size was not specified.

In comparison, Fig. 4.2 shows a photo taken under UV illumination of free nc-Si deposited on a dedicated paper filter. In that case, nanoparticles come from the reaction chamber and are not selected in size (see Sec. 3.1.1.). The typical patterns showing different apparent colors under UV illumination resulting from the expansion of nc-Si through a 3-mm tube into the circular filter chamber, can be clearly seen. Two elliptic spots are formed on both sides of an imaginary vertical line placed in the middle of the filter. Figure 4.3 shows the PL spectra measured on the four different positions indicated in Fig. 4.2. One can notice that the PL peaks are shifted to longer wavelengths while the laser spot is moved out from the center of the elliptic spots to the periphery. PL measurements performed on the left spot of the filter revealed the same behavior (not shown here). The widths of the PL spectra are more than 80 nm larger than those measured for the deposit of size-selected nc-Si on the quartz substrate. They vary here from 210 to 260 nm. Therefore, one can conclude that, even if the nc-Si sizes seem to be radially distributed around the two elliptic spot centers formed by the
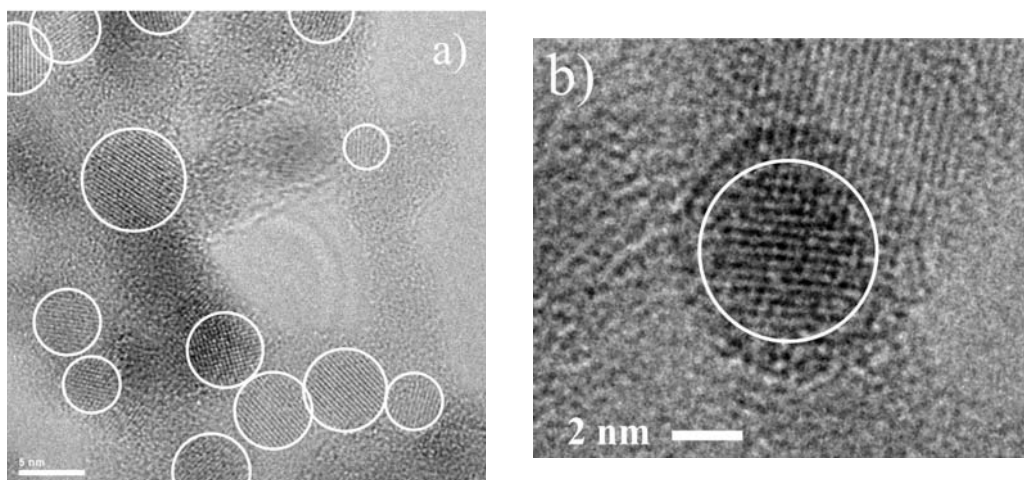
Fig. 4.4. a) TEM image of free nc-Si resulting from the paper filter shown in Fig. 4.1. The silicon cores encircled in white are easily recognizable since high resolution TEM makes it possible to visualize the lattice fringes of the silicon crystalline structure. b) TEM image showing a single crystalline nc-Si surrounded by an amorphous oxide structure.
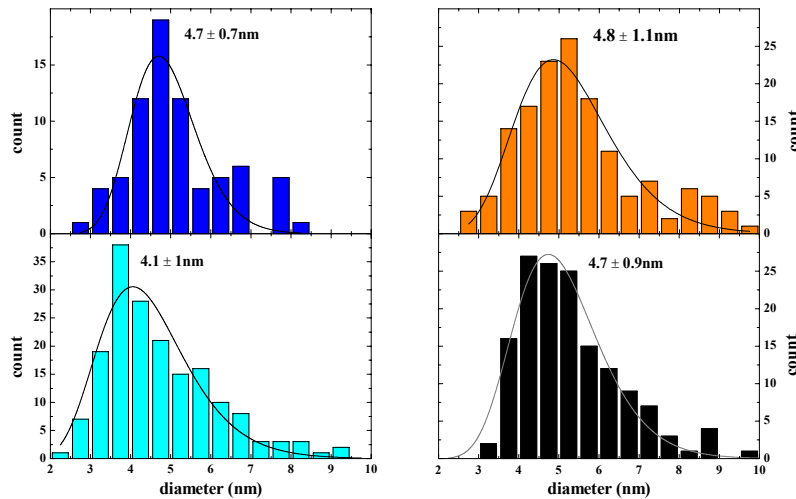
Fig. 4.5. Resulting size distributions of nc-Si corresponding to the four positions 1 (*blue*), 0 (*orange*) 2 (*light blue*), and 3 (*black*) depicted on the paper filter shown in Fig. 4.2. Diameters and standard deviation of each size distribution were evaluated by a log-normal fit (*continuous lines*). The total amount of measured silicon nanoparticles were about 75, 175, 150, and 150 particles for the positions 0, 1, 2, and 3, respectively.

nanoparticles expansion, the size distributions observed in the 0.5-mm laser spot are appreciably broader than those obtained by deposition in the cluster beam.

4.1.2. Structural investigation by TEM

In order to investigate their structural properties, nc-Si were scratched from each four positions on the right side and subsequently dissolved in a chloroform solution to be finally spread out on a copper grid dedicated to TEM measurements. Figure 4.4.a shows a typical TEM image of such prepared samples, where the silicon crystalline cores are easily recognized because of the lattice fringes of the silicon crystalline structure. The spacing of the lattice fringes corresponds to bulk crystalline silicon (0.31 nm). The nanoparticle structure consists of a crystalline core completely covered by an amorphous silicon oxide shell as may be recognized in Fig. 4.4.b. Nevertheless, only a few images – 8 actually – have revealed this core-shell structure since the nanoparticles are generally agglomerated in a large ensemble of nanoclusters as may be seen in Fig. 4.4.a. The average oxide thickness amounts to 16 % of the

Fig. 4.6. Maximum positions of PL spectra in terms of energy of free nc-Si produced by laser pyrolysis of silane of the four positions 1 (*blue*), 0 (*orange*), 2 (*light blue*), and 3 (*black*) indicated in Fig. 4.2 as a function of the diameter of the crystalline core. The nanoparticles sizes were determined by TEM. The black curve arises from a fit of theoretical calculations of H-passivated free nc-Si from Delerue *et al.*[5]

total nanoparticle diameter, which is in good agreement with the values reported by Ledoux *et al.*[72] who found that oxides shells varied between 8 and 16 %.

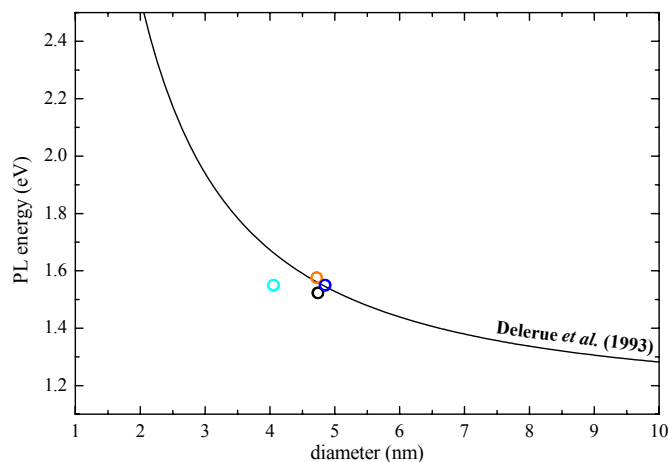Figure 4.5 shows the size distributions of nc-Si corresponding to the four positions indicated on the filter. One can notice that the standard deviations of the four size distributions are rather large. This can be partly explained by the fact that nc-Si were collected from a larger area than the 0.5 mm-diameter spot excited by the laser.

4.1.3. Size dependence of the PL of nc-Si embedded in SiO₂

In Fig. 4.6, the maximum position of the PL curves measured at these four positions of the investigated filter are plotted as a function of the evaluated particle core diameters. As was already observed in the previous work of Ledoux *et al.*,[72] where the nanoparticles' sizes were evaluated by TOFMS, there is a good agreement between the experimental results and the theoretical study of H-passivated free nc-Si of Delerue *et al.*[5]

4.2. nc-Si embedded in SiO₂ produced by ion implantation

The first part of this section reports on the formation of luminescent nc-Si by ion implantation and subsequent annealing at high temperature. The different synthesis stages are investigated by Rutherford backscattering spectroscopy, optical transmission spectroscopy, Raman spectroscopy, and PL measurements. The focus of the second half of this section is more concentrated on the luminescence properties of nc-Si. Temporal behavior, temperature dependence, and excitation intensity dependence will be discussed.

4.2.1. Formation of luminescent nc-Si embedded in SiO₂

4.2.1.1. Implantation profile

Fig. 4.7 shows the depth distribution of Si atoms implanted with an energy of 100 keV and two ion fluences of 1×10^{17} and 2×10^{17} ions/cm² into fused silica windows. The experimental results were obtained from the energy spectrum of backscattered helium ions, and the simulation was performed using the Monte Carlo code SRIM-2003.[133] Since it is experimentally difficult to distinguish by RBS the excess Si from the SiO₂ matrix, especially for low ion fluences, only a few points of concentration of excess Si as a function of the depth could

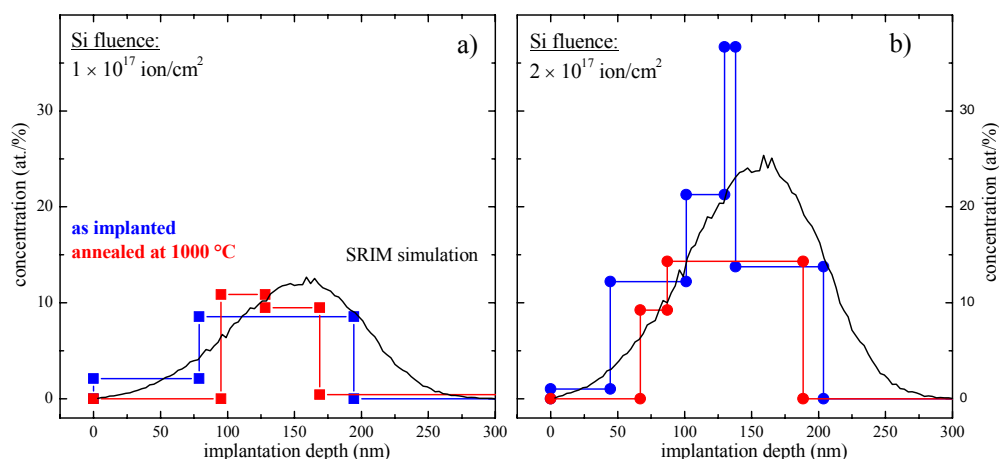Fig. 4.7. Relative concentration of excess Si versus depth for fused silica windows implanted with 100-keV Si⁺ ions with a) 1×10^{17} ions/cm² and b) 2×10^{17} ions/cm² (*blue*) and subsequently annealed at 1000 °C (*red*) in flowing N₂ during one hour as determined by RBS. In comparison, the relative concentration of excess of Si as determined by SRIM simulation is shown (*black*).

be evaluated from the RBS spectrum. In comparison, Wendler *et al.,*[141] who did analogous RBS measurements on Si-implanted quartz, only with a higher Si fluence (4×10^{17} ions/cm^2), could obtain an implantation profile with the same shape as simulated that contained more points. Moreover, it is also seen in Fig. 4.7 that the experimental profile is shifted to the surface because of sputtering effects during implantation. The shift (~25 nm) is in accordance with the Si sputtering value given by SRIM simulation. After annealing (*red*), the profile of Si excess becomes narrower in comparison with the as-implanted profile (*blue*). This can be understood as resulting from an Ostwald ripening process. Small precipitates in the wings of the distribution dissociate and, and on the other hand, large particles in the maximum of the profile grow further. Such effect has been clearly observed by means of TEM which shows that the sizes of the nc-Si formed in the middle of the implanted layer (100 keV) are larger than those near the surface and the bottom of the layer at high implantation fluence (3×10^{17} ions/cm^2), whereas the nc-Si are homogeneously distributed over the whole implanted layer at low implantation fluence ($\leq 8 \times 10^{16}$ ions/cm^2).[142]

4.2.1.2. Optical transmission spectroscopy

Figure 4.8.a shows a comparison of absorption spectra of as-implanted and annealed fused silica windows into which Si$^+$ ions were implanted with ion fluences ranging from 0.5×10^{17} to 2×10^{17} ions/cm^2. One can clearly observe from the comparison with the unimplanted sample depicted in grey that the broad absorption band in the ultraviolet-visible range (200 - 600 nm) of irradiated samples is due to the presence of excess Si in the SiO$_2$ matrix. Moreover, absorption is apparently proportional to the number of Si atoms in the as-implanted and annealed samples. One can notice that the slope of absorption becomes steeper after one hour of thermal treatment. This behavior, which has previously been observed by several researchers,[15, 124] is directly related to the crystalline nature of the Si precipitates. In the as-implanted samples, a broad band is an indication of amorphous states and the presence of defects, whereas the rising edge observed in annealed samples is due to the onset of absorption in the quantum-confined state of the nc-Si. Furthermore, Pellegrino *et al.,*[15] who studied the evolution of absorption of Si-implanted quartz as a function of annealing time, demonstrated in their transmission measurements that nanocrystals are completely formed
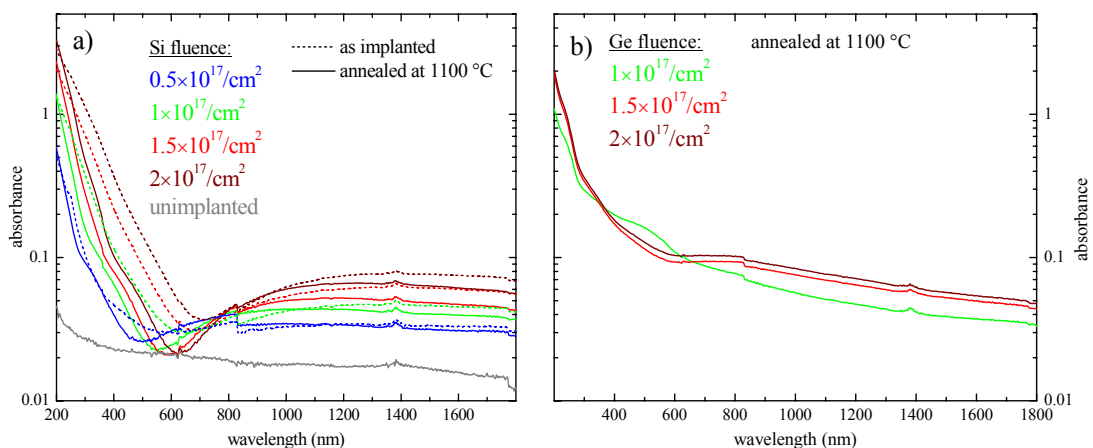

Fig. 4.8. Absorbance plotted in logarithmic scale as a function of wavelength for fused silica samples implanted with a) 100-keV Si$^+$ ions and b) 208-keV Ge$^+$ ions. The discontinuity in the transmission measurement at 830 nm is due to a detector change.

after the first minutes of annealing time at 1100 °C.

It is also seen in Fig. 4.8.a that the absorption edges of the annealed samples are parallel for each Si[+] ion fluence, which is in accordance with the measurements reported by Garrido et al.,[10] who found that in such samples the absorption band gaps are independent of the details of the nc-Si distribution.

Elliman et al.[143] have demonstrated that the broad absorption band starting beyond 600 nm results from interference effects and therefore is an artifact of the transmission measurement and can lead to misinterpretation. Pavesi et al.,[127] who claimed to have identified a new absorption band near 800 nm, had previously attributed this band to the Si=O defect. Since these interference effects significantly change absorption spectra, one can thus cast doubt on energy band gap values obtained by this method. PL excitation measurement is a more suitable method to evaluate the band gap of nc-Si.[10] However, absorption in highly scattered samples such as fused silica windows containing nanoparticles can be appropriately measured by photothermal deflection spectroscopy.[143]

In comparison, Fig. 4.8.b shows absorption spectra of quartz samples implanted with germanium ions with ion fluences ranging from 1×10^{17} to 2×10^{17} ions/cm^2 and subsequently annealed at 1100 °C. Again, the steeper absorption band in the near UV is attributed to the presence of Ge nanocrystals. However, one can notice that the absorption slopes are much softer than for nc-Si in Fig. 4.8.a. This is qualitatively consistent with the fact that the band gap of Ge nanocrystals is significantly smaller than that of nc-Si for an identical nanoparticle size.[144]

4.2.1.3. Raman spectroscopy

Figure 4.9 shows the Raman spectrum of an Si-implanted fused silica window subsequently annealed at high temperature. A spectrum of an un-implanted sample is also shown for comparison. The spectrum is characterized by a resonance at ~520 cm^{-1} caused by the Raman transition of crystalline silicon which indicates the presence of nc-Si. Similar observations have been previously reported on nc-Si embedded in SiO$_2$ produced either by ion implantation[44] or by low energy implantation[145] and also on Si/SiO$_2$ superlattices containing nc-Si.[146, 147] In the same way, Raman measurements confirmed the crystallinity of free silicon nanoparticles produced by laser pyrolysis of silane.[94, 148] A closer look reveals a redshift of the optical phonon peak (517.9 cm^{-1}) with respect to bulk silicon (reference sample) which is explained by confinement effect due to the reduced penetration depth of the excitation radiation. The size of nc-Si can be estimated using the comparison of experimental and theoretical results for Raman line positions versus nanoparticle sizes reported by Paillard et al.[148] They demonstrated a size dependence of the shift $\Delta\omega$ of the Si phonon frequency with respect to that of bulk crystalline silicon following the relation $\Delta\omega = -A \, (a/D)^\gamma$, where $A = 52.3$ cm^{-1}, $\gamma = 1.586$, $a = 0.543$ nm is the silicon lattice parameter, and D is the mean diameter of the nanocrystals. The amorphous SiO$_2$ background Raman signal was subtracted from the measured spectrum and fitted with a Lorentzian function in order to determine its maximum position. We found an average size of 3.9 nm. In Fig. 4.14, we have plotted the PL peak position
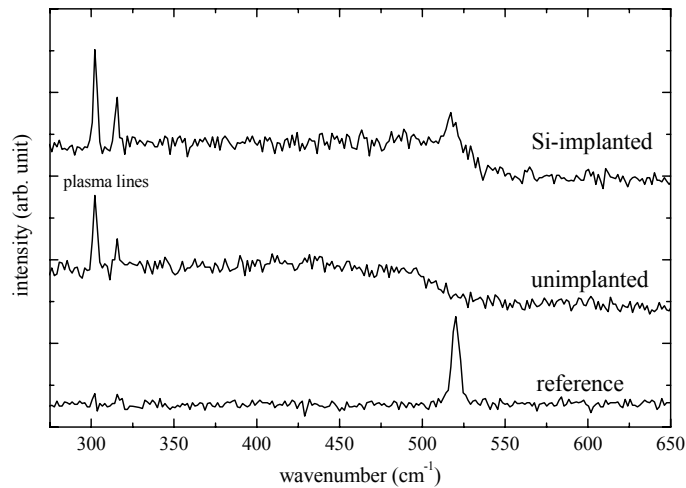
Fig. 4.9. Raman spectra of a) a fused silica window implanted with 100-keV Si[+] ions with an ion fluence of 1×10^{17} ions/cm^2 and subsequently annealed at high temperature, and b) of an unimplanted sample. c) Reference Raman spectrum of a bulk single silicon crystal. The two peaks at 302.4 and 316.1 cm^{-1} are Ar^{+}-laser plasma lines arising from the excitation source.

of this sample (1.46 eV) as a function of the so-evaluated size. This result is in accordance with other studies dedicated to the synthesis of nc-Si by ion implantation (see Sec. 4.2.1.7.). However, the Raman spectrum of nc-Si embedded in SiO$_2$ can be affected by compressive stress caused by the host matrix, which induces a blue shift of the crystalline silicon Raman peak.[149, 150] Moreover, since the isotopic composition of nc-Si formed by implantation of ^{28}Si ions is different from natural bulk silicon, an additional blue shift could affect the Raman spectrum, as reported in the case of Ge nanocrystals.[150] The combined effects of compressive stress and isotopic composition would ergo lead to an underestimation of the size of the nanoparticles.

4.2.1.4. Structural investigation by TEM

TEM confirms the presence of small nc-Si inside an amorphous oxide matrix. Figure 4.10.a shows a typical TEM image of a sample prepared by the cross section method (see Sec. 3.2.4.), where the lattice fringes of the crystalline silicon nanoparticles are clearly seen. Apparently it is more difficult to distinguish nc-Si from the amorphous oxide matrix than for free
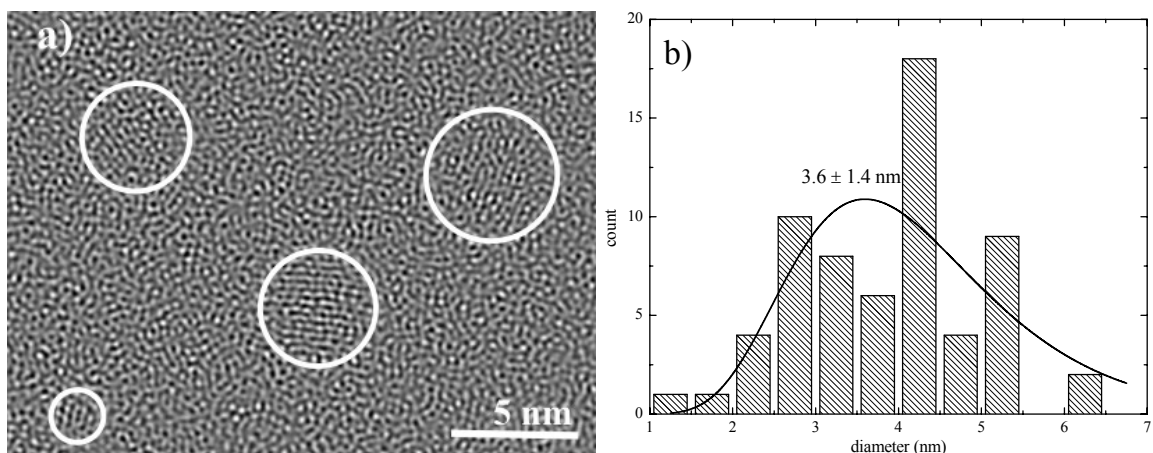
Fig. 4.10. a) Typical cross section TEM image of a fused silica window implanted with 100-keV Si[+] ions with a fluence of 1×10^{17} ions/cm^2 and subsequently annealed at 1100 °C in N$_2$ atmosphere during one hour. Circles indicate typical lattice images of nanocrystallites. b) Histogram of the size distribution resulting from the evaluation of 63 nc-Si diameters. Diameter and standard deviation of the distribution were evaluated by fitting the data with a log-normal function (*continuous line*).

oxidized nc-Si surrounded by a thin oxide layer which was deposited on a substrate (see Fig. 4.4). In Fig. 4.14, the PL peak position of this sample (1.44 eV) is plotted as a function of the mean diameter of the nanoparticles that was estimated by a log-normal fit of the data. This result is consistent with previous studies dedicated to the synthesis of nc-Si by ion implantation and subsequent annealing (see Sec. 4.2.1.7.).

4.2.1.5. Effect of annealing on PL of nc-Si embedded in SiO$_2$

Figure 4.11 shows PL spectra from fused silica samples after various stages of the synthesis of nc-Si. The as-implanted sample (*dotted blue line*) exhibits an asymmetric PL peak at around 650 nm, which arises from defects created in the host matrix during implantation. In comparison, the PL spectrum of a He irradiated sample is shown. It peaks at the same position and has the same shape. This well-known luminescence is attributed to nonbridging oxygen hole centers $\equiv$ Si-O$^{\bullet}$ in the SiO$_2$ matrix; ($\equiv$) stands for bonds with three oxygen atoms and ($^{\bullet}$) indicates an unpaired electron.[82, 83] Although the He fluence is 100 times lower than the Si fluence, its PL peak intensity is more than two times higher. This can be easily explained by the fact that He irradiation induces mainly binding defects in the amorphous SiO$_2$ matrix, whereas Si irradiation creates structural damages by displacement of atoms. The number of vacancies induced by Si implantation, which were evaluated by SRIM simulation, are five orders of magnitude higher than those caused by He irradiation (see Fig. 5.9). Following annealing at high temperature ($\geq$ 900 °C), this defect luminescence totally disappears and the PL emission is dominated by nanocrystal-based Vis-NIR emission. The peak emission wavelengths ranging from 800 to 1000 nm are consistent with the emission from quantum-confined nc-Si with mean diameters ranging from 3 to 6 nm (see Sec. 2.2.4.). It has already been demonstrated that the intensity of the defect luminescence decreases significantly with increasing annealing temperature and fully disappears after thermal annealing at 800 °C.[151, 152] More-
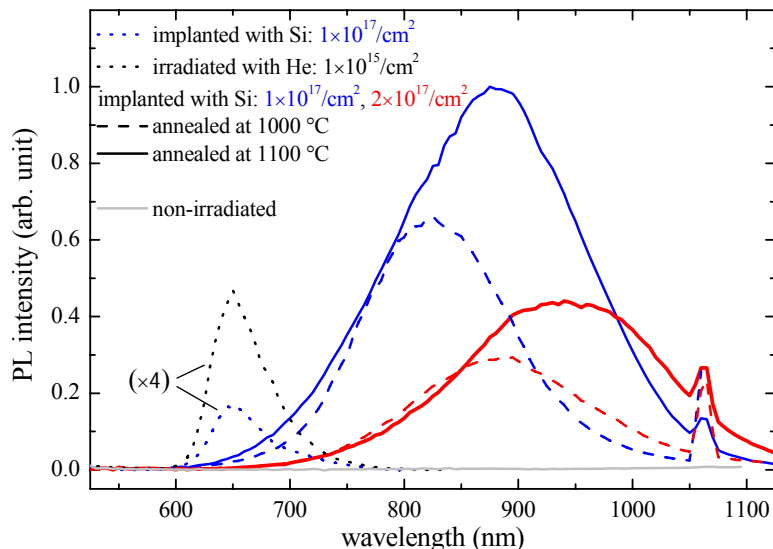
Fig. 4.11. PL spectra of as-implanted (*dotted lines*) fused silica windows implanted with 100-keV Si$^+$ ions with two different ion fluences of 1×10^{17} (*blue*) and 2×10^{17} ions/cm^2 (*red*), and of samples subsequently annealed at 1000 °C (*dashed lines*) or 1100 °C (*continuous lines*) in N$_2$ during one hour. For comparison, the PL spectrum of a sample irradiated with 1.4-MeV He$^+$ ions with an ion fluence of 1×10^{15} ions/cm^2 (*dotted black line*) is shown. The as-implanted spectra are multiplied by a factor of 4 for clarity. The 1064 nm-PL peak originates from the remaining light of the fundamental of the Nd:YAG laser.

over, the intensity ratio between defects and nc-Si luminescence is in good agreement with previous experiments.[152, 153]

The effect of annealing temperature on the PL of nc-Si is seen in Fig. 4.11. The PL increases and shifts to longer wavelengths with increasing annealing temperature from 1000 to 1100 °C. This is consistent with previous studies on the PL dependence on annealing temperature of samples prepared by ion implantation of Li et al.[152] They observed that the nc-Si PL increases rapidly with increasing annealing temperature and reaches a maximum at the thermal annealing temperature of 1100 °C. Again, they observed a significant red shift while the annealing temperature increases. The enhancement of the PL intensity with increasing annealing temperature can be understood in terms of better passivation, while the size distribution of nc-Si shifts to larger nanoparticles so that the position of the PL peak shifts to longer wavelengths. Above 1100 °C, the nc-Si PL intensity decreases seriously[137, 152] because of the significant raise of the nanoparticle size caused by Ostwald ripening.

Figure 4.12.a shows the evolution of the silicon nanoparticle size as a function of the annealing time according to Garrido et al.[10] The mean diameter increases very quickly in the first minute and then increases very slowly when the annealing time changes from 1 min to 16 hours. This is consistent with the absorption spectra measured by Pellegrino et al.,[15] who demonstrated that silicon precipitation in implanted SiO_2 samples takes place in the first minutes of annealing at 1100 °C in N_2 atmosphere. However, the evolution of the PL with the annealing duration is also conditioned by the surface passivation of the nc-Si. As illustrated in Fig. 4.12.b, the PL intensity of the nc-Si increases and eventually reaches saturation with increasing annealing duration, while it correlates inversely after 30 minutes with the amount of Si dangling bonds at the nanocrystal/oxide interface (*Pb* centers, see Sec. 2.2.2.3.), as measured by electron spin resonance.

Annealing environment plays an important role on the luminescence of nc-Si in silica. This has been studied in detail by Wilkinson and Elliman,[154] who compared the behaviour of the PL versus three commonly used annealing environments: Ar, N_2, and 5% H_2 in N_2, also called forming gas (FG). PL spectra from samples annealed in Ar exhibit a significant red shift compared to PL spectra from samples annealed in the other two environments. They are also considerably weaker in peak and integrated intensity. The differences in PL shape and intensity resulting from Ar environment have been partly attributed to differences in nanocrystal size distribution. Furthermore, Raman measurements suggest that N_2 could be incorporated within the oxide. Annealing in Ar is a simple process of thermal relaxation, while annealing in N_2 is a process of thermal relaxation that is affected by the exchange of nitrogen with the oxide matrix, which contributes to the synthesis of smaller nanocrystals and improves the degree of surface passivation.

PL spectra of samples annealed in 5% H_2 in N_2[154, 155, 156] or in 5% H_2 in Ar atmosphere[153] exhibit a significant increase of the PL intensity compared to PL spectra from samples annealed in environments without H_2. The enhancing effect of FG on the PL is well-known and is generally exploited in a second annealing at low temperature (~600 °C) that
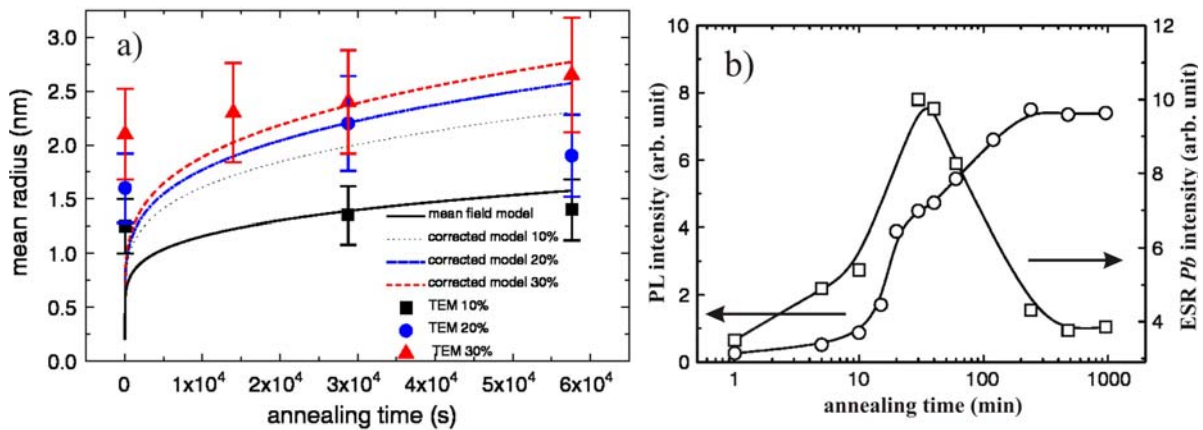
Fig. 4.12. a) Values determined by HRTEM (*symbols*) of the average size of nc-Si as a function of annealing time and simulated curves for Si excess concentrations varying from 10 to 30% according to Garrido *et al.*[10]. b) Correlation of PL intensity evolution versus annealing time with the evolution of the amount of *Pb* centers measured by electron spin resonance for Si excess concentration of 10% according to Pellegrino *et al.*[15] Thermal treatments were performed at 1100 °C in N_2 atmosphere.

follows a first annealing performed in an N_2 or Ar atmosphere at higher temperature (~1100 °C). Ion implantation of hydrogen or deuterium with subsequent thermal treatment results in a similar effect.[157] Withrow *et al.*[153] demonstrated that hydrogen is selectively trapped in the region of the nc-Si and enhances the PL intensity yield, by passivating non-radiative defects at the nanocrystal/oxide interface (*Pb* centers). Furthermore, PL spectra are also significantly shifted to longer wavelengths. Cheylan and Elliman[155] showed that the enhancement increases monotonically with the increasing wavelength. Since a longer emission wavelength is characteristic of larger nanocrystals, according to the quantum confinement model, this implies that a greater fraction of these nc-Si contains non-radiative defects prior to passivation. This is consistent with the fact that the number of defects might reasonably be more present in larger nanoparticles (see Sec. 2.2.2.2.). Significant increase in the PL intensity has been found in samples coated with a thin aluminum layer compared to standard FG-annealing.[156] This implies that at least two different recombination centers (*Pb*) are present at the nanocrystal/SiO_2 interface, one that reacts with molecular hydrogen and one that only reacts with atomic hydrogen generated via the metal layer.

Annealing SiO_2 films containing nc-Si in flowing O_2 at 1000 °C results in a PL intensity decrease and a continuous blue shift of the spectra with increasing oxidation time.[158, 159] This blue shift is attributed to a quantum size effect in which a reduction of the average nanocrystal size by oxidation leads to the emission of shorter wavelengths. RBS measurements show that the oxidation of the nc-Si starts close to the sample surface, followed by oxidation of nc-Si located at a greater depth.[159, 141]

In conclusion, one can say that the choice of annealing temperature, duration, and environment has significant influence on the luminescence of nc-Si. An optimum choice of annealing parameters, however, does not guarantee to passivate completely the nc-Si, and, thus to achieve, a good PL yield. The cooling period of the annealing cycle is also essential to avoid the formation of residual stress, which is known to quench the luminescence (see Sec. 3.1.2. and 2.2.2.6.).

The PL emission of our fused silica windows containing nc-Si produced by ion implantation and subsequent annealing is visible with the naked eye under UV light illumination (~100 µJ at 266 nm) and is comparable with the PL intensity of free nc-Si produced by laser pyrolysis of silane. Although a certain degree of tunability of the PL emission is shown for nc-Si embedded in SiO$_2$, this is, however, far from that observed for free nc-Si produced by laser pyrolysis of silane.

4.2.1.6. Silicon fluence dependence of PL of nc-Si embedded in SiO$_2$

The Si$^+$ ion fluence dependence of the PL spectra of nc-Si formed by Si implantation in fused silica windows and subsequent annealing is shown in Fig. 4.13.a. The windows were implanted with Si$^+$ ions with different ion fluences ranging from 0.5 to 2×10^{17} ions/cm^2, corresponding to excess Si peak concentrations of 6 to 26%, respectively. It is clearly seen that the PL spectra shift to longer wavelengths and increase in width (see Fig. 4.13.b) as the silicon excess concentration increases, which is qualitatively consistent with the quantum confinement model, reflecting changes in the size distribution of optically active nc-Si. Similar results have been reported for different implantation and annealing conditions.[10, 155, 158]

Figure 4.13.a also shows an increase of the PL intensity when the maximum position moves from 780 to 850 nm and a subsequent decrease for the spectra peaking above 850 nm. The highest efficiency is obtained for a Si excess close to 13% which corresponds to an average size of 3.8 nm (see Fig. 2.22). This is consistent with the previous results of Shimizu-Iwayama et al. (8% of Si excess),[158] Garrido et al. (10% of Si excess),[10] Cheylan and Elliman (10% of Si excess),[155] and Sa'ar et al. (16% of Si excess).[12] This is also in accordance with the PL quantum efficiency measured by Walters et al.[160] Indeed, in their study, the maximum quantum yield of optically active embedded nc-Si (60%) was found for an emission wavelength of 800 nm which corresponds to an average size of 3 nm. In comparison, the maximum PL yield (30%) of free nc-Si covered by a SiO$_2$ layer produced by laser pyrolysis of silane measured by Ledoux et al.[72] was found for an average size of 3.8 nm which corresponds to an emission wavelength of 840 nm. In our samples, the behavior of the PL intensity with the Si$^+$ ion fluence can be explained by the concerted action of three effects: the increase of the nc-Si

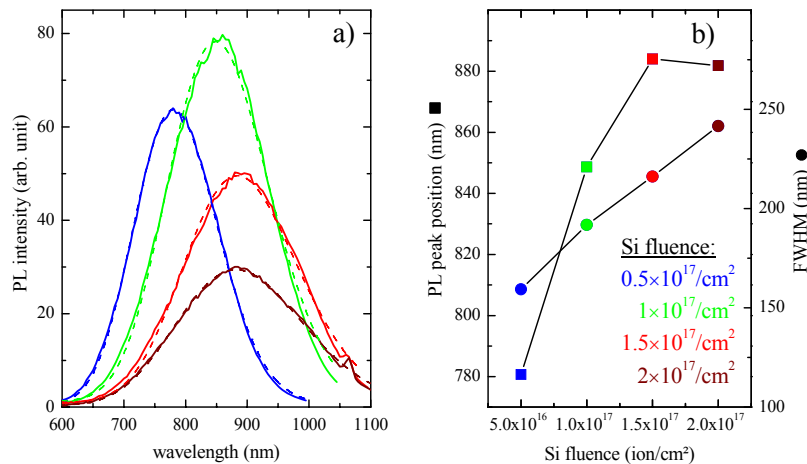
Fig. 4.13. a) Photoluminescence of fused silica windows implanted with 100-keV Si$^+$ ions with four different ion fluences and subsequently annealed at 1100 °C in N$_2$ during one hour (*continuous lines*). PL spectra were fitted with log-normal functions (*dashed lines*) in order to evaluate their peak positions (*squares*) and width (*circles*) which are plotted versus Si ion fluence in b).

concentration and the decreasing PL efficiency as a result of reduced quantum confinement and/or as a result of increased probability of encountering a defect inside the nc-Si. Defects are non-radiative recombination centers. Indeed, the PL quantum yield η_{PL} is a function of the radiative, R_{rad}, and non-radiative rates, $R_{non-rad}$, and can be written as $\eta_{PL} = R_{rad} / (R_{rad} + R_{non-rad})$.[74] Radiative rates increase as quantum size decreases, according to the quantum confinement model.

4.2.1.7. Size dependence of the PL of nc-Si embedded in SiO$_2$

Figure 4.14 shows the size dependence of the PL of nc-Si synthesized by ion implantation and subsequent annealing. We have plotted the PL peak position of one of our samples (*full circle*) as a function of the mean diameter of the nc-Si that was determined by means of TEM (see Sec. 4.2.1.4.). For comparison, we plotted the PL peak position of another sample (*open circle*), the size of which was evaluated by Raman spectroscopy (see Sec. 4.2.1.3.). As one can see, our results are in accordance with previous studies where the nc-Si sizes were all determined by mean of TEM (see Appendix A). Apparently, the experimental size dependence of the PL of embedded nc-Si does not follow the theoretical calculations of Delerue *et al.*,[5] that were based on the quantum confinement model. However, these calculations were done for H-passivated free nc-Si, and one can reasonably suspect an embedding effect. This is supported by the fact that other results concerning nc-Si/SiO$_2$ systems that were synthesized by various other techniques follow the gray curve as well (see Sec. 2.2.4.).

One can see in Fig. 4.14, and even in a much more evident way in Fig. 2.22, that the PL peaks of embedded nc-Si range from the band-gap of bulk silicon at room temperature (1.12 eV) to an upper limit at around 1.75 eV (*dashed line*), which has been observed by other authors.[10, 158] It seems that the PL does not depend on the size for smaller nanocrystals ($\leq$ 2.5 nm). In this regime, the recombination of excitons would originate from interface states in the band gap of nc-Si (See Sec 2.2.2.3.). Therefore, one can reasonably question the origin of the PL observed by Guha[124] at 1.9 eV, all the better that this emission energy corre-
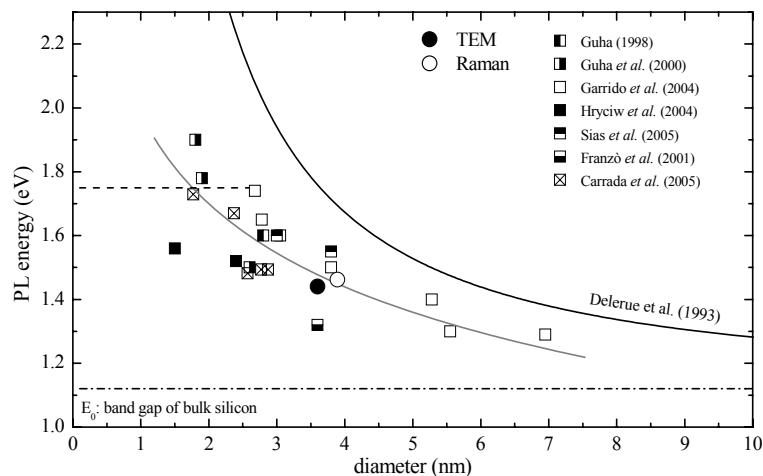
Fig. 4.14. Positions of PL peaks in terms of energy of nc-Si produced by ion implantation as a function of the diameter of the crystalline core. The nanoparticles' sizes of two of our samples (*circles*) were determined either by TEM or evaluated by Raman spectroscopy. Some values (*squares*) extracted from the literature are also plotted for comparison.[124, 107, 10, 108, 109, 110, 111] The black curves arise from a fit of theoretical calculations of H-passivated nc-Si from Delerue *et al.*,[5] whereas the gray curve is shown to guide the eye.

sponds to the defect luminescence of non bridging oxygen hole centers (see Sec. 2.2.2.4.) frequently observed in irradiated quartz.

4.2.1.8. Synthesis of nc-Si in SiC by ion implantation

Ion implantation followed by thermal treatment is a common technique to produce embedded nanocrystals. Since Kaiser *et al.*[161] demonstrated by TEM the existence of nc-Si in hexagonal silicon carbide after Si implantation and subsequent annealing, we have have carried out similar experiments in order to investigate the PL properties of nc-Si embedded in SiC. Silicon ions were implanted into 4H-SiC (n-type) bulk single crystal wafers supplied by Cree Research Inc. During implantation, the temperature was kept at 700 °C in order to prevent an amorphization of the crystalline matrix.[162] The samples were tilted at an angle of 7° with respect to the ion beam to avoid channeling effects. A first set of samples was implanted with 110-keV Si^+ ions with ion fluences ranging from 0.5 to 2×10^{16} ions/cm^2 and subsequently annealed at 1600 °C during 120 s in N_2 atmosphere, according to the synthesis conditions reported by Kaiser *et al.* A second set of samples was produced by 150-keV Si^+ ion implantation with fluence values ranging from 0.1 to 1×10^{17} ions/cm^2 and subsequent annealing at 1500 °C during one hour in N_2. Although the particle sizes are expected to range from 2 to 7 nm under these synthesis conditions, no PL was observed. This can be explained by the difficulty to passivate nc-Si embedded in a crystalline structure.

4.2.1.9. Conclusion

Formation of silicon nanocrystals in a Si-implanted SiO_2 matrix by high temperature annealing is achieved by diffusion, nucleation, aggregation, crystallization, and growth processes. The implantation of Si^+ ions forms an excess concentration of Si in SiO_2 and, to a lesser extent, Si aggregates. The diffusion of Si is counterbalanced by the nucleation and aggregation of Si dots which grow and crystallize in the first moment of annealing. With such condensation of implanted Si after prolonged annealing, the growth of nanocrystals can be explained by Ostwald ripening, which predicts that larger nc-Si grow being supplied with Si atoms from surrounding Si clusters of smaller size. This effect, combined with the passivation of nc-Si, that is, reduction of the number of silicon dangling bonds at the surface, leads to a significant increase of the luminescence. Ion implantation is a successful technique to produce a homogeneous and high-purity thin suboxide $SiO_{x<2}$ layer in host SiO_2 matrices which leads to the production of homogenously distributed nc-Si.

4.2.2. Other photoluminescence properties of nc-Si embedded in SiO$_2$

4.2.2.1. Time-resolved photoluminescence spectroscopy

The multi-exponential behavior of the decay curves of an ensemble of nc-Si embedded in SiO_2 has previously been observed by other researchers.[10, 137] Similar behaviors have been also reported on free nc-Si covered by a thin oxide layer,[123, 163] and on porous silicon.[164, 137] The decay curves are usually fitted by a Kohlrausch function $I(t) = I_0 \exp[-(t/\tau)^\beta]$ where τ is the lifetime and β the dispersion factor. Analogous properties have been observed for the luminescence of CdSe quantum dots. Schlegel *et al.*[136] and Fisher *et al.*[135] showed that the multi-exponential feature is intrinsic to one single quantum dot. They noticed that the decay life-
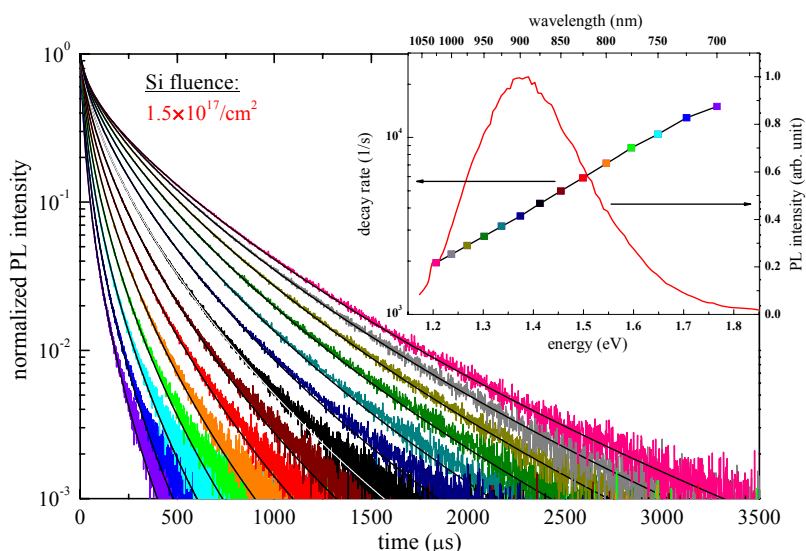
Fig. 4.15. PL decay curves of nc-Si embedded in SiO$_2$ recorded from 675 nm (*left curve*) to 1 μm (*right curve*) with a step of 25 nm. The inset shows the PL spectrum of the respective sample as well as the decay rates as a function of emission energy.

times correlated strongly with the luminescence intensity fluctuations where a high PL yield is associated with a long PL lifetime. In particular, at the highest PL intensity, the decay curves were found to approach a single-exponential behavior. The multi-exponential behavior of the decay curves of luminescent nanoparticles is still not completely understood. Experiments demonstrated that single nc-Si reveal blinking under UV-excitation.[134] This PL emission intermittency, which is also observed in single CdSe nanocrystals, is explained by the existence of a dark state, which is commonly assumed to be a charged state, where the electron of the excited electron-hole pair is trapped in the surroundings of the nanocrystal. The hole that remains in the crystalline core can efficiently quench further optical recombinations by an Auger process until the particle is neutralized by the return of the electron. Therefore, luminescence decays are believed to reflect the macroscopic dispersion of traps of an ensemble of nc-Si that emit light.

In the main frame of Fig. 4.15, we have plotted the decay curves of the nc-Si PL as measured on a sample produced with an ion fluence of 1.5×10^{17} ions/cm^2. From left to right, the emission wavelength varies from 700 to 1025 nm in steps of 25 nm, *i.e.*, the lifetime increases as the emission wavelength becomes longer. The decay rates were evaluated by fitting log-normal decay rate distributions to the measured data using the maximum entropy method of data analysis.[140] Log-normal rate distributions have also been employed to fit the decay curves of CdSe nanocrystals, but with another method.[139] However, it must be underlined that there is by no means a unique solution and that the decay curves can be fitted by different distributions of rates.

Figure 4.16 shows the decay rates of fused silica windows implanted with three different Si fluences plotted as a function of emission energy. The corresponding PL spectra are plotted in Fig. 4.13. It is seen that the PL decay rates increase exponentially with the emission energy. An exponential increase following an exp(-*E/E**) law, where *E* is the photon energy and the parameter *E** varies between 0.2 and 0.4 eV, has previously been observed by several

Fig. 4.16. Decay rates versus emission energy of nc-Si embedded in SiO_2 produced by Si^+ ion implantation with three different Si fluences ranging from 0.5 to 1.5×10^{17} ions/cm^2. The curves were fitted with an exponential function $f = \exp(-E/E^*)$ in order to evaluate the parameters E^*.
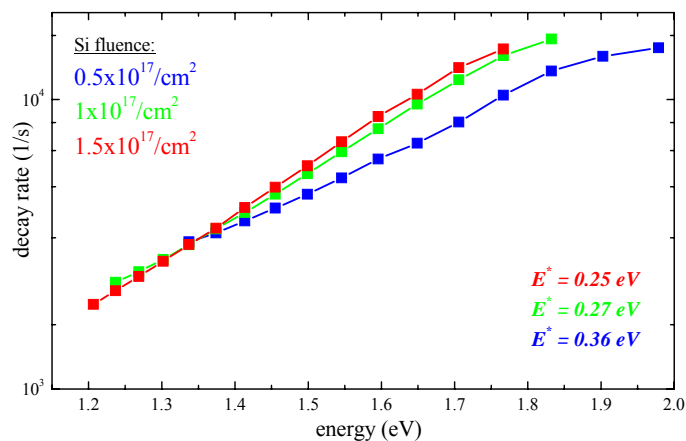
authors.[137, 123, 163, 10, 140] This functional form has always been observed for quantum-confined nanostructures but its physical background still remains unexplained. We found that E^* varies from 0.25 to 0.36 eV, which is consistent with the 0.25, 0.28, and 0.31 eV values found by Huisken *et al.*,[163] Linnros *et al.*,[137] and Delerue *et al.*,[140] respectively. Furthermore, as previously observed by other authors,[137, 165] it is seen that decay rates increase when the ion fluence, *i.e.* the Si excess concentration, increases. This reflects the role of the environment on the luminescence of nc-Si. The more the nc-Si are isolated the longer is the luminescence lifetime. However, this behavior seems to be less pronounced for the largest nanoparticles, since lower emission energy is characteristic of larger nanocrystals, according to the quantum confinement model. Indeed, the three curves are not parallel. The shift of the decay rates between each curve gradually decreases with the size of the nanoparticles. Linnros *et al.* suggested that photogenerated excitons may migrate to adjacent nanocrystals and may become trapped for an extended time and before recombining.[137] This model is also supported by the multiexponential behavior of an ensemble of nc-Si where an excited nanocrystal may act as a donor and transfer its energy to a neighboring acceptor. This picture is consistent with our data showing a gradual increase of lifetimes with the concentration of the nanoparticles, when the nanoparticle size increases. This can be associated with a redistribution of the energy within the sample with a transfer from smaller nc-Si having larger gaps to larger nc-Si having smaller gaps.

4.2.2.2. Temperature dependence

Figure 4.17.a shows PL spectra measured at 6.5, 12.5, 25, 50, 100, 200, and 300 K in a vacuum. As the nanoparticles are cooled down, the PL integrated intensity increases and reaches a maximum at 50 K (Fig. 4.17.b). At the same time, the spectra become slightly narrower and shift to the blue (Fig. 4.17.c). This effect has been reported[166, 167, 168, 169, 19, 39, 170, 11] and explained by a model introduced by Calcott *et al.*,[167] initially for porous silicon. In this model, the localized excitonic levels are split by an energy Δ, due to the exchange interaction between the electron and the hole. The lower level corresponds to a triplet state which has a radiative rate R_T. The upper level corresponds to a singlet state with a radiative rate R_S (see
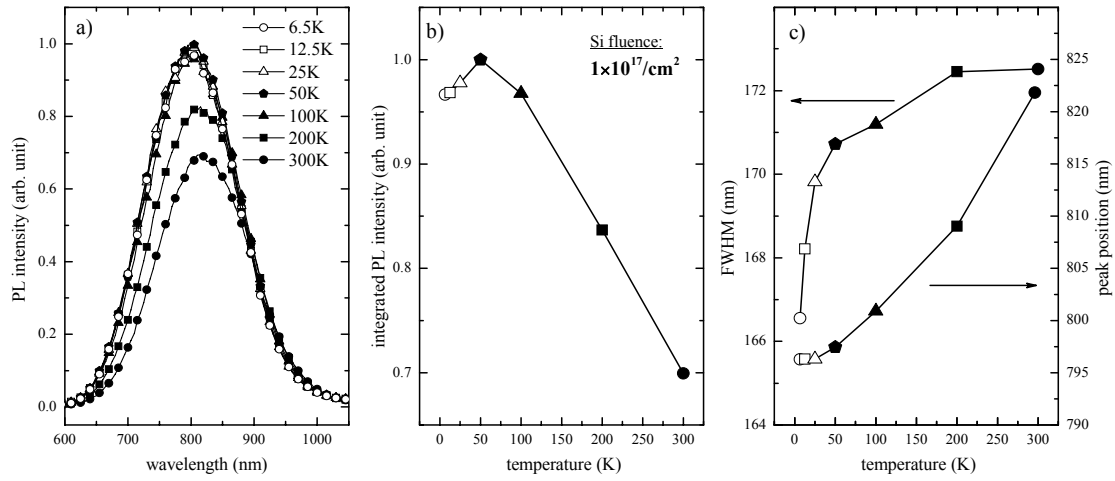
Fig. 4.17. a) Temperature dependence of the PL spectra of nc-Si embedded in SiO$_2$. b) Temperature dependence of the integrated PL intensity, I_{PL}. c) Temperature dependence of the width and the position of the PL peaks.

inset Fig. 4.19.a). The temperature dependence of the radiative decay rate, R_{rad}, can be evaluated on the basis of Boltzmann statistics by assuming thermal equilibrium between the two levels with a weight factor of 3 for the triplet state. Thus the rate becomes

$$R_{rad} = \frac{3\,R_{\text{T}}+R_{\text{S}}\,exp\left(-\frac{\Delta}{k_{\text{B}}T}\right)}{3+exp\left(-\frac{\Delta}{k_{\text{B}}T}\right)} \tag{1}$$

where k_{B} is the Boltzmann constant. At low temperature, only the triplet state is occupied and the radiative decay rate is rather small. When the temperature is raised, the population of the upper level, which is characterized by a faster decay rate, becomes more important. The PL quantum yield η_{PL} is a function of the radiative and non-radiative rates and can be written as $\eta_{PL} = R_{\text{rad}} / (R_{\text{rad}} + R_{\text{non-rad}})$, where $R_{PL} = R_{\text{rad}} + R_{\text{non-rad}}$ is the total PL rate as measured in our time-resolved experiment. The decrease of the PL intensity for temperatures above 75 K can be thus explained by the fact that non-radiative processes between nc-Si and the SiO$_2$ matrix then become more effective.

Figure 4.18.a shows typical multi-exponential decay curves at emission wavelengths of 750, 800, 850, and 900 nm which were measured at temperatures in the range from 6.5 to 300 K. Figure 4.18.b shows the corresponding PL decay rates, R_{PL}, which were evaluated by fitting log-normal decay rate distributions to the measured data using the maximum entropy method (see Sec. 4.2.2.1.). The slow decay curves characteristic for luminescence decay at low temperatures below 25 K were difficult to fit properly using this method, and the decay values given in Fig. 4.18.b might be overestimated. The PL decay rates, for a given emission wavelength, raise by about one order of magnitude as the temperature increases from 6.5 K to room temperature. Furthermore, at temperatures below 25 K, it is seen that the PL decay rates decrease with the increasing emission energy which is in contradiction to the feature observed at high temperature that is reported in the previous section (see Sec. 4.2.2.1.). This behavior has already been observed by Dovrat et al.[169] who suggested that, at low temperature (lower level), the recombination of excitons is dominated by non-radiative processes which depend on the macroscopic properties of the medium and do not depend on the nanoparticles' size.
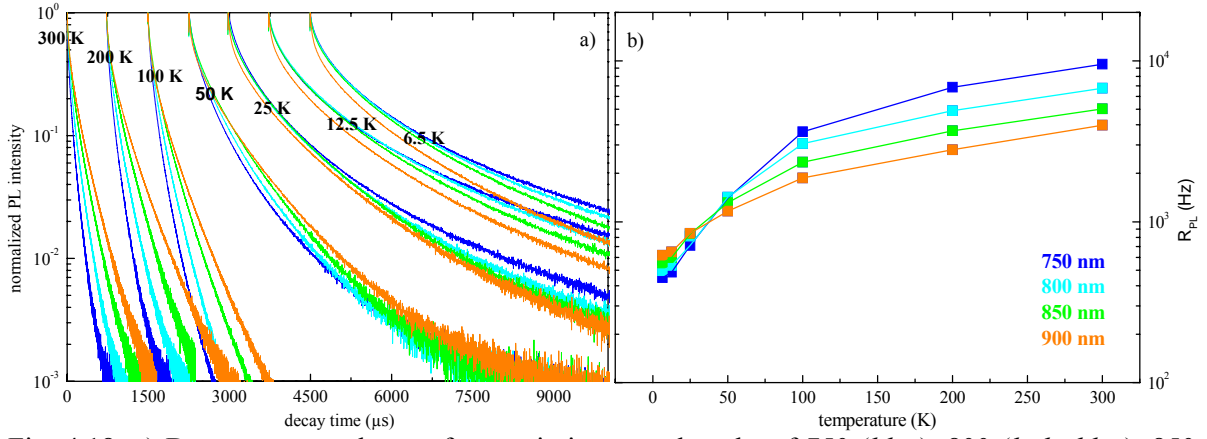
Fig. 4.18. a) Decay curves taken at four emission wavelengths of 750 (*blue*), 800 (*light blue*), 850 (*green*), and 900 nm (*orange*) for different temperatures ranging from 6.5 to 300 K. b) Temperature dependence of the photoluminescence decay rate, R_{PL}, at the four emission wavelengths.

Figure 4.19.a shows the calculated temperature dependence of the radiative rates R_{rad}, for emission wavelengths of 750, 800, 850, and 900 nm, obtained by multiplying I_{PL} (Fig. 4.17.b) with R_{PL} (Fig. 4.18.b) at each temperature. Since these data are derived from I_{PL}, each one is expressed in arbitrary units, and has been multiplied by a different scaling factor to facilitate their comparison. The black curves represent the best fits to the experimental data using Eq. 1. This model seems to reproduce fairly well the temperature dependence observed for R_{rad}. Figure 4.19.b and Figure 4.19.c show the parameters determined by the fitting procedure – the ratio of R_S to R_T and the splitting energy, respectively – which are plotted as a function of the emission energy. It can be seen that the decay rates of the upper level, R_S, are much larger than R_T. However, the range of the ratio of R_S to R_T is about one order of magnitude smaller than previously reported for porous silicon or embedded nc-Si.[11, 166, 167, 168, 169] This large difference can be explained partly by the difficulty to evaluate the PL rates of the long
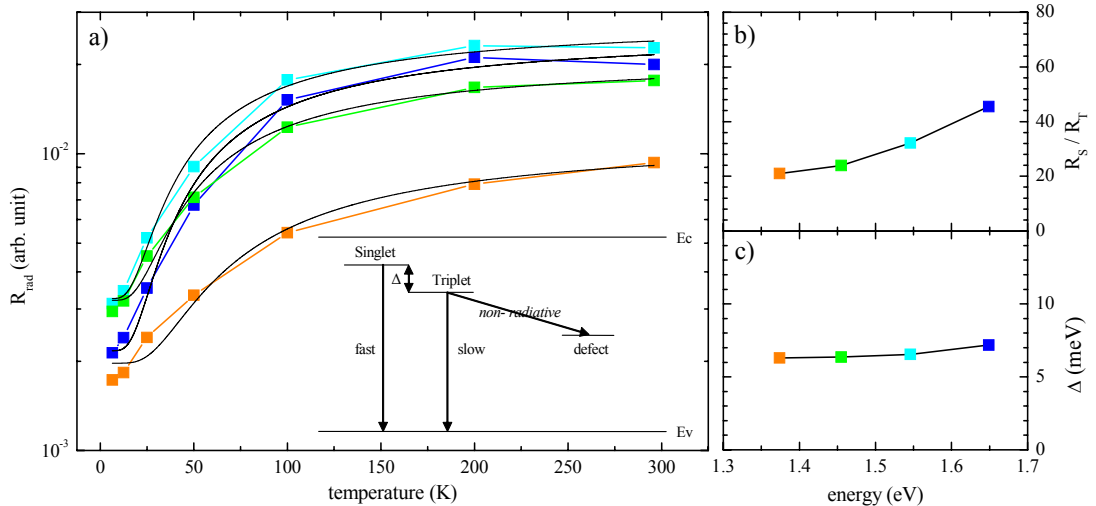
Fig. 4.19. a) Temperature dependence of the radiative rate, R_{rad}, at the emission wavelengths of 750 (*blue*), 800 (*light blue*), 850 (*green*), and 900 nm (*orange*), obtained by multiplying the temperature dependence of I_{PL} data in Fig. 4.12.b with the R_{PL} data in Fig. 4.13.b. The black curves are best fits of R_{rad} using the model of Calcott *et al.*[167] that takes into account the exchange splitting of energy levels of excitons in nc-Si. The inset shows a schematic of the singlet and triplet energy levels split by the electron-hole exchange energy Δ. b) Ratio of the singlet (R_S) and triplet (R_T) radiative decay rates of excitons in nc-Si embedded in SiO_2 as a function of the emission energy. c) Exchange splitting energy as a function of emission energy. The ratio R_S / R_T and values Δ were obtained by fitting Eq. (1) to the temperature dependence of the radiative rate.

decay traces at low temperature with our fitting procedure. On the other hand, Brongersma *et al.*,[166] Timoshenko *et al.*,[19] and Kobitski *et al.*[170] observed a more pronounced decrease of the PL intensity with decreasing temperature below 75 K, compared to our measurements. Kovalev *et al.*[171] have demonstrated that this effect is purely artificial and is caused by the saturation of the PL which is made easier at the long PL lifetime regime below 75 K. Moreover, our measurements are very similar to previous ones reported elsewhere.[11, 168, 169] Furthermore, the splitting energies Δ extracted from the fitting procedure are in line with previous experimentally observed values.[166, 169] The values of Δ are found to increase with the PL emission energy. This dependence of Δ on the nanocrystal size is a strong indication that excitons are confined in the nanocrystalline core, since Δ is determined by the spatial separation between the electron and the hole.

4.2.2.3. Excitation intensity dependence

Figure 4.20.a shows the PL spectra of nc-Si embedded in SiO_2 as the excitation intensity ($\lambda_{exc} = 266$ nm) is increased from to 1.3 $\mu J/cm^2$ to 2 mJ/cm^2. It is interesting to note that the peak position shifts continuously to the blue with increasing excitation intensity. This behavior has been previously reported for nc-Si embedded in SiO_2,[39] porous silicon,[171, 123] and free nc-Si.[123] In order to better understand this behavior, we studied the excitation intensity dependence of the PL intensity at five wavelengths ranging from 700 to 900 nm. The data are reported in Fig. 4.20.b. At all wavelengths, the PL intensity increases with the excitation intensity. For low intensities ranging from 1 to 5 $\mu J/cm^2$, the PL spectra shapes do not show any variation. The occurrence of a non-linear behavior seems to be governed by a threshold. We found 7 and 22 $\mu J/cm^2$ at 700 and 900 nm, respectively, for the values of the threshold, which are in good accordance with these reported by Amans *et al.*[123] Above those latter values, saturation effects are observed. It is clearly seen that the deviation from the linear behavior is stronger and appears at lower excitation intensities for longer wavelengths. This naturally explains the blue shift observed in Fig. 4.20.a. This behavior of the excitation intensity dependence of the PL spectra suggests that the population of smaller excited nc-Si (emitting at shorter wavelengths) is saturated at much higher excitation intensities than larger nanoparticles and can be easily explained by the fact that larger nc-Si have larger absorption cross-sections and longer lifetimes. An interesting feature has been reported by Amans *et al.*[123] They observed that the evolution of the PL spectra is different and depends on whether one increases or decreases the excitation intensity. For a given cycle of increase followed by a decrease in intensity, the positions of the PL maxima roughly formed a hysteresis. In order to explain the mechanism able to transform a radiative nc-Si into a non-radiative one, a significant increase of the density of charges within the nanoparticles created by the formation of many excitons followed by Auger non-radiative recombinations has been advanced. The excitation intensity dependence of the PL decay rate has been studied at low temperature by Vinciguerra *et al.*[39] and Kovalev *et al.*[171] The PL decay rates increase with increasing excitation intensity. Moreover, at high excitation intensities, the multi-exponential feature of the decay curves is more pronounced. In this regime, several excitations can be simultaneously present
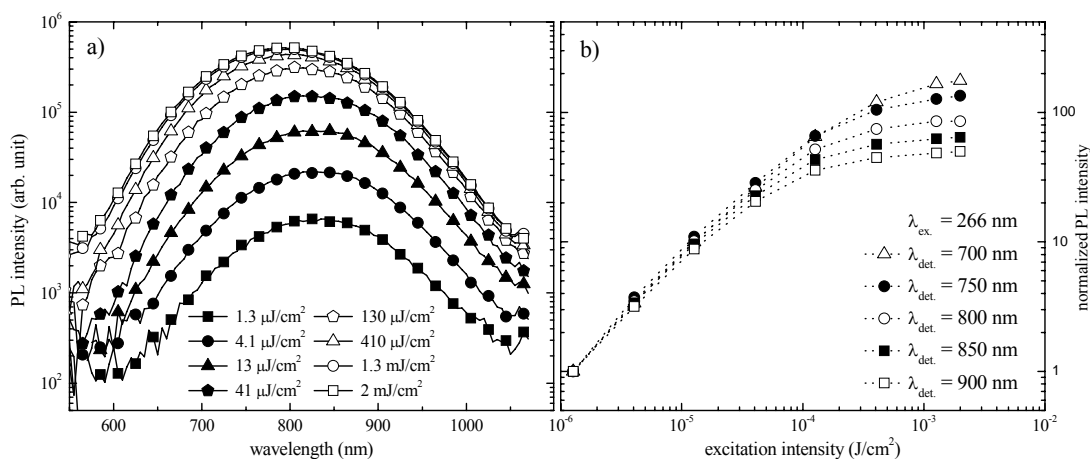
Fig. 4.20. a) Evolution of the PL spectra of nc-Si embedded in SiO_2 for different excitation intensities. The spectra were taken at room temperature with the 266 nm excitation line of an Nd:YAG laser as the exciting source. b) Excitation intensity dependence of the normalized PL signals at five detection wavelengths.

within the same nanocrystal and new non-radiative recombination routes can take place reducing the PL quantum yield. Again, the Auger process has been suggested. During the collision of two excitons, one electron-hole pair recombines non-radiatively, releasing its energy to the other one. One of the remaining carriers, the electron, gains the energy of the recombined pair and can escape from the crystallite. As a result, the nanocrystallite is ionized, and all further radiative recombinations are suspended.

4.2.2.4. Conclusion

The origin of the multi-exponential behavior of the decay curves of a single quantum dot is not well understood. The multi-exponential decay dynamics is due to fluctuating lifetimes caused by fluctuations of non-radiative decay rates. Since surface and other external trapping states provide sources of non-radiative recombination channels, the fluctuating lifetimes must reflect fluctuations in the coupling of the excited state with non-radiative trap states.[135] Therefore, in an ensemble of quantum dots, the multi-exponential feature of the decay traces is believed to reflect the macroscopic dispersion of traps. Photoionization associated with PL intermittency (blinking) may also contribute.[134] Again, the multi-exponential behavior of an ensemble of nanoparticles is also believed to be affected by the exciton transfer from an excited nanocrystal, which acts as a donor, to a neighboring acceptor, where it may become trapped for an extended time and thereafter recombines.[137, 160] Studying the PL properties of nc-Si/SiO_2 systems implanted with foreign atoms is an instructive method to understand the mechanism responsible for the multi-exponential decay dynamics since it may modify the concentration of traps at the nanoparticle's interface and in the surroundings.

5. Ion implantation into nc-Si/SiO$_2$

This chapter deals with the investigation of the optical and structural properties of fused silica windows containing luminescent silicon nanocrystals (nc-Si/SiO$_2$ systems) that were synthesized by Si-implantation and subsequent annealing, and into which additional atomic elements have been incorporated. The incorporation procedure consists of the post-implantation of additional ions at the same penetration depth where the nc-Si are localized (~150 nm), followed by a post-annealing performed at high temperature.

Taking into account the astrophysical aspect of this work, the incorporation procedure has been first applied to atomic elements encountered in silicates. The purpose is to simulate the conditions for silicates containing nc-Si. The incorporation procedure essentially results in the quenching of the PL originating from nc-Si.

In a glass matrix, the effective absorption cross section of Er^{3+} is considerably enhanced by the presence of nc-Si because of their large absorption cross section. Therefore, nc-Si/SiO$_2$ systems are promising host matrices for the emission line of Er^{3+} at 1.536 μm, an emission wavelength that is interesting for optical telecommunication technology. Incorporating Er into our nc-Si/SiO$_2$ systems, we take benefit of the Er^{3+} emission to understand the quenching mechanisms caused by the incorporation of additional atomic elements.

PL originating from the recombination of excitons confined within the nanocrystal volume has been previously observed for Si$_{1-x}$Ge$_x$ alloy nanocrystals (nc-Si$_{1-x}$Ge$_x$) produced by a cosputtering technique.[125] It was found that the PL energy changed from the band gap of nc-Si to that of nc-Ge as the Ge concentration increases.[125] The last sections deal with the synthesis of nc-Si$_{1-x}$Ge$_x$, applying either the sequential incorporation procedure into our nc-Si/SiO$_2$ systems, or the Si and Ge coimplantation method in fused silica windows. The strong resemblance of the as-obtained PL spectra with those previously obtained by the incorporation of other atomic elements into nc-Si/SiO$_2$ systems provides new approaches for the understanding of the PL quenching mechanisms.

5.1. Incorporation of various atomic elements into nc-Si/SiO$_2$

In order to simulate the conditions for silicates, which have already been identified in space,[7, 8, 9] Mg$^+$, Ca$^+$, Na$^+$, P$^+$, S$^+$, and Fe$^+$ ions have been post-implanted into luminescent nc-Si/SiO$_2$ systems. The implantations energies have been chosen to provide the same range of around 150 nm for all types of ions where nc-Si are localized. Because of the ion-beam irradiation, the nc-Si are seriously damaged, and, as a result, the PL is seriously quenched. However, Pacifici et al.[74] demonstrated that it is possible to recover the original luminescence of the nc-Si irradiated with various ions by applying to the samples a post-annealing at high temperature above 800 °C. The next sections deal with the effect of the ion fluence and the post-annealing temperature on the partial recovery of the original PL in nc-Si/SiO$_2$ systems that are post-implanted with various ions. Interestingly, we have also observed a surprising compensation effect when we incorporated P into nc-Si/SiO$_2$ systems into which Ca was already incorporated. Time-resolved PL, optical transmission spectroscopy, structural investiga-

tions by TEM, and simulations of ion implantations using the SRIM-2003 software are used to advance various models that explain the observations concerning the PL spectra of our post-implanted nc-Si/SiO$_2$ systems.

5.1.1. Photoluminescence

5.1.1.1. Incorporation of Mg into nc-Si/SiO$_2$

Two samples were synthesized by implantation of 100-keV Si$^+$ ions in fused silica windows with an ion fluence of 1×10^{17} ions/cm^2 followed by an annealing at 1100 °C in flowing N$_2$ during one hour. The samples exhibited strong visible Vis-NIR luminescence due to the presence of nc-Si. The implantation and annealing conditions were chosen to obtain the strongest luminescence with regard to the results reported in Sec. 4.2.1. and previous studies available in the literature. However, in spite of the fact that the synthesis conditions were definitively identical, some discrepancies between the resulting PL spectra were sometimes observed. Therefore, PL measurements were performed after the synthesis to verify that the PL peaks were defined by an identical position, intensity and shape. One of these samples was subsequently post-implanted with 74-keV Mg$^+$ ions with an ion fluence of 2×10^{16} ions/cm^2. The PL completely disappeared suggesting that the nc-Si were seriously damaged by the Mg$^+$ ion irradiation. Carrying out a post-annealing at 900 °C partly recovered the original PL of the nc-Si, as can be seen in Fig. 5.1 which shows the effect of Mg incorporation into nc-Si/SiO$_2$ systems on the PL spectra. In order to allow a proper comparison, the sample that was not implanted with Mg$^+$ ions was also subjected to the post-annealing. It is found that the incorporation of Mg significantly quenches the PL of nc-Si. We find that the PL originating from Mg-incorporated nc-Si/SiO$_2$ systems is at least 70 times weaker than in the sample without Mg. The dotted curve shows the luminescence of a fused silica window into which only Mg$^+$ ions were implanted. This sample was also annealed under the same conditions. It reveals a broad PL band peaking around 540 nm which is attributed to defect sites in SiO$_2$. This peak is also present in the sample containing both nc-Si and Mg.

In order to further study the effect of Mg-incorporation into our nc-Si/SiO$_2$ systems on the PL, a second set of samples was prepared following the same procedure just described,
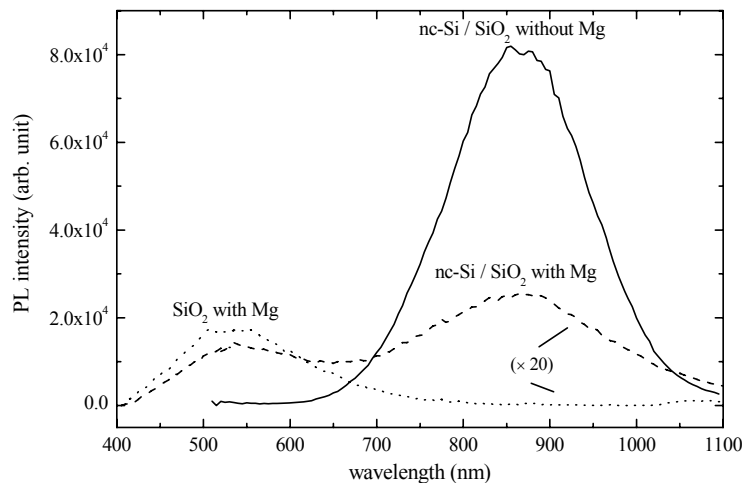

Fig. 5.1. PL spectra of a nc-Si/SiO$_2$ sample (*continuous line*), of a nc-Si/SiO$_2$ sample post-implanted with Mg$^+$ ions (*dashed line*), and of fused silica sample implanted with Mg$^+$ ions (*dotted line*). The two PL spectra of Mg-doped samples are multiplied by a factor of 20 for clarity.
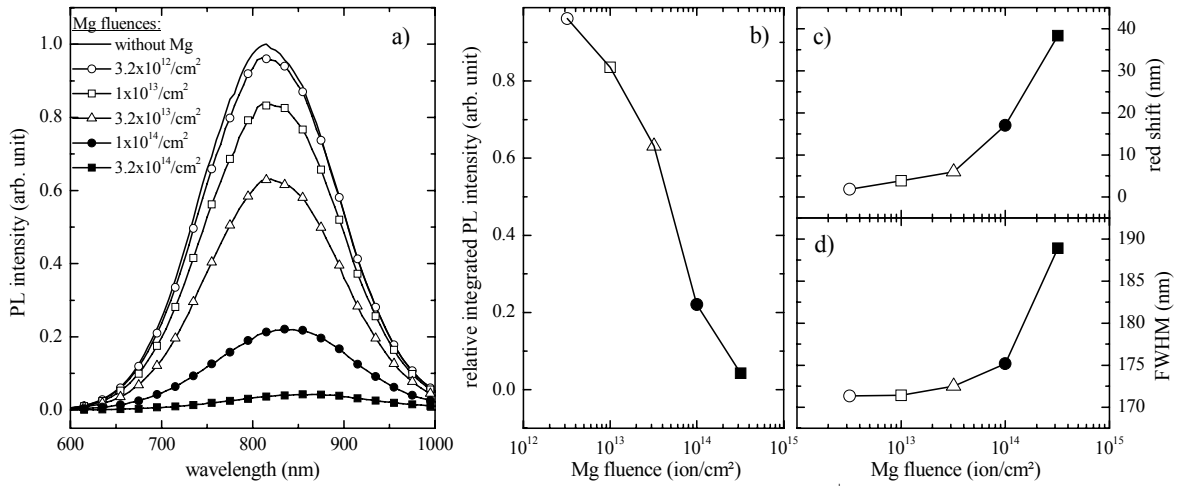
Fig. 5.2. a) PL spectra of nc-Si/SiO$_2$ systems post-implanted with Mg$^+$ ions and subsequently post-annealed at 900 °C (the sample containing no Mg included) in N$_2$ during one hour. b) Integrated PL intensity of Mg-incorporated nc-Si/SiO$_2$ systems, derived from panel a) as a function of the Mg$^+$ ion fluence. c) Red shift of the PL peaks of Mg-incorporated nc-Si/SiO$_2$ systems as a function of the Mg$^+$ ion fluence. d) Width of the PL peaks of Mg-incorporated nc-Si/SiO$_2$ systems versus Mg$^+$ ion fluence. The maximum position and the width of each spectrum were obtained by fitting the data with a log-normal function. The samples were excited with the 266 nm light of a Nd:YAG laser with an excitation energy fluence of 130 µJ/cm^2.

but with lower Mg$^+$ ion fluences ranging from 3.2×10^{12} to 3.2×10^{14} ions/cm^2. Figure 5.2.a shows the effect of Mg-incorporation into nc-Si/SiO$_2$ systems on the PL spectra with various Mg concentrations. In contrast to the previous measurements, no PL band peaking around 540 nm was observed. Since the highest Mg$^+$ ion fluence is more than 50 times lower than in the previously reported experiment, we assume that the Mg concentration is too weak to form enough suchlike defect sites in the host matrix. The PL intensity and integrated PL intensity (see Fig. 5.2.b) originating from the nc-Si decrease progressively with increasing Mg$^+$ ion fluence. At low fluence (3.2×10^{12} ions/cm^2), the effect is rather small, but when the Mg$^+$ ion fluence is further increased, the PL of nc-Si is progressively quenched. For a Mg$^+$ ion fluence of 3.2×10^{14} ions/cm^2, the integrated PL intensity is 25 times weaker than in the sample without Mg. Figure 5.2.c shows the progressive red shift of the PL peaks with increasing Mg$^+$ ion fluence with respect to the sample containing only nc-Si. In the same way as the PL quenching, at low fluence the red shift is rather small, but when the Mg$^+$ ion fluence is further increased, the PL of nc-Si is progressively shifted to longer wavelengths. At a Mg$^+$ ion fluence of 3.2×10^{14} ions/cm^2, the PL spectrum is shifted by 39 nm. Together with the quenching and red shift, we also observed a progressive broadening of the PL peak with increasing Mg$^+$ ion fluence as can be seen in Fig. 5.2.d.

Surprisingly, the red shift previously shown in Fig 5.1 is only about 10 nm although the Mg$^+$ ion fluence was considerably higher (2×10^{16} ions/cm^2). But, in the previous PL measurements, the excitation intensity used with the Mg-implanted samples was more than two times higher than for the sample containing pure nc-Si. And, since a strong excitation intensity leads to a blue shift of the PL spectrum (see Sec. 4.2.2.3.), we believe that the small red shift is caused by the contribution of this latter effect. PL measurements performed on several other Mg-incorporated nc-Si/SiO$_2$ systems confirm the reproducibility of the observations reported in Fig 5.2. Moreover, employing other atomic elements, for instance Ca, Na,

and P, resulted in similar effects on the PL of nc-Si/SiO$_2$ systems: PL quenching, inherent red shift and broadening. Therefore, in the following, we present our more interesting results regarding various atomic elements. All results concerning the effects of the additional ions that were post-implanted into nc-Si/SiO$_2$ systems on their PL properties are summarized in Sec. 5.1.1.5.

5.1.1.2. Ca-incorporation into nc-Si/SiO$_2$ with various size distribution of nc-Si

Four samples were synthesized by 100-keV Si$^+$ implantation in fused silica windows with ion fluences ranging from 5×10^{16} to 2×10^{17} ions/cm^2 followed by an annealing at 1100 °C. Increasing the Si ions fluences allows us to shift the nc-Si size distribution to larger nanoparticles (see Sec. 4.2.1.6). Each sample was cut into two parts. One part was implanted with 137-keV Ca$^+$ ions with an ion fluence of 3.2×10^{13} ions/cm^2, the other one served as reference. The implantation energy of Ca$^+$ ions provides the same range as for Si$^+$ ions. Figure 5.3.a shows the effect of Ca-incorporation into nc-Si/SiO$_2$ systems on the PL spectra with various size distributions of nc-Si. The PL spectra are quenched and shifted to longer wavelength in the same way as reported with Mg-incorporation (Sec. 5.1.1.1.). However, Ca affects the PL originating from nc-Si to a larger extent. The atomic size dependence of the PL quenching is further discussed in section 5.1.6. For a Si$^+$ ion fluence of 1×10^{17} ions/cm^2 and a Ca$^+$ ion fluence of 3.2×10^{13} ions/cm^2, the integrated PL intensity is 2.6 times weaker than the one of the sample in which only Si$^+$ ions were implanted, and the PL spectrum is shifted by 37 nm. In comparison, for identical Si$^+$ and Mg$^+$ ion fluences, the integrated PL intensity is only 1.6 times weaker and the PL spectrum is only shifted by 6 nm. Figure 5.3.b shows the PL red shift plotted as a function of the Si$^+$ ion fluence. The PL red shift increases as the size distribution of nc-Si is shifted to larger particles, since longer emission wavelengths are characteristic of larger nanocrystals according to the quantum confinement model. However, the ratio between the integrated PL intensity of the Ca-incorporated nc-Si/SiO$_2$ and that of the reference samples is rather constant as the Si$^+$ ion fluence changes, see Fig. 5.3.c.
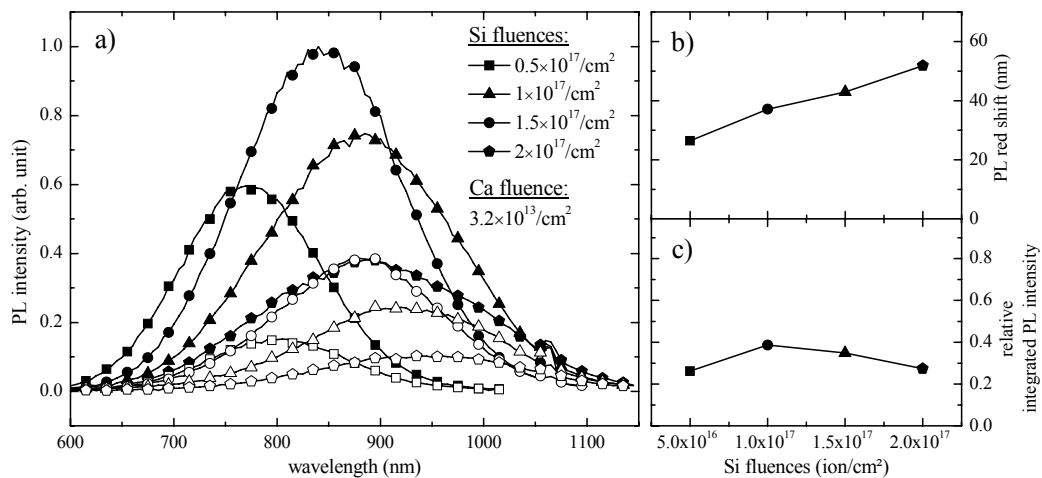
Fig. 5.3. a) PL spectra of nc-Si/SiO$_2$ systems synthesized by Si-implantation with different Si$^+$ ion fluences (*full symbols*), and of the same nc-Si/SiO$_2$ systems post-implanted with Ca$^+$ ions (*open symbols*) and subsequently post-annealed at 900 °C (the sample containing no Ca included) in N$_2$ during one hour. b) In nc-Si/SiO$_2$ systems, PL red shift caused by the Ca incorporation as a function of the Si$^+$ ion fluence. c) Integrated PL intensity of Ca-incorporated nc-Si/SiO$_2$ systems relative to the one of the pure nc-Si/SiO$_2$ sample versus the Si$^+$ ion fluence.

5.1.1.3. P-incorporation into nc-Si/SiO$_2$: the role of the post-annealing temperature

Figure 5.4.a shows the effect of P-incorporation into nc-Si/SiO$_2$ systems on the PL spectra. Note that the PL intensity is plotted on a logarithmic scale. After a post-annealing at 900 °C, the post-implanted samples recover only a weak proportion of the PL originating from the nc-Si (*open symbols*). The PL intensity decreases with the increase of the P$^+$ ion fluence from 1×10^{14} to 3.2×10^{14} ions/cm^2; while above the latter value the PL intensity increases again. In the same way as was previously observed with the incorporation of Mg and Ca, one can see that the more the PL is quenched, the more the PL peak is shifted to longer wavelengths. The red shift varies between 45 to 70 nm with respect to the sample containing only nc-Si. Proceeding to a second post-annealing at 1100 °C (*full symbols*), the PL intensity increases significantly. For low P$^+$ ion fluences, the PL of doped nc-Si/SiO$_2$ even exceeds that of pure nc-Si. The integrated PL intensity is slightly increased by a factor varying between 4 to 11% relative to the integrated PL intensity of the sample containing only nc-Si. For the highest P$^+$ ion fluence (3.2×10^{15} ions/cm^2), the PL remains quenched, but to a much lower extent than after the first post-annealing at 900 °C. One can also clearly see that the red shift of the PL spectra observed after the second post-annealing at 1100 °C is less pronounced. However, it is still present even in the samples where the PL is enhanced, and it increases progressively from 11 to 55 nm with increasing P$^+$ ion fluence.

Phosphorus and boron are the most widely used dopants for silicon; they are also believed to change the electronic band structure of nc-Si. In bulk silicon, the ionization energy levels of P-donors and B-acceptors are located close to the conduction and valence bands, respectively. At room temperature, P and B provide a free carrier leading to a well-known doping effect. An introduction of additional charge carriers in nc-Si/SiO$_2$ systems is believed to result in the quenching of the luminescence caused by the Auger interaction between the free carriers and photogenerated excitons. In this model, the exciton energy is not emitted in the form of a photon, but transferred to a third charge carrier.

Previous studies on the post-implantation of P$^+$ and/or B$^+$ ions in nc-Si/SiO$_2$ systems

Fig. 5.4. a) PL spectra of nc-Si/SiO$_2$ systems post-implanted with P$^+$ ions and followed by a first post-annealing at 900 °C (*open symbols*) and a second one at 1100 °C (*full symbols*)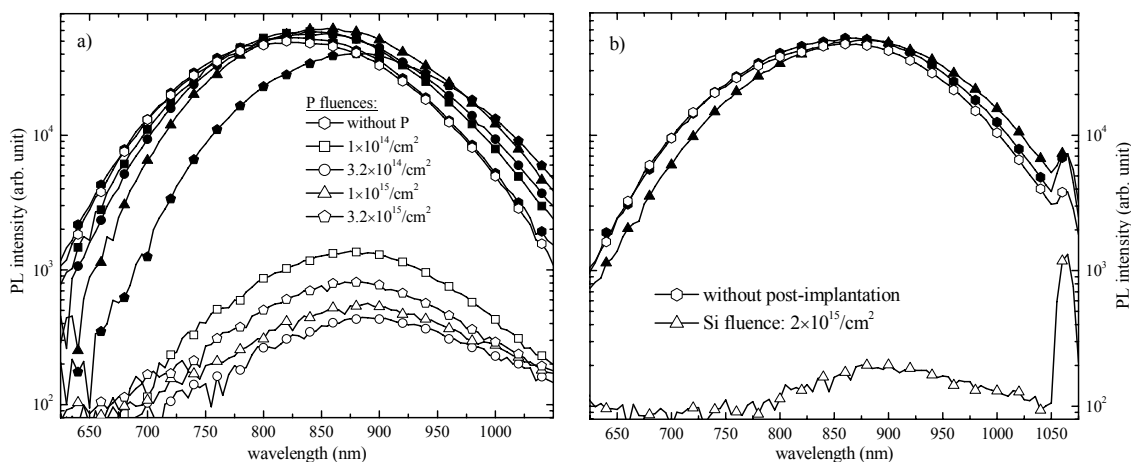. b) PL spectra of nc-Si/SiO$_2$ systems post-implanted with Si$^+$ ions followed by a first post-annealing at 900 °C (*open symbols*) and a second one at 1100 °C (*full symbols*). The 1064 nm-PL peak originates from the remaining light of the fundamental line of the Nd:YAG laser.

followed by a post-annealing at high temperature showed that for high dopant ion fluences the PL originating from nc-Si was significantly decreased, supporting the latter model.[43, 44, 172] Doping nc-Si embedded in SiO$_2$ with boron[42, 48] and phosphorus[45, 173] during their synthesis by sputtering Si in combination with SiO$_2$ and B$_2$O$_5$, or SiO$_2$ and P$_2$O$_5$, respectively, with a subsequent annealing resulted in an analogous PL decrease for high dopant concentrations. However, the results concerning this synthesis technique are controversial since, in the case of P, for instance, using the same dopant concentrations and annealing conditions, either enhancement[41] or quenching[45, 173] of the PL have been observed. Finally, an earlier report on spin-on doping of porous Si with either B or P revealed a similar effect on the PL properties originating from the porous Si,[174] supporting the hypothesis that quenching is dominant at high dopant concentrations.

Kachurin *et al.*[172] reported on the role of the post-annealing temperature in the PL properties of nc-Si/SiO$_2$ systems which were post-implanted with P$^+$ ions. The behavior of their PL spectra as a function of the dopant concentration employing a post-annealing temperature of 1000 °C was similar to ours at 900 °C. They also noticed a progressive decrease of the PL intensity originating from the nc-Si inherent with a shift to longer wavelengths as the P$^+$ ion fluence increased from 1×10^{13} to 3×10^{15} ions/cm^2, except for the higher P$^+$ ion fluence (3.2×10^{16} ions/cm^2). However, since they used a higher post-annealing temperature, their general PL decrease was less pronounced. In their study, an increase in the heat treatment temperature to 1100 °C gave rise to a better recovery of the PL intensity and a reduction of the red shift. For the lowest P$^+$ ion fluences, the PL intensity of P-doped nc-Si was also found to exceed the intensity measured before the post-implantation of P$^+$ ions. However, since they had not post-annealed their non-doped sample, in contrast to our experimental procedure, we cannot directly compare the two experiments.

The enhancement of the PL of P-doped nc-Si/SiO$_2$ at low P concentration has been previously observed by many researchers.[43, 45, 172, 173] An explanation of the enhancement of the PL has been partly given by electron spin resonance measurements, which showed that P atoms improve the passivation of the nc-Si by contributing to the reduction of the number of silicon dangling bonds at the nanoparticle surface.[41, 45] However, indications in Raman spectra[44] suggested that the PL enhancement is also due to the promotion of crystallization caused by impurities. This picture is also supported by the fact that an enhancement of the PL was also observed in B-doped samples at low B concentrations.[44] Thus, enhancement should not only be attributed to an increase of the passivation quality. The PL quenching is explained by the inclusion of dopant atoms in the nc-Si volume, which is supposed to suppress drastically the PL caused by non-radiative Auger recombination.[41, 45]

In order to elucidate the effect of the second implantation irrespective of the element used, we have also incorporated Si into nc-Si/SiO$_2$ systems (see Fig. 5.4.b). Again, we observed a similar behavior of the PL spectra with the post-annealing conditions. The sample post-implanted with Si ions recovers only a weak proportion of the PL originating from the nc-Si after a post-annealing at 900 °C (*open symbols*) and totally after a second post-

annealing at 1100 °C (*full symbols*). Interestingly, although the vacancies generated by Si$^+$ and P$^+$ ions irradiation are very close, the nc-Si/SiO$_2$ sample recovers less luminescence with Si than with P for the same ion fluence range after a post-annealing at 900 °C. The role of P in the passivation of nc-Si can be advanced. In the same way as for the P-incorporation, the PL peak is strongly shifted to higher wavelengths (red shift = 39 nm) after the first post-annealing at 900 °C and shifts to shorter wavelengths (red shift = 11 nm) when post-annealing the sample once more at 1100 °C. Apparently, the decrease of the red shift cannot be attributed to a modification of the size distribution of nc-Si, since it is known that particle size increases with annealing time and temperature which leads to a red shift of the PL spectra according to the quantum confinement model (see Sec. 4.2.1.5.). Moreover, the PL spectra of the pure sample remain unchanged after the two post-annealing. In addition, according to TEM data,[41, 48] the incorporation of P into nc-Si/SiO$_2$ systems does not affect the size distribution of nc-Si. As a consequence, the red shift could thus be attributed to a modification of the size distribution of optically active nc-Si. However, for a given concentration of defects, smaller nc-Si should have fewer defects than larger ones. As a result, smaller particles would emit PL with higher efficiency than larger ones resulting in a blue shift of the PL spectra (see Sec. 2.2.2.2.). This explanation is also supported by the theoretical calculations of Cantele *et al.*[175] who showed that for smaller nc-Si a larger energy is needed for the formation of impurities. Moreover, they also found that the activation energy of impurities decreases with the size, showing that for smaller nc-Si it would be very difficult to activate the impurities.

5.1.1.4. Incorporation of Ca and P into nc-Si/SiO$_2$

Figure 5.5 shows the PL behavior of nc-Si/SiO$_2$ systems post-implanted with Ca$^+$ ions and subsequently post-annealed at 900 °C (*continuous lines*). The overall PL behavior is similar to those previously reported on Mg-incorporation in Fig. 5.2. The PL intensity decreases and the PL peaks shift to longer wavelengths with increasing the Ca$^+$ ion fluence. It is striking to see how the PL spectra of nc-Si/SiO$_2$ systems into which Ca was previously incorporated change after the post-implantation of P$^+$ ions followed by a post-annealing at 900 °C (*dotted lines*). The intensities of the PL spectra are further decreased due to the incorporation of P while, however, in contrast to the previous observation, the order is reversed, *i.e.*, the PL intensity is less decreased when the concentration of Ca is increased. The PL quenching caused by the incorporation of P is thus partly compensated by the presence of Ca. Fujii *et al.*[48, 176] have already reported on a compensation effect of B and P codoping on the PL of nc-Si/SiO$_2$ systems. Their nc-Si/SiO$_2$ samples were codoped with B and P during the synthesis by sputtering Si in combination with SiO$_2$, B$_2$O$_5$, and P$_2$O$_5$. By doping nc-Si/SiO$_2$ with B the PL intensity decreased significantly and the PL spectra were shifted to longer wavelengths. Doping simultaneously nc-Si/SiO$_2$ with B and P resulted in an enhancement of the PL intensity in comparison with the samples only doped with B. The PL peaks were also greatly shifted to the red part of the spectrum and even crossed the band gap of bulk crystalline silicon which was a convincing indication that the luminescence mechanism was different from that of pure nc-Si. They suggested that the radiative recombination process was dominated by non-
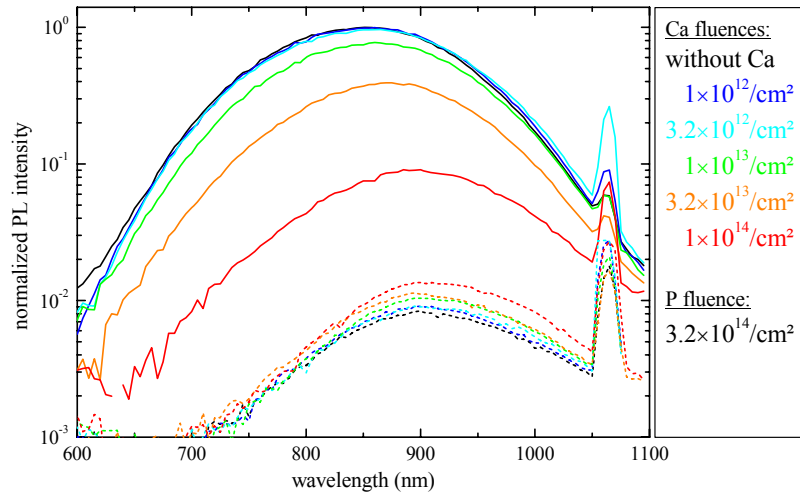
Fig. 5.5. Effect of post-implantation of P$^+$ ions on nc-Si/SiO$_2$ systems into which Ca was previously incorporated. PL spectra of nc-Si/SiO$_2$ systems post-implanted with 137-keV Ca$^+$ ions with various ion fluences and post-annealed at 900 °C in N$_2$ during one hour (*continuous lines*). PL spectra of the latter samples subsequently post-implanted with 104-keV P$^+$ ions with an ion fluence of 3.2×10^{14} ions/cm^2 and post-annealed at 900 °C (*dotted lines*). The 1064 nm-PL peak originates from the remaining light of the fundamental line of the Nd:YAG laser.

phonon-assisted quasidirect optical transitions between the donor and acceptor states in the band gap of nc-Si. In our samples, such a mechanism could also occur if, however, Ca^{2+} ions can act as acceptor in nc-Si.

5.1.1.5. Summary

Figure 5.6 shows the effect of the incorporation of various atomic elements into nc-Si/SiO$_2$ systems with various concentrations in the host matrix. The atomic concentrations of the various elements resulting from the ion implantations were estimated using the SRIM-2003 software (see Sec. 5.1.5). By applying a post-annealing to the samples at 900 °C, the PL recovery is found to depend on the ion mass for the lighter ions, *i.e.* Na$^+$, Mg$^+$, and Ca$^+$. However, this behavior is inverse considering Er$^+$ ions. Tchebotareva *et al.*[43] had previously revealed that the recovery of the PL was more pronounced when they incorporated Au rather than P, whereas Kachurin *et al.*,[44] who compared B and P incorporation into nc-Si/SiO$_2$ (two light ions), showed that the particle mass dependence of the PL recovery was inverse. Therefore, it is reasonable to assume that the PL recovery is not crucially dependent to the density of elastic displacements produced by the ion irradiation, as heavier ions induce more vacancies than lighter ones (see Fig. 5.9). But, we rather believe that the implanted atomic elements affect the crystallization and/or the passivation of the nanoparticles.

For the sake of completeness, it should be mentioned that 173-keV Fe$^+$ ions were also post-implanted into nc-Si/SiO$_2$ systems with two Fe$^+$ ion fluences of 1×10^{13} and 1×10^{14} ions/cm^2 followed by a post-annealing at 900 °C, but no PL could be observed. We post-implanted S as well (116-keV S$^+$ ions) into our luminescent nc-Si/SiO$_2$ samples with two S$^+$ ion fluences of 1×10^{14} and 1×10^{15} ions/cm^2. We post-annealed the samples under the same conditions, but only a very weak PL could be observed.
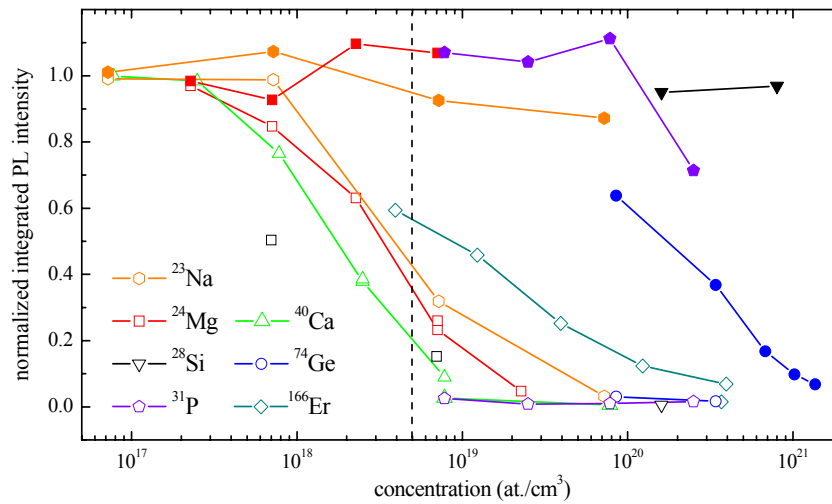
Fig. 5.6. Effect of the incorporation of various ions into nc-Si/SiO$_2$ systems on the integrated PL intensity relative to the one of pure nc-Si/SiO$_2$. The nc-Si/SiO$_2$ systems were all produced by Si implantation in fused silica with an ion fluence of 1×10^{17} /cm^2 followed by an annealing at 1100 °C in N$_2$ during one hour. After the post-implantation, the samples were post-annealed at 900 °C (*open symbols*) in N$_2$ during one hour, and some samples were post-annealed a second time at 1100 °C (*full symbols*). The vertical dashed line represents the average concentration of nc-Si.

Furthermore, submitting the data to the model of Pacifici *et al.*,[74] which relates the fraction of quenched optically active nc-Si to the total defect concentration in the host matrix and to the value of the nc-Si volume itself, and considering a foreign atom as a defect, it seems that the quenching of the PL observed after a post-annealing at 900 °C is not due only to Ca- and Mg-incorporation into the nc-Si volume. Therefore, we believe that residual structural damages in the nc-Si core or dangling bonds at the nanoparticle surface are still present. In the model of Pacifici *et al.*, one defect in the nc-Si volume is supposed to radically inhibit the PL (see Sec. 2.2.2.2.). Moreover, following this model, an increase of the concentration of defects induces a blue shift of the PL spectra, while, in our samples, a red shift has always been observed, except for Er-incorporation. Indeed, it seems that the quenching mechanism is different for heavy and light ions, as it has been previously demonstrated by comparing the P- and Au-incorporation into nc-Si/SiO$_2$ systems.[43]

As can be seen in Fig 5.6, the integrated PL intensity is considerably increased by performing a second post-annealing at 1100 °C. For some samples the PL intensity was even slightly enhanced. The increase of the PL can be explained by a reduction of the damage caused by the ion implantation and/or by the improvement of the passivation of the nc-Si. However, at atomic concentrations above ~10^{20} at./cm^3, no PL is expected considering one additional atomic element as a defect which kill the PL. Indeed, for a mean nanoparticle diameter of 4 nm, the fraction of nanocrystals able to emit light is close to zero at this concentration (see Fig. 2.10) according to the model of Pacifici *et al.*[74] Therefore, two hypotheses can be advanced. One can suggest that, during the post-annealing, the foreign ions are expelled from the nc-Si so that they reside either at the interface between the nc-Si and the SiO$_2$ matrix or deeper in the host matrix. One of the carriers of the photogenerated electron-hole pair can be trapped by the additional ion at the interface. The free carrier remaining in the nc-Si core acts as defect inhibiting any further radiative recombinations. This picture can ex-

plain the observed red shift with the increase of the foreign atom concentration in our samples. In a second picture, a fraction of the foreign atoms, which are incorporated into the nc-Si core either by substitution of Si atoms or by insertion into a lattice interstice, do not act as a defect that radically inhibits the PL, but, they induce some local modifications of the lattice structure resulting in a decrease of the band gap of nc-Si, and thus explains the observed red shift.

5.1.2. Time-resolved photoluminescence

Figure 5.7.a shows the PL behavior of nc-Si/SiO$_2$ systems post-implanted with Ca$^+$ ions and followed by a post-annealing at 900 °C with increasing Ca$^+$ ion fluence. In the time domain, the registration of the decay curves was performed at several wavelength positions of the PL spectra. The PL decay curves were measured up to a Ca$^+$ ion fluence of 3.2×10^{13} ions/cm^2, above this value the signal to noise ratio was too high because of the strong quenching of the luminescence. PL measurements show that the luminescence intensity does not change when implanting Ca$^+$ ions with a low ion fluence of 3.2×10^{12} ions/cm^2 (Fig. 5.7.a). At the same time, the lifetimes remain almost unchanged (Fig. 5.7.b). When the Ca concentration is further increased, the PL intensity decreases significantly. At the same time the lifetimes decrease as well. The shortening of the decay lifetimes (increase of the decay rates) is independent of the emission energy of the PL spectra (Fig. 5.7.c), and, thus, cannot explain the small red shift observed in the wavelength domain.

Pacifici et al.[74] studied the formation and annihilation of defects produced in nc-Si/SiO$_2$ systems by ion-beam irradiation. Their samples, which were produced by PECVD, were irradiated with He$^+$, Si$^+$, Ge$^+$, and Au$^+$ ions. The ion beam energy was chosen such that the ions are located beyond the films containing nc-Si. They observed that when they increased the ion fluence, the PL intensity and the lifetime decreased. They demonstrated that
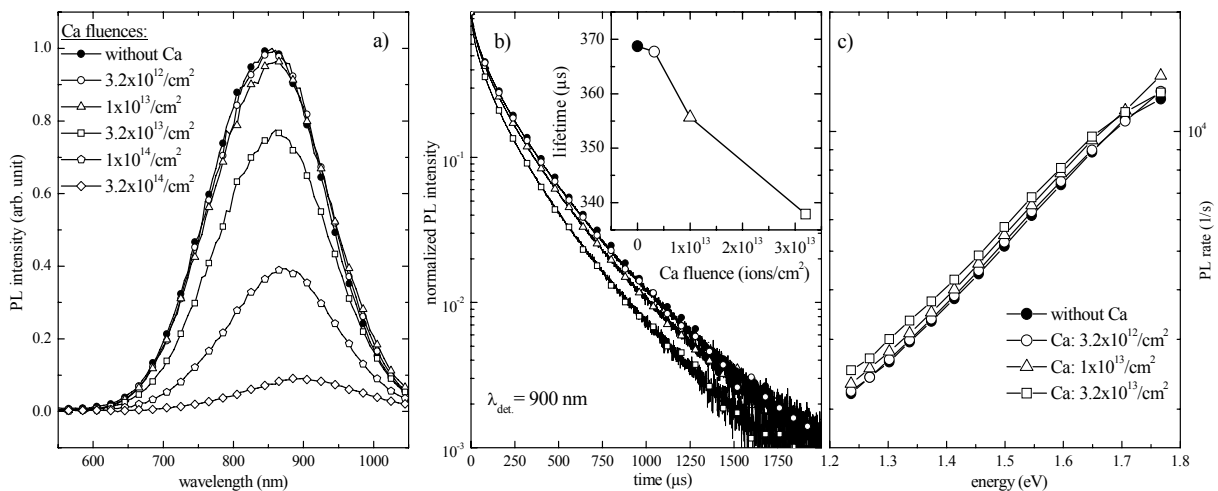
Fig. 5.7. a) PL spectra of nc-Si/SiO$_2$ systems post-implanted with Ca$^+$ ions and subsequently post-annealed at 900 °C in N$_2$ during one hour. b) PL decay curves of nc-Si/SiO$_2$ systems post-implanted with Ca$^+$ ions with different ion fluences and subsequently post-annealed at 900 °C. The inset shows the lifetimes of the respective samples as a function of the Ca$^+$ ion fluence. The PL lifetimes were evaluated by fitting log-normal lifetime distributions to the measured data using the maximum entropy method of data analysis.[140] c) PL rates of nc-Si/SiO$_2$ post-implanted with Ca$^+$ ions and subsequently post-annealed at 900 °C as a function of PL emission energy.

just one defect inside the nanoparticle quenches its luminescence. Besides, they showed that complete amorphization of nc-Si occurs at low ion fluences since 2×10^{13} ions/cm^2. Moreover, they studied the recovery of the damaged nc-Si by performing both isochronal and isothermal annealings. They showed that nc-Si/SiO₂, damaged with 2-MeV Si ions with an ion fluence of 2×10^{13} ions/cm^2, recovered completely its original luminescence without any change in the shape of the PL spectra either by a post-annealing at 900 °C during 3 hours or by a post-annealing at 1100 °C during only 5 min. Therefore, in our samples post-annealed at 900 °C during one hour only, the PL shortening can be partly explained by an increase of the non-radiative rates due to the presence of residual defects within or at the nanoparticle surface caused by the ion irradiation. One could also assume that the PL shortening is also caused by the incorporation of additional charge carriers into nc-Si/SiO₂ systems resulting in an increase of Auger interactions between the free carriers and photogenerated excitons. Although such PL shortening has also been observed by other researchers in nc-Si/SiO₂ samples incorporated with P and Au by ion implantation followed by a post-annealing at 800 °C in a (8% H₂ in N₂) gas flow,[43] and in nc-Si/SiO₂ samples incorporated with Er by ion implantation and subsequent post-annealing at 900 °C in N₂,[19] its mechanism is not well understood. The effect of post-implantation of Er$^+$ ions into nc-Si/SiO₂ samples is further discussed in Sec. 5.2.

Figure 5.8 shows the PL decay curves of nc-Si/SiO₂ systems post-implanted with Mg$^+$ ions followed by a post-annealing at 900 °C and by a second post-annealing at 1100 °C. In the frequency domain, the integrated PL intensity of the respective sample post-annealed at 900 °C is decreased by a factor of 0.63 compared to the integrated PL intensity of the pure sample (see Fig. 5.2), whereas the integrated PL intensity of the respective sample that was subjected to a second post-annealing at 1100 °C is slightly increased by a factor of 1.07. It is clearly seen that, by carrying out to the second post-annealing, the lifetime of the sample into which Mg has been incorporated increases and its decay curve matches completely the one containing only nc-Si. Therefore, we assume that the PL shortening observed at 900 °C is mainly due to residual damages in the Si nanoparticles that do not totally recover their crystalline structure or are not well passivated after the post-annealing at this temperature. This is also supported by the fact that, for instance, for an Mg$^+$ ion fluence of 3.2×10^{13} ions/cm^2 that corresponds to an Mg concentration peak of about 2.3×10^{18} at/cm^3, according to SRIM
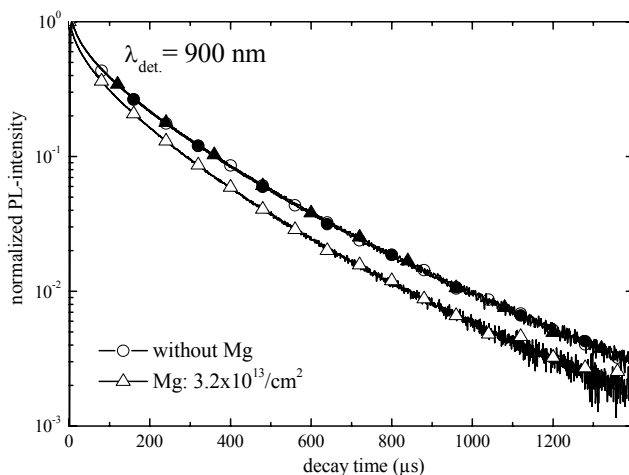

Fig. 5.8. PL spectra of a pure nc-Si/SiO₂ sample and a sample post-implanted with Mg$^+$ ions with an ion fluence of 3.2×10^{13} ions/cm^2 and post-annealed at 900 °C (*open symbols*) and followed by a second post-annealing at 1100 °C (*full symbols*) in N₂ during one hour.

simulation, the integrated PL intensity is decreased by a factor of 0.63, whereas at this Mg concentration 93% of the silicon nanoparticles should be optically active according to the model of Pacifici *et al.* considering one Mg atom as a defect inside the nanoparticle volume.

5.1.3. Optical transmission spectroscopy

The optical transmission spectra of nc-Si/SiO$_2$ samples implanted with Ca$^+$ or with Mg$^+$ ions at low ion fluence ($\leq$ 1 × 10^{15} ions/cm^2) and subsequently annealed at 900 °C were compared with a pure nc-Si/SiO$_2$ sample in the range from 190 to 3200 nm. No significant difference has been noticed in the UV range, suggesting that neither Mg nor Ca incorporation induced any significant change of the crystalline structure quality. Furthermore, the optical transmission spectra of fused silica windows implanted with Ca$^+$ or with Mg$^+$ ions and subsequently annealed in the same conditions were compared to the one of a non-irradiated window. Again, no significant difference has been noticed, indicating that, at such low ion fluences, the optical transmission remains unchanged, in particular in the visible domain. Therefore, in nc-Si/SiO$_2$ samples, the decrease of the PL intensity and the red shift of the PL spectra observed with increasing foreign ion fluence cannot be attributed to a variation of the optical transmission of the host matrix.

5.1.4. Structural investigation by TEM

In order to investigate the structural properties of nc-Si/SiO$_2$ systems into which foreign atoms were incorporated, a sample post-implanted with Mg$^+$ ions with an ion fluence of 3.2 × 10^{14} ions/cm^2 followed by a post-annealing at 900 °C has been prepared to be imaged by TEM. This sample is characterized by a strong decrease of the PL and a pronounced red shift of its PL spectrum with respect to the pure nc-Si/SiO$_2$ sample (see Fig. 5.2). Compared to the pure nc-Si/SiO$_2$ systems (see Sec. 4.2.1.4.), it was more difficult to distinguish the crystalline nanoparticles from the amorphous host matrix. However, we cannot affirm whether this is due to the TEM-preparation itself or to our Mg-incorporation procedure. The latter case would support the picture that the strong PL decrease is mainly due to the fact that a large portion of nanoparticles are not completely recrystallized after the post-annealing at 900 °C. By analyzing the TEM images, we found an average diameter of 3.4 nm with a FWHM of the size distribution of about 1 nm, which are identical to the one of the pure sample (see Sec. 4.2.1.4.). This size is also very close to the value of 3.3 nm of the corresponding pure nc-Si/SiO$_2$ sample which was calculated using the relation between the nc-Si size and the PL peak position which was established in Fig. 2.22. On the other hand, the calculated size of the sample containing Mg is about 4 nm. Therefore, we believe that the incorporation of foreign atoms into nc-Si/SiO$_2$ systems following our procedure does not affect the size distribution of nc-Si.

5.1.5. SRIM simulations

Ion implantation is a process that consists in accelerating ions which penetrate the target surface and are stopped in the host material. Figure 5.9 shows the calculated distribution profiles, using the SRIM-2003 software,[133] for various atomic elements that were implanted into fused silica windows. One can notice that for all elements, except Er (for which higher
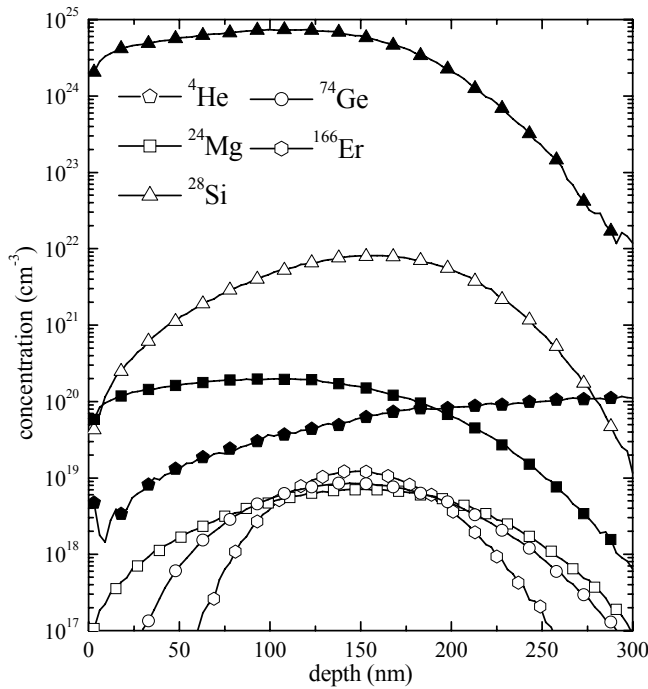
Fig. 5.9. Calculated relative concentration profiles (*open symbols*) and produced vacancy profiles (*full symbols*) of various implanted ions in a silicon dioxide layer. The concentration profiles were calculated for an implantation of 100-keV Si$^+$ ions with an ion fluence of 1×10^{17} ions/cm^2, and for 74-keV Mg$^+$, 208-keV Ge$^+$, and 446-keV Er$^+$ ions with an ion fluence of 1×10^{14} ions/cm^2. The vacancy profiles were calculated for an implantation of 100-keV Si$^+$ and 74-keV Mg$^+$ ions with an ion fluence of 1×10^{17} ions/cm^2 and 3.2×10^{12} ions/cm^2, respectively. The calculated vacancy profile caused by 1.4-MeV He$^+$ ion irradiation with an ion fluence of 1×10^{15} ions/cm^2 is also plotted, for comparison. The displacement threshold energy for Si atoms was set to 15 eV.

energy was used), the concentration profiles match the one of Si taking into account the ference of the ion fluences.

When an energetic ion is stopped in a solid material, it loses its energy in an elastic collision with a host atom, eventually displacing it from its original lattice position if the energy loss is higher than a critical value which is characteristic of the matrix (displacement threshold energy). The vacancy profile produced by the implantations of Mg$^+$ ions (*full squares*) for an ion fluence of 3.2×10^{12} ions/cm^2 is shown in Fig. 5.9. In our nc-Si/SiO$_2$ samples, the average volume of a nc-Si is approximately ~3.3×10^{-20} cm^3, thus, at the depth of 150 nm, where the nc-Si are localized, the amount of Mg$^+$ ions traversing the nc-Si should induce ~6 vacancies per nanoparticle at these Mg ion fluences. Therefore, the PL quenching observed directly after the Mg$^+$ ion irradiation is consistent with the latter estimations even for the lowest ion fluences.

The distribution profile of vacancies caused by 1.4-MeV He$^+$ ion irradiation (*full pentagons*) in fused silica windows is also plotted in Fig 5.9 for comparison. It is clearly seen that the vacancies induced by He$^+$ ion irradiation (He$^+$ ions are passing through the target material), are five orders of magnitude weaker than those caused by Si$^+$ implantation (*full triangles*). When an energetic ion is passing through a solid material, the ion can interact with a host atom by losing energy in electronic or nuclear collisions, being eventually stopped in the host matrix. In the electronic stopping regime, the fast ion loses its energy by interacting with electrons in the solid, producing electronic excitation or ionization. Therefore, high-energetic He$^+$ ion irradiation produces mostly binding defects creating NBOHCs in the SiO$_2$ host matrix, which induce PL peaking at 1.9 eV (see Sec 4.2.1.5). Interestingly, the 1.9-eV luminescence induced by implantation of heavier ions is comparatively less pronounced, because it creates mostly structural defects in the host matrix.

5.1.6. Conclusion

It has been demonstrated that nc-Si/SiO$_2$ samples post-implanted with additional ions recover only a small proportion of their original PL after a post-annealing at 900 °C. The recovery of PL does not follow the picture which considers an incorporated atom in the nc-Si core as a defect that inhibits radically any radiative recombination of photogenerated excitons, at least for light ions (Mg$^+$, Ca$^+$, and Na$^+$ ions). We believe that, after a post-annealing at 900 °C, the PL quenching is mainly due to the presence of residual structural defects caused by the ion irradiation and/or dangling bonds at the nanoparticle surface. Surprisingly, the recovery of the PL is less pronounced for lighter ions than for the heavier Er$^+$ ions, although the implantation of one Er$^+$ ion induces quantitatively more structural defects. This would suggest that light ions hinder the crystallization and/or the passivation mechanisms of the nanoparticles. An unexpected red shift of the PL spectra has been observed together with the decrease of the PL as the concentration of additional ions was increased, at least for light ions. This red shift does not result from a modification of the size distribution of nc-Si or from the optical properties of the host matrix. We rather believe that during the post-annealing, the additional ions are expelled from the nc-Si so that they reside either at the interface between the nc-Si and the SiO$_2$ matrix or deeper in the host matrix. One of the carriers of the photogenerated electron-hole pair can be trapped by the additional ions. The free carrier remaining in the nc-Si core then quenches any further optical recombination by a non-radiative process. The red shift can also be explained by the fact that the incorporation of additional atoms into the nc-Si core, either by substitution of Si atoms or by insertion into lattice interstices, induces local modifications of the lattice structure resulting in a decrease of the band gap energy.

Applying a second post-annealing at 1100 °C, the PL is significantly increased, and, in some cases, it is even slightly enhanced compared to the original PL of pure nc-Si/SiO$_2$ systems. The enhancement of the PL could be due to the improvement of the crystallization and/or the passivation of the nc-Si that could be induced by the impurities. The PL intensity is unexpectedly strong for atomic concentrations of the impurities above ~10^{20} at./cm^3, which indicates that, during the post-annealing, either the additional atoms are expelled from the nc-Si core or they do not act as defect.

5.2. Exciton-erbium energy transfer in nc-Si/SiO$_2$ containing Er

Erbium-doped silica glass is employed as an optical amplifier medium in telecommunication technology. The Er^{3+} ions present in the glass matrix exhibit two sharp emission lines due to intra-4f shell electronic transitions at 0.982 and 1.536 μm, corresponding to the $^4I_{11/2} \rightarrow {}^4I_{15/2}$ and $^4I_{13/2} \rightarrow {}^4I_{15/2}$ transitions, respectively.[177] Fujii *et al.*[17] demonstrated that the presence of nc-Si considerably enhanced the effective absorption cross section of Er^{3+} ions by 2 to 4 orders of magnitude because of the large absorption cross section of nc-Si. Because of the promising applications of such systems, in which nc-Si acts as photosensitizer for the emission line of Er^{3+} ions at 1.536 μm, a standard wavelength in telecommunication, great efforts have been devoted to the understanding of the interaction between nc-Si and Er^{3+} ions. Incorporating Er into our nc-Si/SiO$_2$ systems and taking benefit of the Er^{3+} emission, provides a new approach to understand the quenching mechanisms caused by the incorporation of additional ions.

5.2.1. Photoluminescence

Similar experiments as described before have been carried out by post-implanting Er$^+$ ions into luminescent nc-Si/SiO$_2$ samples, which were prepared by implantation of 100-keV Si$^+$ ions into fused silica windows with an ion fluence of 1×10^{17} ions/cm^2. The samples were subsequently annealed at 1100 °C. The nc-Si/SiO$_2$ samples were implanted with 446-keV Er$^+$ ions with various ion fluences, resulting in an Er-peak concentration ranging from 3.9×10^{18} to 3.9×10^{20} at./cm^3. Figure 5.10.a shows the effect of Er-incorporation into our nc-Si/SiO$_2$ systems on the PL spectra for various Er$^+$ ion fluences. In the Vis-NIR region, the sample containing no Er exhibits a broad luminescence peaking at about 875 nm originating from the radiative recombination of excitons confined within the nc-Si of an average size of about 4.2 nm in diameter. As the Er concentration increases, the intensity of the peak decreases rapidly. It should be noted that, in spite of the drastic change in intensity, the PL peak positions do not significantly vary with the Er concentration in contrast to the progressive red shifts of

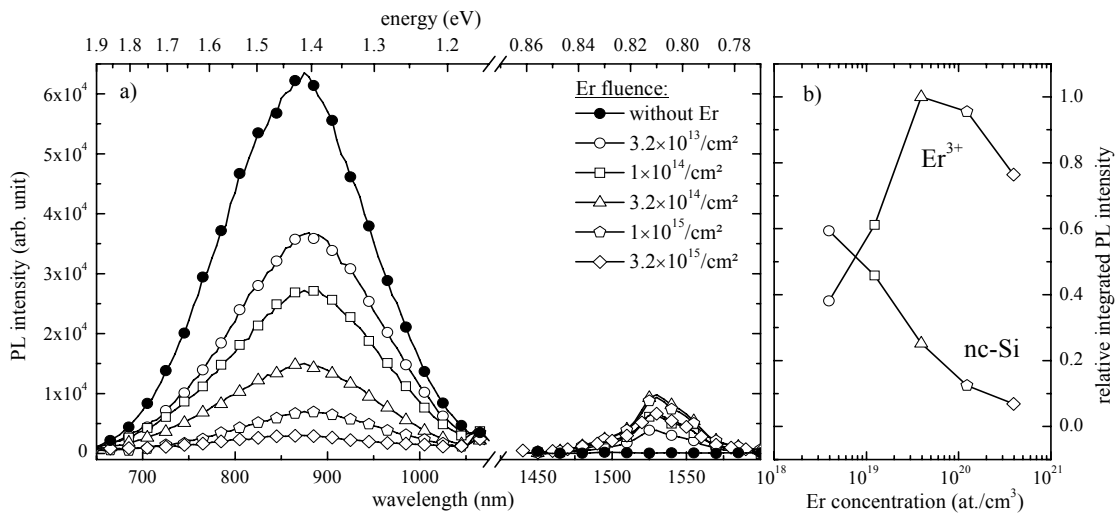Fig. 5.10. a) PL spectra of nc-Si/SiO$_2$ systems post-implanted with Er$^+$ ions with ion fluences ranging from 0 to 3.2×10^{15} ions/cm^2. All six samples were subsequently post-annealed at 900 °C in N$_2$ (the sample containing no Er included) during one hour. b) Integrated PL intensity originating from the nc-Si and from the 1.54-μm Er^{3+} emission as a function of Er concentration.

the PL spectra observed in the case of Mg (see Sec. 5.1.1.1.) and Ca incorporations (see Sec. 5.1.2.) as the concentration of Mg or Ca was increased. This absence of a red shift could be explained by the implantation profile of Er (see Fig. 5.9) which is narrower than the one of Si. Therefore, the small silicon precipitates localized in the wings of the nc-Si distribution are less affected by the presence of Er, leading to a counterbalancing blue shift of the PL spectra since, according to the quantum confinement model, shorter emission wavelengths are characteristic of smaller nanocrystals.

For the samples containing Er, another peak at 1.54 μm is seen in the infrared region, in spite of the very small amount of Er. This peak becomes more intense as the Er-peak concentration increases from 3.9×10^{18} to 3.9×10^{19} at./cm^3 and decreases in intensity for Er concentrations above the latter value. In our samples, the concentration of Er is too small to observe the Er^{3+} emission line at 0.98 μm.[17, 18] Although it is not shown here, the intensity of the 1.54-μm peak is more than 70 times stronger than that of SiO$_2$ not containing nc-Si and containing Er implanted with an ion fluence of 3×10^{15} ions/cm^2, which gives evidence that nc-Si enhances the 1.54-μm PL emission of Er^{3+}. The enhancement of the Er^{3+} emission suggests that energy is transferred from the nc-Si to the Er^{3+} ions. First, the excitation light is absorbed mainly by the nc-Si, generating electron-hole pairs within the nc-Si. Excitons can recombine radiatively, emitting photons with an energy that depends on the nc-Si size. However, excitons can also interact with Er^{3+} ions located in the nanoparticles or residing closed to the nc-Si and transfer their energy to the Er^{3+} ions. Two different energy transfer processes (slow and fast) coexist in such nc-Si/SiO$_2$ systems containing Er.[19, 118, 178] The fast process (~10 ns) concerns the emission of Er^{3+} ions located in the nc-Si or at a short distance from the nanoparticle surface of about 1 - 2 nm,[18, 19] and is essentially the same as in Er-doped bulk silicon. An exciton is trapped by an Er^{3+} ion and then the recombination energy is transferred to the first excited state of Er^{3+} ion ($^4I_{13/2}$) by an Auger-like process. The slow process (a few μs) concerns the emission of Er^{3+} ions located deeper in the host SiO$_2$ matrix.

In our samples, the PL intensity of the Er^{3+} emission line at 1.54 μm is, for the same Er concentration and with respect to the intensity of the original PL of nc-Si, weaker than in previous studies.[17, 19, 110] In these studies, the residual 0.6-1 μm PL in the nc-Si/SiO$_2$ systems containing Er is believed to originate mainly from nc-Si's that are not or only weakly coupled with Er^{3+} ions.[18] Therefore, because of the apparently less efficient coupling between the nc-Si and Er^{3+} ions and the quenching of the PL of nc-Si observed in our nc-Si/SiO$_2$ samples, although post-annealed at 900 °C, we believe that the PL of nc-Si is strongly affected by the presence of residual defects caused by the post-implantation of Er$^+$ ions, and thus, that only a small portion of optically active Er^{3+} ions is coupled to a nc-Si.

5.2.2. Time-resolved photoluminescence spectroscopy

Figure 5.11 shows the effect of Er-incorporation on the PL originating from nc-Si in the time-resolved domain. As the concentration of Er increases, the lifetime becomes shorter. In previous PL studies of similar samples,[179] which, however, were implanted with lower Er$^+$ ion fluences, the nc-Si PL decay time was reported to be insensitive to the concentration of
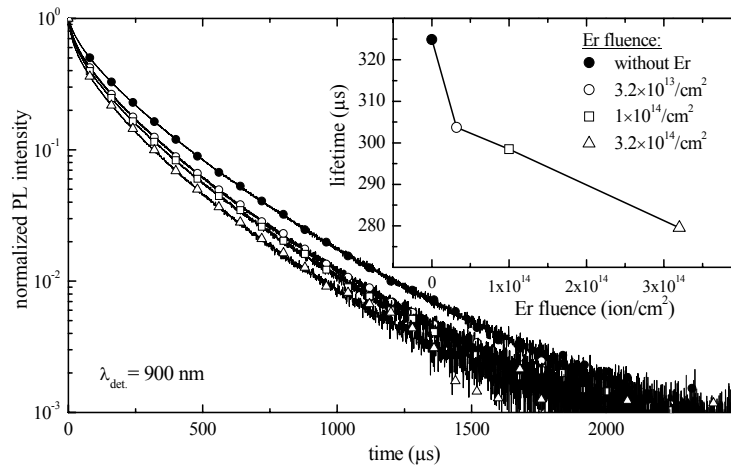
Fig. 5.11. PL decay curves of nc-Si/SiO$_2$ systems post-implanted with Er$^+$ ions with ion fluences ranging from 0 to 3.2×10^{14} ions/cm^2 and subsequently annealed at 900 °C. The inset shows the decay lifetimes of the respective samples as a function of the Er$^+$ ion fluences. The lifetimes were evaluated by fitting log-normal lifetime distributions to the measured data using the maximum entropy method of data analysis.[140]

Er, while, paradoxically, the Er-incorporation was found to reduce the nc-Si luminescence. Kik and Polman[18] suggested that, since the transfer time is rather fast (a few µs), all observed exciton luminescence originates mainly from nc-Si which are not coupled with Er^{3+} ions. However, a decay shortening similar to ours has also been observed elsewhere for higher Er concentrations,[19, 178] suggesting that the shortening of the lifetime is due to the emergence of new non-radiative recombination paths in our nc-Si/SiO$_2$ systems, like, for instance, defects at the nanoparticle surface. Therefore, the decrease of the Er^{3+} PL emission that we observed for concentrations of Er above 3.9×10^{19} at./cm^3 (see Fig. 5.10.b) can thus be explained by the competition between the energy transfer mechanism and the non-radiative transition through defects.

5.2.3. Conclusion

In our nc-Si/SiO$_2$ systems into which Er has been incorporated, the quenching of the PL originating from nc-Si results principally from defects induced by the Er-implantation. Applying a post-annealing at 900 °C seems not sufficient to recrystallize and/or passivate the damaged nc-Si. This picture is supported by the shortening of the PL decay observed as the Er concentration increases. However, the Er^{3+} emission line at 1.54 µm, apparently enhanced by the presence of nc-Si, gives evidence that a fraction of the nc-Si are transferring their energy to Er^{3+} ions. The greater part of Er^{3+} ions is believed to be localized at the nanoparticle surface or in the host SiO$_2$ matrix since the solubility of Er in crystalline silicon is about 2 orders of magnitude lower than in SiO$_2$.[19] Therefore, it is evident that the quenching mechanism of nc-Si embedded in a host matrix is not only due to dangling bonds at the nanoparticles' surface and/or to defects in the lattice structure induced by the presence of additional atomic elements, but also to the presence of foreign ions in the host matrix.

5.3. Ge and alloy Si$_{1-x}$Ge$_x$ nanocrystals embedded in SiO$_2$

Great efforts have been devoted to the synthesis and PL properties of nanometer-sized Si and Ge crystals (nc-Si and nc-Ge) due to their potential applications in optoelectronics. It has been clearly experimentally demonstrated that the PL energy of nc-Si is tunable from the bulk band gap to the visible region by decreasing the nanoparticle size (see Chap. 4). This indicates that the PL is due to the recombination of excitons confined within the nanocrystal's volume, as predicted by theoretical calculations.[5] Such size dependence of the PL has also been observed for nc-Ge; however, only for samples produced by a cosputtering technique.[180] And, in spite of the fact that the experimental results are not in perfect accordance with theoretical calculations of the size dependence of the energy band gap,[144] the observed NIR photoluminescence is believed to originate from quantum-confined states in nc-Ge.

Takeoka *et al.*[125] have experimentally demonstrated that in Si$_{1-x}$Ge$_x$ alloy nanocrystals the PL energy changes from the band gap of nc-Si to that of nc-Ge as the Ge concentration is increased. Their samples were however synthesized by a cosputtering technique. The next sections deal with the production of nc-Ge by ion implantation, as well as the synthesis of nc-Si$_{1-x}$Ge$_x$, either by our incorporation procedure into the nc-Si/SiO$_2$ systems, as reported in the previous sections, or by Si and Ge coimplantation into fused silica windows. The optical properties of the nanoparticles are investigated by PL and Raman spectroscopy.

5.3.1. Photoluminescence

5.3.1.1. Photoluminescence centers in fused silica windows containing nc-Ge

Figure 5.12 shows the PL spectra obtained from fused silica windows implanted with Ge$^+$ ions with various ion fluences followed by an annealing at 1100 °C. Broad peaks of green luminescence are observed around 540 nm for all the samples. As the Ge$^+$ ion fluence increases from 1×10^{16} to 5×10^{16} ions/cm^2, the PL intensity increases progressively, and for the highest ion fluence a sharp peak of violet luminescence appears at 410 nm (3.02 eV). This violet luminescence is intense and visible to the naked eye. It was previously observed in various SiO$_2$ substrates implanted with Ge at a position varying between 2.7 and 3.2 eV, and its origin is attributed to germanium oxygen deficient centers.[82] Rebohle *et al.*,[181] who ob-
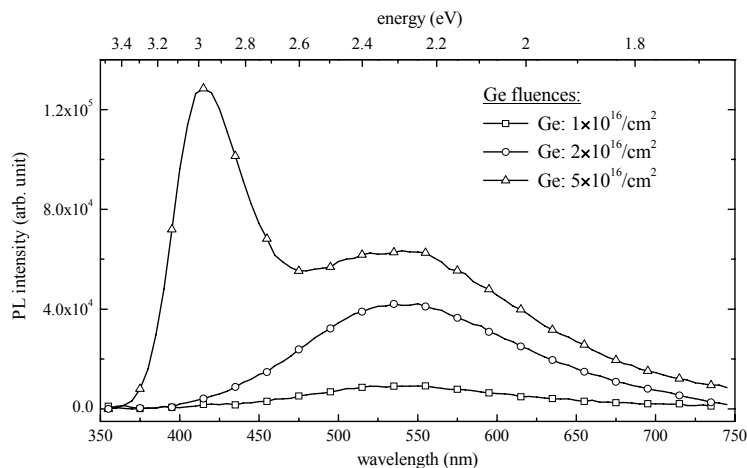

Fig. 5.12. PL spectra of fused silica windows implanted with 208-keV Ge$^+$ ions with three different ion fluences and subsequently annealed at 1100 °C in N$_2$ during one hour. The samples were excited with the 266 nm fourth harmonic line of a Nd:YAG laser with an excitation fluence of 250 μJ/cm^2.

served in their samples three distinct violet PL bands peaking at 3.39, 3.05, and 2.72 eV, proposed an explanation for the variation of the PL peak position originating from germanium oxygen deficient centers. They suggested that one or both Si atoms of a neutral oxygen vacancy defect $\equiv$ Si-Si$\equiv$, a well-known luminescence center in quartz peaking at 2.7 eV (see Sec. 2.2.2.4.), is/are substituted by Ge atoms forming a $\equiv$ Si-Ge $\equiv$ or $\equiv$ Ge-Ge$\equiv$ center, emitting at 3.05 and 3.39 eV, respectively.

The green broad PL band has been detected in samples synthesized by sputtering Ge in combination with SiO$_2$ and followed by an annealing at high temperature, where the presence of nc-Ge has been detected either by TEM, Raman spectroscopy, and X-ray photoelectron spectroscopy,[182] or only by TEM.[180, 183] In spite of the fact that the authors have observed that the green-yellow PL peak position, in terms of emission energy, decreases with the nanoparticles size, this behavior cannot be explained by the quantum confinement model. Theoretical calculations by Niquet *et al.*[144] have predicted that radiative recombination of quantum-confined excitons in nc-Ge occurs in the Vis-NIR region. Size dependence of the PL in the Vis-NIR region has previously been observed for nc-Ge embedded in SiO$_2$ by Takeoka *et al.*[180] However, their results did not completely agree with the theoretical predictions and Niquet *et al.* concluded that the near-infrared PL originates from deep traps in the band gap of nc-Ge. However, one can also suggest that in these systems the band gap of nc-Ge is affected by the host matrix.

The green broad PL band seen in Fig. 5.12 has also been detected in samples synthesized by a similar procedure consisting in Ge implantation into quartz matrices followed by an annealing at high temperature, where the presence of nc-Ge was manifested either by Raman spectroscopy,[184] X-ray diffraction,[185] or TEM.[187] The presence of nc-Ge in our samples was also detected by optical transmission spectroscopy (see Sec. 4.2.1.2) and Raman spectroscopy (not shown in this thesis), however only for Ge ion fluences above 1×10^{17} ions/cm^2. The green luminescence was found to vary with the synthesis conditions from 1.9 to 2.31 eV,[184, 185, 186, 187] However, it is inconsistent with the quantum confinement model of excitonic recombination in nc-Ge. Kachurin *et al.*[184] have demonstrated that the green PL disappears when an annealing above 1200 °C is applied, and, Min *et al.*[186] have shown that this PL can be drastically quenched by implanting the sample with deuterium which is known to passivate electronic defects in semiconductors, demonstrating that the green PL is due to defects in the samples. It seems that the Ge-SiO$_2$ boundary does not allow strong luminescence from quantum-confined states in nc-Ge systems, and other PL peaks are related to defects in such systems. Takeoka *et al.* have suggested that the green PL originates from defects at the interface between nc-Ge and the surrounding matrix, whereas Gorshkov *et al.*[49] have attributed this PL to atomic chains of Si-Si-Si, Ge-Si-Si, and Ge-Si-Ge types. However, Kartopu *et al.*[188] have recently shown that defects in GeO$_2$ or Ge-O bonded materials exhibit light in the same energy domain, suggesting that this PL is definitely not related to nc-Ge.

5.3.1.2. Si and Ge coimplantation into SiO$_2$

Figure 5.13 shows the PL of fused silica samples co-implanted with Si$^+$ and Ge$^+$ ions (*open symbols*) followed by an annealing at 1100 °C. The two ion energies were chosen in order to provide the same penetration depth of ~150 nm for both ions. In the UV-visible region ranging from 350 to 650 nm, one can clearly observe a green luminescence peaking at around 525 nm for a Ge$^+$ ion fluence of 1×10^{16} ions/cm^2 and the appearance of a violet shoulder when the Ge$^+$ ion fluence is increased to 5×10^{16} ions/cm^2. These two bands were already observed in Ge-implanted samples, and they were attributed to defects in nc-Ge/SiO$_2$ systems (see previous section). However, in contrast to samples implanted only with Ge$^+$ ions (see Fig 5.12), the intensity of the green PL was found to increase with increasing Ge$^+$ ion fluence, and the violet PL peak was relatively stronger. This implies that the presence of excess Si affects the concentration of luminescent centers where Ge is apparently involved. In the Vis-NIR region, one can clearly see from the sample implanted only with Si$^+$ ions a strong luminescence peaking at around 850 nm (*full symbols*) which originates from the radiative recombination of quantum-confined excitons in nc-Si (see Chap. 4). As the Ge$^+$ ion fluence increases, the PL from nc-Si progressively decreases and, besides, all the PL spectra are slightly shifted to longer wavelengths.

In order to further investigate the Vis-NIR PL of such samples co-implanted with Si$^+$ and Ge$^+$ ions, a new set of fused silica windows has been coimplanted with Si$^+$ ions with an ion fluence of 1×10^{17} ions/cm^2 and with Ge$^+$ ion fluences ranging from 1×10^{12} to 1×10^{16} ions/cm^2. The resulting PL spectra are shown in Fig 5.14.a. Again, the PL spectrum peaking at 825 nm of the sample into which no Ge$^+$ ions has been implanted (*full symbols*) is due to the presence of nc-Si. The PL intensity of the 825 nm peak decreases progressively with increasing Ge$^+$ ion fluence. At low fluence ($\leq 1 \times 10^{15}$ ions/cm^2) the effect is rather small, but when the Ge$^+$ ion fluence is further increased, the PL of nc-Si is significantly decreased. For a Ge$^+$ ion fluence of 1×10^{16} ions/cm^2 the integrated PL intensity is 5 times weaker than in the sample without Ge. Furthermore, at this Ge$^+$ ion fluence, the PL peak is shifted to the red by about 35 nm with respect to the sample into which only Si$^+$ ions were

Fig. 5.13. PL spectra of fused silica windows coimplanted with 100-keV Si$^+$ ions with an ion fluences of 1×10^{17} ions/cm^2 and with 208-keV Ge$^+$ ions with two different ion fluences. All samples were subsequently annealed at 1100 °C in flowing N$_2$ during one hour. The samples were excited with the 266 nm fourth harmonic line of a Nd:YAG laser with a fluence of 130 μJ/cm^2.
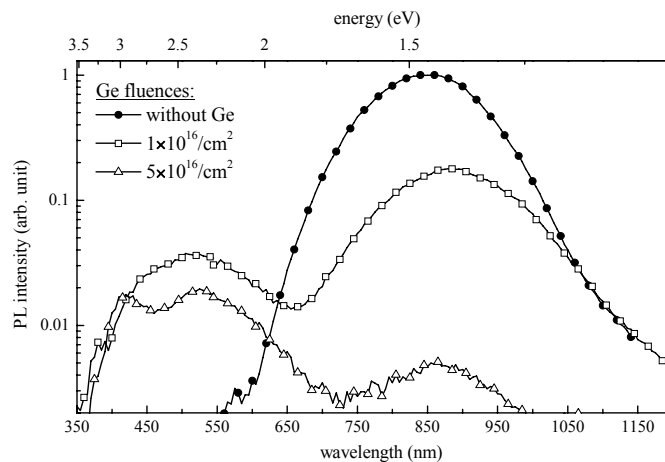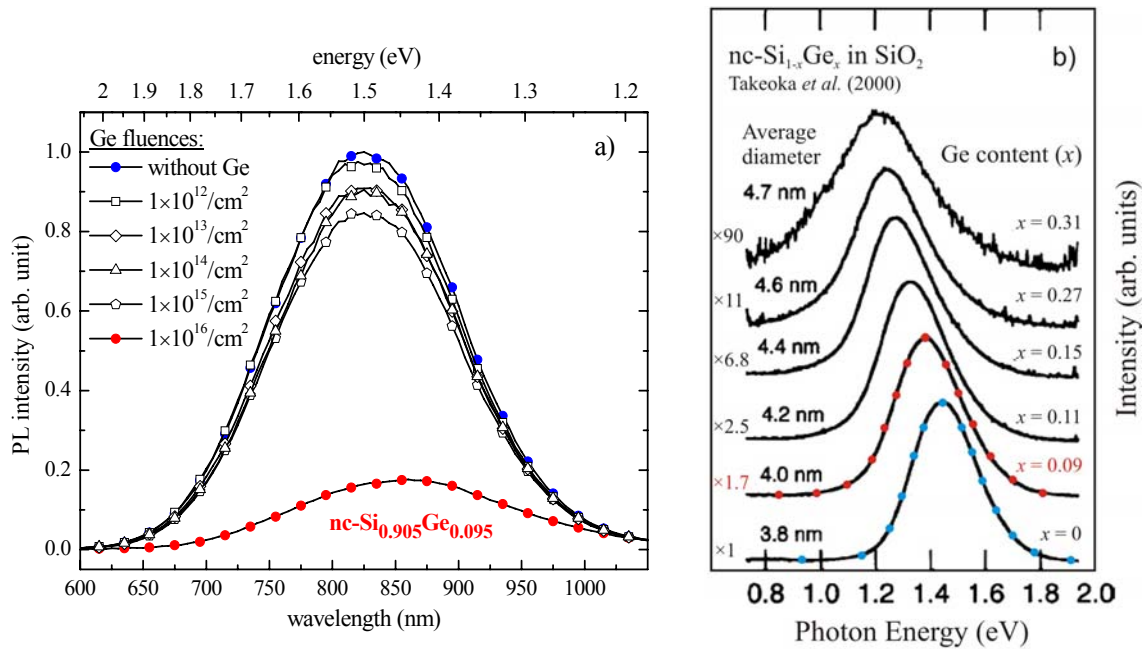
Fig. 5.14. a) PL spectra of fused silica windows coimplanted with 100-keV Si$^+$ ions with an ion flu-ences of 1×10^{17} ions/cm^2 and with 208-keV Ge$^+$ ions with five different ion fluences. All samples were subsequently annealed at 1100 °C in flowing N$_2$ during one hour. The samples were excited with the 266 nm fourth harmonic line of a Nd:YAG laser with an excitation fluence of 130 μJ/cm^2. b) PL spectra of nc-Si$_{1-x}$Ge$_x$ embedded in SiO$_2$ with various Ge contents, according to Takeoka *et al.*[125] The PL spectra are normalized to yield equal maximum intensity and the scaling factors for the normalization are displayed in the figure. The excitation source was the 457.9 nm line of an Ar-ion laser. And the excitation power density was about 1 W/cm^2.

implanted. Besides, it is sensitively broadened. The FWHM of the PL spectra is about 200 nm in the latter sample whereas it is about 170 nm for the pure nc-Si/SiO$_2$ system.

Takeoka *et al.*[125] produced nc-Si$_{1-x}$Ge$_x$ alloy nanocrystals embedded in SiO$_2$ matrices by sputtering Si in combination with Ge and SiO$_2$. Their samples were annealed at 1100 °C in N$_2$. The existence of nc-Si$_{1-x}$Ge$_x$ was supported by the spacing of the lattice fringes of the nanocrystals imaged by HRTEM which was between that of Si and Ge bulk crystals. More-over, they found the signatures of Si-Si, Ge-Ge, and Si-Ge vibrations in their Raman spectra indicating that they synthesized nc-Si$_{1-x}$Ge$_x$. We show the PL spectra in Fig. 5.14.b of their nc-Si$_{1-x}$Ge$_x$/SiO$_2$ systems with various Ge content x. Interestingly, their measurements re-vealed a qualitatively similar decrease, broadening, and red shift of the spectra with increasing Ge concentration suggesting that we also synthesized alloy nanocrystals with our coimplanta-tion procedure.

In this case, the coimplantation of Si and Ge into our fused silica windows with the two Si$^+$ and Ge$^+$ ion fluences of 1×10^{17} and 1×10^{16} ions/cm^2, respectively, would result in the formation of nc-Si$_{0.905}$Ge$_{0.095}$ alloy nanocrystals. We estimated the Ge content x by the ratio between the Si and Ge peak concentrations obtained by simulation using the SRIM-2003 software. It is interesting to compare the PL spectra of our pure nc-Si sample (*blue*) and our nc-Si$_{0.905}$Ge$_{0.095}$ sample (*red*) with the ones obtained by Takeoka *et al.* for the same Ge con-tents. They are depicted in the same colors. The red shift reported for their nc-Si$_{0.91}$Ge$_{0.09}$ is comparable (~35 nm) with the one observed in our nc-Si$_{0.905}$Ge$_{0.095}$ sample. However, the PL intensity is more decreased in our sample (÷5) than in their previous work (÷1.7) which is

probably related to the different synthesis methods. This would explain why we did not observe Vis-NIR photoluminescence originating from our samples at higher Ge$^+$ ion fluences.

Takeoka *et al.* suggested that the observed red shift as the Ge concentration increased reflected the narrowing of the band gap of nc-Si by the Si-Ge alloying. The band-gap energy of nc-Si$_{1-x}$Ge$_x$ is expected to change continuously from the wider band gap of nc-Si to the smaller one of nc-Ge with increasing *x*. However, Delerue *et al.*[189] predicted an increase of the PL efficiency with the increase of the Ge content.

The PL quenching of the samples produced by Takeoka *et al.* was explained by Toshikiyo *et al.*[190] They studied the Si and Ge dangling bonds at the interface between nc-Si$_{1-x}$Ge$_x$ and the host SiO$_2$ matrix (Si and Ge *Pb* centers, see Sec. 2.2.2.3.) by electron spin resonance. As the Ge content increased, the signal attributed to Ge *Pb* centers increased, while that from Si *Pb* centers was nearly independent of the Ge concentration. Therefore, they could conclude from the observed correlation between the amount of Ge *Pb* centers and the PL intensity that the PL quenching resulted from Ge dangling bonds which are efficient non-radiative recombination centers.

Finally, the strong resemblance of the behavior of the PL spectra with various Ge contents in the present study with the one reported elsewhere[125, 191] suggests the presence of Si$_{1-x}$Ge$_x$ alloy nanocrystals in our samples.

5.3.1.3. Ge incorporation into nc-Si/SiO$_2$

Figure 5.15.a shows the effect of the incorporation of Ge into our nc-Si/SiO$_2$ systems on the PL spectra originating from the nc-Si. The PL completely disappeared after implanting the samples with 208-keV Ge$^+$ ions suggesting that the nc-Si were seriously damaged by the Ge$^+$ ion irradiation. Carrying out a post-annealing at 900 °C for one hour in flowing N$_2$, partly recovered the original PL of the nc-Si, but only for the lowest Ge$^+$ ion fluences (*open symbols*), as can be seen in Fig. 5.15.a. For the Ge$^+$ ion fluence of 1×10^{15} ions/cm^2, the PL peak decreases and shifts to longer wavelengths in the same way as reported for the Mg- or Ca-incorporation (see Sec. 5.1.1.1. and 5.1.1.2.). For the Ge$^+$ ion fluence of 4×10^{15} ions/cm^2, the spectrum is seriously quenched and seems to shift to the blue. However, since the PL intensity is rather weak, this luminescence could also originate from defects in the host matrix and not from nc-Si. Applying a second annealing at 1100 °C (*full symbols*), the PL intensity of the pure nc-Si/SiO$_2$ sample (*full circles*) slightly decreases and the PL spectrum is slightly shifted to the red. This could be explained by the growth of nc-Si since longer emission wavelength is characteristic of larger nanocrystals, according to the quantum confinement model, and, furthermore, it has been demonstrated that for nanoparticles larger than 3 nm in diameter, *i.e.* that exhibit PL above 800 nm, the PL yield decreases with the size.[160] The PL intensity of nc-Si/SiO$_2$ samples into which Ge has been incorporated is substantially enhanced with the second annealing. This is probably due to the reduction of the damages caused by the Ge post-implantation. The red shift is also less pronounced after the second post annealing. The behavior of the PL spectra of nc-Si/SiO$_2$ systems implanted with Ge with respect to the an-
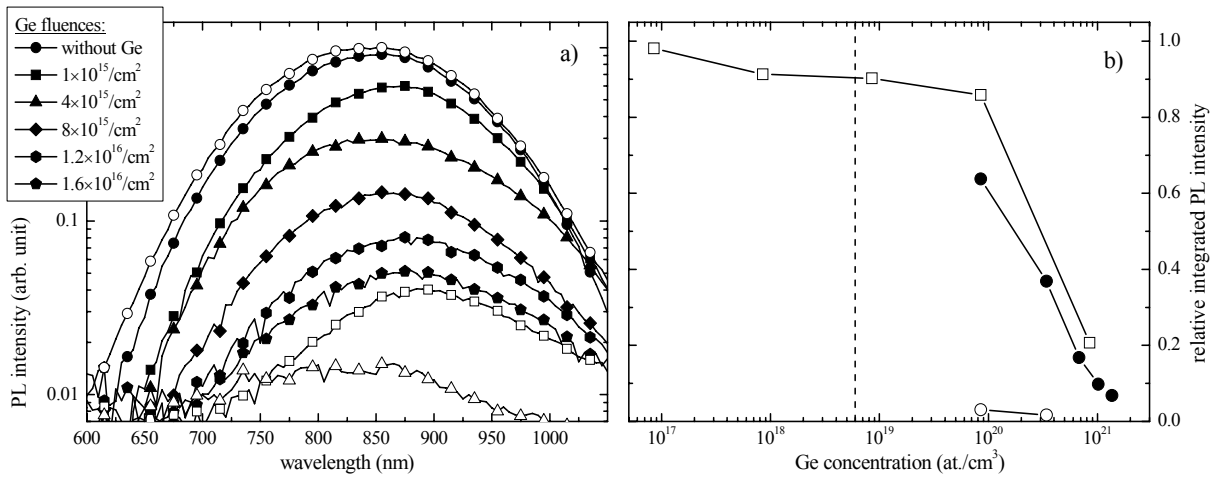
Fig. 5.15. a) PL spectra of nc-Si/SiO$_2$ systems post-implanted with 208-keV Ge$^+$ ions at different ion fluences and followed by a first annealing at 900°C (*open symbols)* and a second one at 1100 °C (*full symbols*). b) Effect of Ge concentration in Si-Ge systems on the integrated PL intensity relative to the sample into which only Si$^+$ ions were implanted. The Si-Ge systems were produced either by coimplantation of Si$^+$ and Ge$^+$ ions (*squares*) or by Ge post-implantation into nc-Si/SiO$_2$ systems followed by a first post-annealing at 900 °C (*open circles*) and a second one at 1100 °C (*full circles*). The vertical dashed line represents the average concentration of nc-Si in pure systems.

nealing temperature is similar as the one previously reported for Mg, Ca and Na (see Sec. 5.1.1.).

Figure 5.15.b shows the integrated PL intensity as a function of the Ge concentration comparing coimplantation and incorporation method. The PL spectra of the sample produced by coimplantation are displayed in Fig. 5.14.a. Surprisingly, as it can be seen, the coimplantation procedure (*open squares*) quenches the luminescence to a lesser extent than the incorporation procedure (*full symbols*) with a first post-annealing at 900 °C and a second one at 1100 °C, although the nc-Si's were previously formed before the Ge$^+$ ion post-implantation into the incorporation procedure. This can be explained by the following picture. In the incorporation procedure, the nc-Si$_{1-x}$Ge$_x$ are formed from the residual small Si aggregates, which remain after the Ge$^+$ ion post-implantation, acting as agglomeration nuclei during the growth process in the post-annealing, thus, we can expect that the concentration of Ge increases with the distance from the center of the alloy nc-Si$_{1-x}$Ge$_x$. On the other hand, we expect that, in the coimplantation procedure, the Ge atoms are randomly distributed in the nc-Si$_{1-x}$Ge$_x$. Therefore, in the incorporation procedure, we believe that the Ge dangling bonds are comparatively more present at the interface between nc-Si$_{1-x}$Ge$_x$ and the host SiO$_2$ matrix than in the coimplantation procedure, resulting in a more effective quenching of the PL. Furthermore, the PL quenching starts at Ge atom concentrations one order of magnitude higher than the nc-Si concentration (*dashed vertical line*) where we do not expect to observe so much PL originating from pure nc-Si considering one Ge atom as a defect that inhibits any radiative excitonic recombination. This implies that PL would originate from Si$_{1-x}$Ge$_x$ alloy nanocrystals. Finally, we believe that we formed nc-Si$_{1-x}$Ge$_x$/SiO$_2$ in some cases, by the incorporation and coimplantation method.

5.3.2. Time-resolved photoluminescence

Figure 5.16.a shows the PL decay curves recorded at various energies of two fused silica windows prepared differently. One sample was implanted with Si^+ ions and the second was coimplanted with Si^+ and Ge^+ ions. The Si^+ and Ge^+ ion fluences were 1×10^{17} and 1×10^{16} ions/cm^2, respectively. Implantations were followed by an annealing at 1100 °C in flowing N_2, leading to the formation of pure nc-Si and nc-Si$_{0.905}$Ge$_{0.095}$, respectively. The respective PL spectra are shown in Fig. 5.14.a. As can be seen in Fig 5.16.a, we observed a shortening of the PL lifetimes with the presence of Ge at various detection energies. For instance, at 1.37 eV, the lifetime is about 250 µs for the pure nc-Si/SiO₂ sample, while for the sample containing Ge it is about 130 µs.

In the time-resolved domain, the behavior of the decay curves with the Ge content is also comparable with the work of Takeoka *et al.*[125] They prepared similar samples by a co-sputtering method, where nc-Si$_{1-x}$Ge$_x$ alloy nanocrystals have been identified. Figure 5.16.b shows the PL decay curves of these samples with various Ge content. The respective PL spectra are shown in Fig. 5.14.b. However, in their work, the decay curves were taken at the maximum of each PL spectrum in the spectral domain. Therefore, for a proper comparison, we must consider our decay curves at 1.45 eV (*blue triangles*) for the pure nc-Si/SiO₂ systems and at 1.37 eV (*red pentagons*) for the nc-Si$_{0.905}$Ge$_{0.095}$/SiO₂ systems. In spite of the fact that their lifetimes are different (two different excitation wavelengths were used, two different evaluation methods of the lifetimes were employed, and the lifetimes depend on the quality of the sample), the ratios between the lifetime of the sample containing Ge and the lifetime of
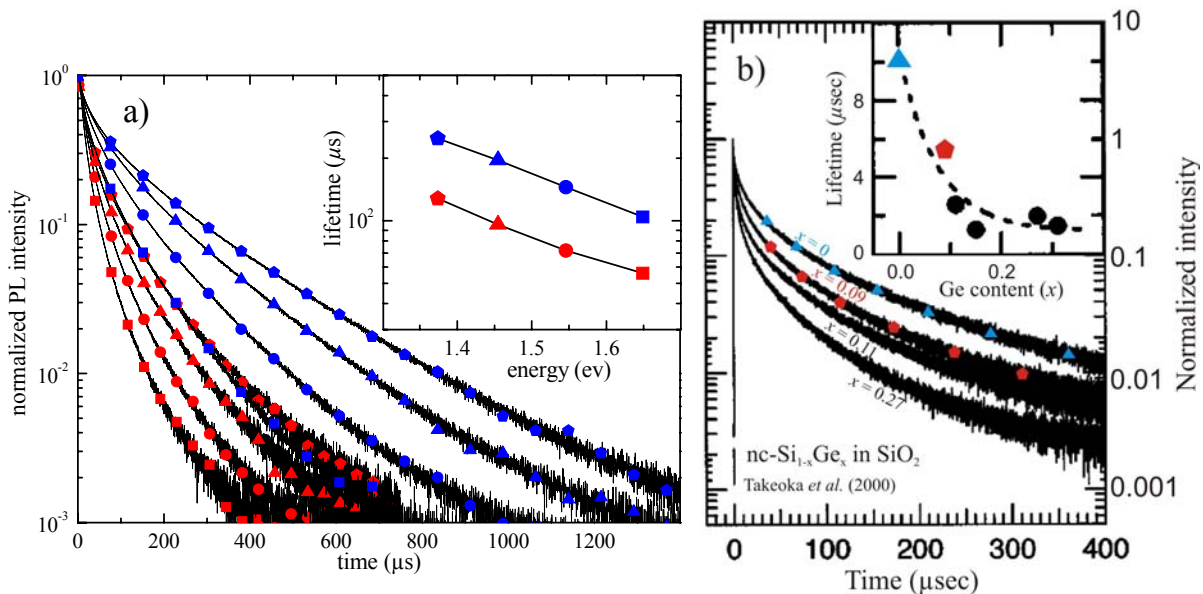
Fig. 5.16. a) PL decay curves of a fused silica window implanted with Si^+ ions (*blue symbols*) and of second one coimplanted with Si^+ and Ge^+ ions (*red symbols*). The decay curves were recorded at 1.65 (*squares*), 1.54 (*circles*), 1.45 (*triangles*) and 1.37 eV (*pentagons*). The inset shows the lifetime dependence on the emission energy for the two respective samples. The PL lifetimes were evaluated by fitting log-normal lifetime distributions to the measured data using the maximum entropy method of data analysis.[140] The samples were excited with the 266 nm fourth harmonic line of a Nd:YAG laser with an excitation fluence of 130 µJ/cm^2. b) PL decay curves of nc-Si$_{1-x}$Ge$_x$ embedded in SiO₂ with various Ge contents, according to Takeoka *et al.*[125] The inset shows the lifetimes dependence on the Ge content. The authors defined the PL lifetime as the time at which the intensity becomes $1/e$ of the peak value. The excitation source was the 532 nm line of a Nd:YAG laser.

the pure nc-Si/SiO$_2$ sample (0.57) are relatively similar to ours (0.64).

Assuming that nc-Si$_{1-x}$Ge$_x$ are also formed in our sample, the shortening of the life-times, which has been theoretically predicted,[189, 192] can be explained by the reduction of the oscillator strength of the excitons caused by the Si-Ge alloying, as demonstrated by Weissker *et al.*[192] Besides, the authors showed that the lifetimes decrease with the Ge content in the alloy nanocrystals. However, it is also possible that the shortening of the lifetimes can be due to an increase of the non-radiative recombinations induced by defects caused by the presence of Ge within the nanocrystal core or at its surface. This latter mechanism explains also the observed quenching of the PL as the Ge concentration increases.

5.3.3. Temperature dependence of the photoluminescence

Figure 5.17.a shows the PL spectra of pure nc-Si/SiO$_2$ (*straight lines*) and alloy nc-Si$_{0.905}$Ge$_{0.095}$/SiO$_2$ systems (*dashed lines*) measured at various temperatures ranging from room temperature to 6.5 K. As the temperature falls, the PL intensity increases and reaches a maximum at 50 K. At the same time, the spectra become slightly narrower and shift progressively to the blue. It can be seen that the behavior of the PL spectra of these two samples as a function of the temperature is very similar. Indeed, the shift observed between the PL spectra of the two different samples is quite constant versus the temperature (Fig. 5.17.c), as well as the ratio between their integrated PL intensity (Fig. 5.17.b). Such comparable behavior suggests that the luminescence of both systems is governed by the same mechanism.

The temperature dependence of the PL of nc-Si can be explained by a model introduced by Calcott *et al.*[167] (see Sec. 4.2.2.2.). In this model, the ground exciton states are split by an energy Δ due to the exchange interaction between the electron and the hole (see inset Fig. 4.19.a). At low temperatures, the PL originates from the triplet state and the radiative lifetime is long, while at high temperatures the PL is dominated by the recombination of the thermally occupied singlet state, which has a shorter radiative lifetime. Figure 5.18.a shows
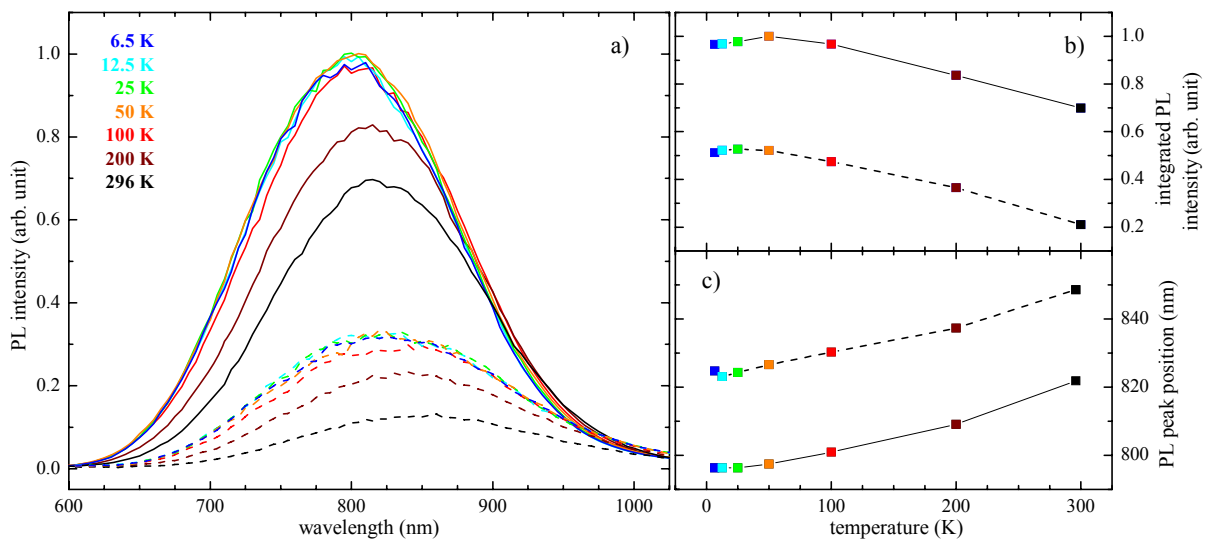
Fig. 5.17. a) Temperature dependence of the PL emission spectra of a fused silica window containing pure nc-Si (*dashed straight lines*) and a sample containing nc-Si$_{0.905}$Ge$_{0.095}$ (*straight lines*). The PL spectra of the pure (*blue*) and alloy (*red*) sample measured at room temperature are also shown in Fig 5.14.a. b) Temperature dependence of the integrated PL intensity of the two samples. c) Temperature dependence of the peak position of PL spectra of the two samples.
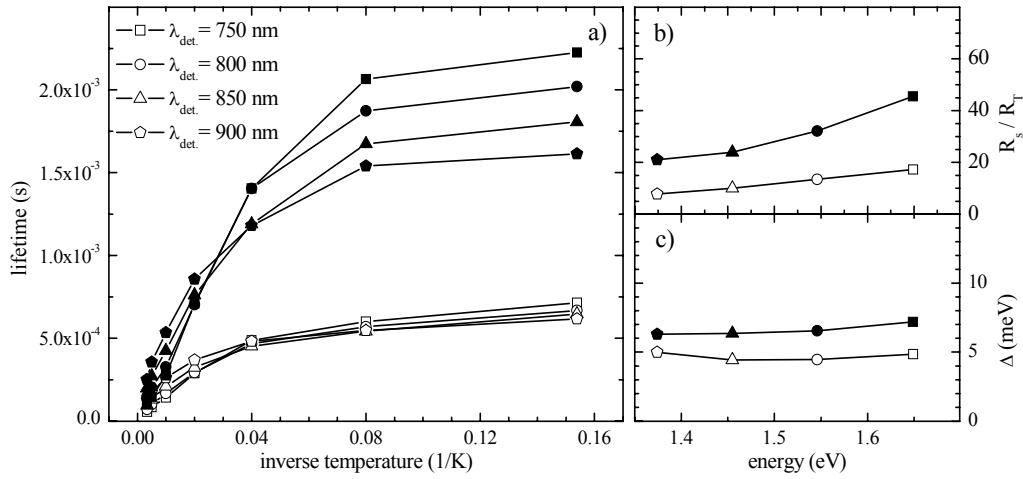
Fig. 5.18. a) Temperature dependence of the PL decay recorded at four emission wavelengths of a fused silica window containing pure nc-Si (*full symbols*) and of another window containing nc-Si$_{0.905}$Ge$_{0.095}$ (*open symbols*). b) Ratio of the singlet (R_S) and triplet (R_T) radiative decay rates of excitons for the two samples as a function of the emission energy. c) Exchange splitting energy as a function of emission energy for the two samples. The ratio R_S / R_T and values Δ were obtained by the fitting procedure reported in Sec. 4.2.2.2. according to the model proposed by Calcott *et al.*[167]

the effect of Ge on the temperature dependence of the PL lifetime of pure nc-Si and nc-Si$_{1-x}$Ge$_x$ embedded in SiO$_2$. One can clearly see that, for both samples, as the temperature decreases, the PL lifetimes increase progressively from the short to the long lifetime regime. The transition from fast to slow PL decay is more abrupt in the pure nc-Si/SiO$_2$ system (*full symbols*) than in the nc-Si$_{1-x}$Ge$_x$/SiO$_2$ system (*open symbols*) where it is more gradual. Furthermore, the PL decay shortening induced by the presence of Ge (see Sec. 5.3.2.) is relatively more pronounced at low temperatures than at room temperature. Similar results have been reported by Fujii *et al.*[191] where the Ge content, *x*, in their nc-Si$_{1-x}$Ge$_x$/SiO$_2$ system even reached values up to 0.27. Furthermore, they noticed that this change of the temperature dependence caused by the presence of Ge was more pronounced as the Ge content increased.

From the fitting procedure, we estimated the rates of the triplet and singlet states (R_T and R_S) and the splitting energies Δ for both systems at different detection energies ranging from 1.37 to 1.65 eV. The values of Δ and the ratios of R_S to R_T are plotted versus the detection energy in Fig. 5.18.c and Fig. 5.18.b, respectively. As expected from Fig. 5.18.a, the ratios of R_S to R_T and the values of Δ are lower in the nc-Si$_{1-x}$Ge$_x$/SiO$_2$ system than in pure nc-Si$_2$/SiO$_2$. One can basically assume that the energy splitting is related to the emission energy.[167]

5.3.4. Raman spectroscopy

Figure 5.19 shows the Raman spectra of nc-Si/SiO$_2$ systems into which various contents of Ge have been incorporated. A spectrum of an un-implanted sample is also shown for comparison. The PL spectra of these samples have been presented in Fig. 5.15.a. The Raman spectrum of pure nc-Si/SiO$_2$ is characterized by a resonance at around 520 cm^{-1} corresponding to the Si-Si vibration in crystalline silicon. This peak is attributed to the transverse optical phonon mode of crystalline silicon which confirms the presence of nc-Si in our samples (see Sec. 4.2.1.3.). As the Ge concentration increases, the peaks are shifted to lower frequencies.
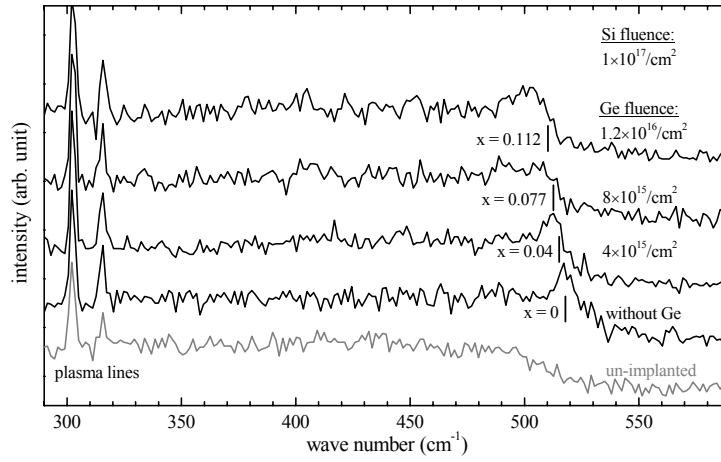
Fig. 5.19. Raman spectra of nc-Si/SiO$_2$ systems incorporated with Ge by ion implantation with various ion fluences followed by two subsequent annealings at 900 and 1100 °C in N$_2$ during one hour. The vertical bars indicate the positions of the Raman peaks following Eq. 1. The two peaks at 302.4 and 316.1 cm^{-1} are Ar$^+$-laser plasma lines originating from the excitation source.

This behavior has been reported by Takeoka *et al.*[125] when they increased the Ge content *x* in the composition of their nc-Si$_{1-x}$Ge$_x$/SiO$_2$ systems synthesized by cosputtering and subsequent annealing at 1100 °C. Therefore, we assume that we also produced nc-Si$_{1-x}$Ge$_x$ following our Ge incorporation method into nc-Si/SiO$_2$ systems. This behavior has also been observed in the Raman spectra (not shown here) of samples produced by coimplanting Si and Ge ions into fused silica resulting in the formation of nc-Si$_{1-x}$Ge$_x$ (see Sec. 5.3.1.2.). Furthermore, the strong resemblance between the PL spectra of our samples produced following our incorporation method and these of Takeoka *et al.* while the Ge concentration increases (see Sec. 5.3.1.3.) supports this assumption.

Takeoka *et al.* noticed that the Raman shift agreed well with that observed in bulk SiGe alloys with various Ge contents. In bulk SiGe alloy, the frequency of Si-Si modes varies almost linearly with the Ge composition *x*

$$\omega_{\text{Si-Si}}(x) = \omega_{\text{Si-Si}}(x{=}0) - 68x \text{ cm}^{-1}. \tag{1}$$

We have plotted the position of the Si-Si peaks (*vertical bars*) following this formula with respect to the sample containing pure nc-Si for all Ge$^+$ ion fluences. The composition of the nc-Si$_{1-x}$Ge$_x$ was determined by evaluating the maximum concentrations of Si and Ge in the host matrix resulting from the ion implantations using the SRIM-2003 software (see Sec. 5.1.5). In spite of the fact that the Raman signals are too noisy to determine the Si-Si peak positions (for *x* = 0.077, the Raman peak at 485 cm^{-1} assigned to SiO$_2$ is even more pronounced) it is clearly seen that the SiGe alloying can partly explain the red shift of the Raman peaks. The spectra are probably also affected by an increase of residual stress caused by the Ge implantation which induces a shift of the Raman peaks to lower frequencies. Regrettably, we find no signature of Si-Ge vibration at around 400 cm^{-1} in our Raman spectra. The Ge-Ge vibration occurs at around 300 cm^{-1} at the same position as one of the remaining plasma lines originating from the excitation source. However, the occurrence of the Si-Ge and Ge-Ge signals is expected to take place at higher Ge contents (*x* ≥ 0.15).[125, 193]

The origin of the observed red shift in our samples is complicated and does not only depend on the alloy composition, *x*, but also on the nanocrystal size, which is expected to in-

crease slightly with the Ge concentration. However, the strong resemblance of the Raman spectra with the studies of Takeoka *et al.*[125] where the presence of alloy Si$_{1-x}$Ge$_x$ nanocrystals has been demonstrated either by TEM,[125] or TEM and X-ray diffraction,[193] supports that our coimplantation or incorporation methods result in the synthesis of luminescent alloy nc-Si$_{1-x}$Ge$_x$.

5.3.5. Conclusion

Although it has been demonstrated by Raman spectroscopy and optical transmission spectroscopy that Ge implantation into fused silica windows followed by an annealing at high temperature results in the formation of nc-Ge, no PL created by the recombination of excitons confined in the nc-Ge volume could be identified. It seems that the samples prepared by this technique do not allow the radiative recombination of quantum-confined excitons and that the observed PL originates from luminescent defect centers in the nc-Ge/SiO$_2$ systems.

Strong resemblance with previous studies on the optical properties of nc-Si$_{1-x}$Ge$_x$/SiO$_2$ systems (photoluminescence,[191] time-resolved PL,[125] temperature dependence of PL,[191] and Raman spectroscopy[125, 193]) indicates that, with our incorporation or coimplantation method, we also synthesized nc-Si$_{1-x}$Ge$_x$ embedded in SiO$_2$. The differences between our two synthesis procedures appearing in the PL spectra could be explained by some nuances in the Ge distribution within the alloy nanoparticles. The red shift of the PL spectra with increasing Ge content x in the nc-Si$_{1-x}$Ge$_x$ could be due to the alloying, since it is expected that the band gap energy of nc-Si$_{1-x}$Ge$_x$ changes continuously from the band gap of nc-Si to the band gap of nc-Ge that is lower in energy.[5, 144] Calculations[189, 192] have predicted the shortening of the PL decay with increasing Ge content, however, it is reasonable to assume that the measured PL decays are also strongly affected by an increase of non-radiative recombinations caused by defects. This picture is supported by the decrease of the PL intensity observed as the Ge concentration increases, whereas the calculations have predicted the contrary.[189] Toshikiyo *et al.*,[190] have demonstrated that Ge atoms in the alloy nanocrystals provide new recombination channels induced by the presence of Ge dangling bonds at the interface between the nanocrystal and the host matrix which are responsible for the PL quenching.

In conclusion, for the first time, luminescent alloy nc-Si$_{1-x}$Ge$_x$ have been produced by ion implantation into fused silica and subsequent annealing at high temperature.

5.4.　Summary and outlook

In relation with the astrophysical aspect of this work, we have post-implanted into strongly luminescent nc-Si/SiO$_2$ systems various atomic elements that are present in natural silicates in order to simulate the conditions of silicates containing nc-Si. We observed that the ion beam irradiation quenches seriously the PL of nc-Si even at low ion fluences ($\leq 10^{12}$ ions/cm^2) forming structural damages in the nanocrystalline core. The PL originating from the nc-Si was partly recovered when a post-annealing at 900 °C was applied. However, we assume that the progressive quenching of the PL observed with increasing ion fluence from ~10^{12} to ~10^{15} ions/cm^2 is mainly due to residual structural defects caused by the ion

irradiation. This is supported by the fact that the incorporation of Si into our nc-Si/SiO$_2$ systems with the same post-annealing conditions resulted in a similar quenching of the PL.

We also incorporated Er into our nc-Si/SiO$_2$ systems and with a post-annealing at 900 °C, and we observed a strong enhancement of the Er^{3+} emission at 1.536 μm compared to samples containing no nc-Si which demonstrates the strong coupling between nc-Si and Er^{3+} ions. Since, the greater part of Er^{3+} ions are believed to be located at the interface between the nanoparticle and the SiO$_2$ matrix or deeper in the host matrix, the Er^{3+} emission gives evidence that foreign ions present in the host matrix contribute to the quenching of the PL.

The PL was considerably enhanced by applying a second post-annealing at 1100 °C to the nc-Si/SiO$_2$ samples into which P, Na, and Mg were incorporated. At low impurity concentrations, the PL intensity was even slightly enhanced for some samples with respect to the pure sample (see Fig. 5.6.). However, for atomic concentrations above ~10^{20} ions/cm^3, we observed more PL as expected, suggesting that, during the post-annealing, either the additional atoms were expelled from the crystalline core or they substituted Si atoms in the core or they were inserted into lattice interstices so that they do not act as defect anymore. However, we cannot conclude whether nc-Si embedded in silicates can exhibit PL since the atomic concentrations of Mg, Ca, and Fe that we used in our experiments were lower than, for instance, in the olivine mineral group which was already detected in space. Nevertheless, the strong decrease of the PL observed by Kachurin et al.,[44] who incorporated B into their nc-Si/SiO$_2$ systems with a B$^+$ ion fluence of 1×10^{16} ions/cm^2 resulting in an atomic peak concentrations of 7×10^{20} ions/cm^3, suggests that, above atomic concentrations of about 10^{21} ions/cm^3, the PL originating from nc-Si should be strongly quenched even after a post-annealing at 1100 °C.

We are convinced to have synthesized luminescent alloy nc-Si$_{1-x}$Ge$_x$ embedded in SiO$_2$ by ion implantation and subsequent annealing. Since Ge dangling bonds are believed to be the main factor responsible for the quenching of the PL of nc-Si$_{1-x}$Ge$_x$,[190] efforts should be devoted to the passivation of nc-Si$_{1-x}$Ge$_x$/SiO$_2$ systems by, for instance, varying the annealing conditions (temperature, duration, and environment).

6. Conclusion

In this thesis, we have studied the photoluminescence (PL) of free O-passivated silicon nanocrystals (nc-Si) and of Si nanocrystals embedded in SiO_2. We have demonstrated that the emission energy depends on the size of the nanoparticles which supports the fact that, in our samples, the PL is due to the recombination of excitons confined within the nanocrystal volume. However, our measurements have revealed that the size dependences of the PL differ whether the nanocrystals are free or embedded in a host SiO_2 matrix. Indeed, the PL spectra measured by different groups (Fig. 2.22), including ours (Fig. 4.6 and Fig. 4.14), show that, for the same peak position, the free O-passivated silicon nanoparticles are about two times larger than the nanocrystals embedded in SiO_2. We assume that the SiO_2 matrix strongly affects the PL energy of nc-Si.

Silicon nanocrystals are possible carriers of the Extended Red Emission (ERE). In astronomical observations, the ERE generally appears as a broad emission band (120 to 210-nm-wide) peaking between 600 and 850 nm (see Sec. 2.1.1.1.). The bandwidth of the ERE increases with the position of the maximum of the band (in wavelengths, see Fig. 2.2). The maximum photon conversion efficiency of the PL process leading to ERE, which was determined by astronomical observations, approaches 10% (Fig. 2.3). Ledoux et al.[37] demonstrated that the PL properties of free O-passivated nc-Si are compatible with the astronomical observations. As far as nc-Si/SiO_2 systems are concerned, quantitative measurements revealed a broad (150 to 250-nm-wide) PL band peaking between 705 and 1050 nm (see Sec. 4.2.17.). However, taking into account the fact that the size distributions of nc-Si in fused silica windows are rather broad, and the fact that cooling the samples down to temperatures below 20 K results in a blue shift of about 30 nm (Fig. 4.17), the entire spectral range observed for the ERE can be covered. We noticed that the bandwidth of the PL spectra of our nc-Si/SiO_2 systems increases with the peak position (Fig. 4.13). Free and embedded silicon nanoparticles exhibit an efficient luminescence. The maximum quantum yield of embedded nc-Si reported by Walters et al.[160] was about 60%, whereas Ledoux et al.[72] measured a maximum PL yield of free oxide-covered nc-Si of 30%. However, the PL efficiencies are even higher at low temperature, since we observed an increase of the PL intensity by a factor of ~1.4 when we cooled one of our nc-Si/SiO_2 samples down to 50 K (Fig. 4.17). Therefore, it can be concluded that nc-Si embedded in SiO_2 matrices do fulfil the requirements of an ERE carrier as far as the spectroscopy (spectral peak position, bandwidth, and PL yield) is concerned.

In order to simulate the conditions of silicates containing nc-Si, we have post-implanted into strongly luminescent nc-Si/SiO_2 systems various atomic elements, for instance magnesium and calcium, which form silicates if their oxides are combined with SiO_2. To recover the PL which disappeared completely upon the Mg^+ or Ca^+ ion irradiation, it was necessary to apply a post-annealing. We have demonstrated that the quenching of the PL observed after a post-annealing at 900 °C is due to the presence of residual defects and that a post-annealing at 1100 °C is needed to recover the PL completely (Fig. 5.6). Nevertheless, we assume that, above concentrations of about 2 at.% in fused silica, the PL originating from nc-Si

should be completely quenched even after a post-annealing at 1100 °C. This supposition is confirmed by Kachurin *et al.*[44] who observed a strong decrease of the PL by incorporating boron into their nc-Si/SiO$_2$ systems with a concentration of ~1 at.%.

Recently, red PL spectra peaking at 750 nm have been observed in crystalline Al$_2$O$_3$ samples (sapphire) where the presence of nc-Si has been clearly demonstrated.[50] However, this PL most likely arises from luminescent defect centers in the host matrix. Moreover, no PL could be observed for nc-Si embedded in hexagonal silicon carbide.[161] It seems that the embedding in crystalline matrices prevents the radiative recombination of excitons in quantum-confined nc-Si. This is probably due to the fact that the passivation of the nc-Si surface is very difficult in a crystal matrix. Therefore, one can throw doubt on the existence of luminescent nc-Si embedded in crystalline silicates. On the other hand, since we demonstrated that alloy nc-Si$_{1-x}$Ge$_x$ embedded in SiO$_2$ can exhibit PL (see Sec. 5.3.), one can consider that not only pure nc-Si could be related to the ERE, but nc-Si containing other atomic elements present in space.

Interestingly, we have shown that the PL of our nc-Si/SiO$_2$ systems is seriously quenched when the samples are implanted with high-energy ions (see Chap. 5). We have demonstrated that, even at low ion fluences (~10^{13} ions/cm^2), the amount of ions traversing a single nanoparticle induces enough structural defects within the nc-Si to explain a complete quenching of the PL (see Sec. 5.1.5). In the same way, Barratta *et al.*,[194] who studied the optical properties of porous silicon thin films subjected to He irradiation, found an evident correlation between the PL yield and the amorphization state evaluated by Raman spectroscopy. The authors questioned the possibility that crystalline silicon nanoparticles could maintain their initially high PL efficiency when they are subjected to intense ion beam irradiations like those expected in some astrophysical environments where the ERE has been observed. On the other hand, Kanemitsu[195] demonstrated that amorphous silicon (a-Si) nanostructures in the same size range of 2-5 nm exhibit broad Vis-NIR PL similar to the one emanating from nc-Si. Although the PL efficiency of a-Si nanoparticles is one order of magnitude lower than that of nc-Si at room temperature, the PL intensity of a-Si nanoparticles is significantly increased below 100 °K, and the PL yields of a-Si nanoparticles and nc-Si become comparable. Therefore, it can be assumed that under astrophysical conditions a-Si nanoparticles (free, embedded, or attached to larger grains) are competitive candidates for the ERE.

Bibliography

1   M. Cohen *et al.*, ApJ, Vol. 196, p. 179, 1975.

2   G. Ledoux *et al.*, A&A, Vol. 333, p. 39, 1998.

3   A. N. Witt, K. Gordon, and D. G. Furton, ApJ, Vol. 501, p. 111, 1998.

4   L. T. Canham, Appl. Phys. Lett., Vol. 57, p. 1046, 1990.

5   C. Delerue, G. Allan, and M. Lannoo, Phys. Rev. B, Vol. 48, p. 11024, 1993.

6   A. Li and B. T. Draine, ApJ, Vol. 564, p. 803, 2002.

7   Th. Posh, F. Kerschbaum, H. Mutschke, J. Dorschner, and C. Jäger, A&A, Vol. 393, L7-L10, 2002.

8   L. Colangeli *et al.*, Astron. Astrophys. Rev, Vol. 11, p. 97, 2003.

9   HF. Markwick-Kemper, J. D. Green, and E. Peeters, ApJ, Vol. 628, p. 119, 2005.

10   B. Garrido *et al.*, Nucl. Instr. and Meth. in Phys. Res. B, Vol. 216, p. 213, 2004.

11   S. Takeoka, M. Fujii, and S. Hayashi, Phys. Rev. B, Vol. 62, p. 16820, 2000.

12   A. Sa'ar, Y. Reichman, M. Dovrat, D. Krapf, J. Jedrzejewski, and I. Balberg, Nano Letters, Vol. 5, p. 2443-2447, 2005.

13   U. Kahler and H. Hofmeister, Optical Materials, Vol. 17, p. 83, 2001.

14   T. Orii, M. Hirasawa, and T. Seto, Appl. Phys. Lett., Vol. 83, p. 3395, 2003.

15   P. Pellegrino, B. Garrido, C. García, R. Ferré, J.A. Moreno, and J.R. Morante, Physica E, Vol. 16, p. 424, 2003.

16   S. Cheylan and R.G. Elliman, Nucl. Instr. and Meth. in Phys. Res. B, Vol. 175-177, p. 422, 2001.

17   M. Fujii, M. Yoshida, Y. Kanzawa, S. Hayashi, and K. Yamamoto, Appl. Phys. Lett, Vol. 71, p. 1198, 1997.

18   P. G. Kik and A. Polman, Mater. Sci. Eng. B, Vol. 81, p. 3, 2001.

19   V. Yu. Timoshenko *et al.*, J. Appl. Phys., Vol. 96, p. 2254, 2004.

20   G. D. Schmidt, M. Cohen, and B. Margon, ApJ, Vol. 239, p. 133, 1980.

21   A. N. Witt and R. E. Schild, ApJ, Vol. 325, p. 837, 1988.

22   A. N. Witt and T. A. Boroson, ApJ, Vol. 355, p. 182, 1990.

23   K. D. Gordon, A. N. Witt, R. J. Rudy, R. C. Puetter, D. K. Lynch, S. Mazuk, K. A. Misselt, G. C. Clayton, and T. L. Smith, ApJ, Vol. 544, p. 859, 2000.

24   D. G. Furton and A. N. Witt, ApJ, Vol. 364, p. 45, 1990.

25   D. G. Furton and A. N. Witt, ApJ, Vol. 386, p. 587, 1992.

26   J. M. Perrin and J. P. Sivan, A&A, Vol. 255, p. 271, 1992.

27   J. P. Sivan and J. M. Perrin, ApJ, Vol. 404, p. 258, 1993.

28   S. Darbon, J.M. Perrin, and J.P. Sivan, A&A, Vol. 333, p. 264, 1998.

29   S. Daron, A. Zavagno, J. M. Perrin, C. Savine, V. Ducci, and J. P. Sivan, A&A, Vol. 364, p. 723, 2000.

30   J. M. Perrin, S. Darbon, and J. P. Sivan, A&A, Vol. 304, p. 21, 1995.

31   D. Pierini, A. Majeed, T. A. Boroson, and A. N. Witt, ApJ., Vol. 569, p. 184, 2002.

32   K. D. Gordon, A. N. Witt, and B. C. Friedmann, ApJ, Vol. 498, p. 522, 1998.

33   A. N. Witt and U. P. Vijh, Astrophysics of Dust, ASP Conference Series, edited by A. N. Witt, G. C. Clayton and B. T. Draine, Vol. 309, Proceedings of the conference held 26-30 May, 2003 in Estes Park, Colorado, p. 115, 2004.

34   S. Darbon; J. M. Perrin, J. P. Sivan, A&A, Vol. 348, p. 990, 1999.

35   A. N. Witt and R. E. Schild, ApJ, Vol. 294, p. 225, 1985.

36   T. L. Smith and A. N. Witt, ApJ, Vol. 565, p. 304, 2002.

37   G. Ledoux, O. Guillois, F. Huisken, B. Kohn, D. Porterat, and C. Reynaud, A&A, Vol. 377, p. 707, 2001.

38   K. Lodders, ApJ, Vol. 591, p. 1220, 2003.

39   V. Vinciguerra, G. Franzò, F. Priolo, F. Iacona, and C. Spinella, J. Appl. Phys., Vol. 87, p. 8165, 2000.

40   Y. Kanzawa, T. Kageyama, S. Takeoka, M. Fujii, S. Hayashi, and K. Yamamoto, Solid State Commun., Vol. 102, p. 533, 1997.

41   M. Fujii, A. Mimura, S. Hayashi, K. Yamamoto, C. Urakawa, and H. Ohta, J. Appl. Phys., Vol. 87, p. 1855, 2000.

42   A. Mimura, M. Fujii, S. Hayashi, and K. Yamamoto, Solid State Commun., Vol. 109, p. 561, 1999.

43   A. L. Tchebotarevaa, M. J. A. de Dooda, J. S. Biteen, H. A. Atwater, and A. Polman, J. Lumin., Vol. 114, p. 137, 2005.

44   G. A. Kachurin et al., Semiconductors, Vol. 40, p. 72, 2006.

45   M. Fujii, A. Mimura, S. Hayashi, Y. Yamamoto, and K. Murakami, Phys. Rev. Lett., Vol. 89, p. 206805, 2002.

46   Y. C. Fang, Z. J. Zhanga, Z. Q. Xie, Y. Y. Zhao, and M. Lu, Appl. Phys. Lett., Vol. 86, p. 191919, 2005.

47   K. Matsumoto, M. Fujii, and S. Hayashi, Jpn J. Appl. Phys., Vol. 45, L450, 2006.

48   M. Fujii, K. Toshikiyo, Y. Takase, Y. Yamaguchi, and S. Hayashi, J. Appl. Phys., Vol. 94, p. 1990, 2003.

49   O. N. Gorshkov, Yu. A. Dudin, V. A. Kamin, A. P. Kasatkin, A. N. Mikhaylov, V. A. Novikov, and D. I. Tetelbaum, Tech. Phys. Lett., Vol. 31, p. 509, 2005.

50   D. I. Tetelbaum et al., Thin Solid Films, Vol. 515, p. 333, 2006.

51   U. P. Vijh, A. N. Witt, and K. D. Gordon, ApJ, Vol. 606, p. 65, 2004.

52   U. P. Vijh, A. N. Witt, and K. D. Gordon, ApJ, Vol. 633, p. 262, 2005.

53   M. H. Nayfeh, S. R. Habbal, and S. Rao, ApJ, Vol. 621, p. 121, 2005.

54   A. N. Witt, K. D. Gordon, U. P. Vijh, P. H. Sell, T. L. Smith, and R. H. Xie, ApJ, Vol. 636, p. 303, 2006.

55   M. Nirmal and L. Brus, Acc. Chem. Res., Vol. 32, p. 407, 1999.

56   S. R. Habbal, M. B. Arndt, M. H. Nayfeh, J. Arnaud, J. Johnson, S. Hegwer, R. Woo, A. Ene, and F. Habbal, ApJ, Vol. 592, p. 87, 2003.

57   J. Singh, T. Sakurai, K. Ichimoto, M. Hagino, and T. T. Yamamoto, ApJ, Vol. 608, p. 69, 2004.

58   I. Mann and E. Murad, ApJ, Vol. 624, p. 125, 2005.

59   E. O. Kane, Phys. Rev., Vol. 146, p. 558, 1966.

60   V. Lehman and U. Gösele, Appl. Phys. Lett., Vol. 58, p. 856, 1991.

61   D. Kovalev and M. Fujii, Adv. Mater., Vol. 17, p. 2531, 2005.

62   L. Tsybeskov, K. L. Moore, D. G. Hall, and P. M. Fauchet, Phys. Rev. B, Vol. 54, p. 8361, 1996.

63   N. A. Hill and K. B. Whaley, Phys. Rev. Lett., Vol. 75, p. 1130, 1995.

64   N. A. Hill and K. B. Whaley, Phys. Rev. Lett., Vol. 76, p. 3039, 1996.

65   M. Nishida, Semicond. Sci. Technol., Vol. 21, p. 443-449, 2006.

66   L. W. Wang and A. Zunger, J. Phys. Chem., Vol. 98, p. 2158, 1994.

67   M. Luppi and S. Ossicini, Phys. Rev. B, Vol. 71, p. 035340, 2005.

68   E. W. Draeger, J. C. Grossman, A. J. Williamson, and G. Galli, J. Chem. Phys., Vol. 120, p. 10807, 2004.

69   L. E. Ramos, J. Furthmüller, and F. Bechstedt, Phys. Rev. B, Vol. 71, p. 035328-1, 2005.

70   A. Puzder, A. J. Williamson, J. C. Grossman, and G. Galli, J. Am. Chem. Soc., Vol. 125, p. 2786-2791, 2003.

71   M.V. Wolkin, J. Jones, P. M. Fauchet, G. Allan, and C. Delerue, Phys. Rev. Lett., Vol. 82, p. 198, 1999.

72   G. Ledoux, J. Gong, F. Huisken, O. Guillois, and C. Reynaud, Appl. Phys. Lett., Vol. 80, p. 4834, 2002.

73   R. B. Wehrspohn, J. N. Chazalviel, F. Ozanam, and I. Solomon, Eur. Phys. J., Vol. 8, p. 179, 1999.

74   D. Pacifici, E. C. Moreira, G. Franzò, V. Martorino, and F. Priolo, Phys. Rev. B, Vol. 65, p. 144109, 2002.

75   F. Koch, V. Petrova-Koch, and T. Muschik, J. Lumin., Vol. 57, p. 271, 1993.

76   S. M. Prokes, Appl. Phys. Lett., Vol. 62, p. 3244, 1993.

77   T. Shimizu-Iwayama, N. Kurumado, D. E. Hole, and P. D. Townsend, J. Appl. Phys., Vol. 83, p. 6018, 1998.

78   Y. Kanemitsu, Phys. Rev. B, Vol. 48, p. 4883, 1993.

79   M. López, B. Garrido, C. García, P. Pellegrino, A. Pérez-Rodriguez, C. Bonafos, M. Carrada, and A. Claverie, Appl. Phys. Lett., Vol. 80, p. 1637, 2002.

80   E. P. O'Reiily and J. Robertson, Phys. Rev. B, Vol. 27, p. 3780, 1983.

81   R. Tohmon, Y Shimogaichi, H. Mizuno, and Y. Ohki, Phys. Rev. B, Vol. 62, p. 1388, 1989.

82   L. Rebohle, J. von Borany, H. Fröb, and W. Skorupa, Appl. Phys. B, Vol. 71, p. 131, 2000.

83   S. Munekumi, T. Yamanaka, Y. Shimogaichi, K. Nagasawa, and Y. Yama, J. Appl. Phys., Vol. 68, p. 1212, 1990.

84   S. M. Prokes and W. E. Carlos, J. Appl. Phys., Vol. 78, p. 2671, 1995.

85   A. Colder, F. Huisken, E. Trave, G. Ledoux, O. Guillois, C. Reynaud. H. Hofmeister, and E. Pippel, Nanotechnology, Vol. 15, L1-L4, 2004.

86   A. G. Cullis, L. T. Canham, and P. D. J. Calcott, J. Appl. Phys., Vol. 82, p. 909, 1997.

87   A. K. Sood, K. Jayaram, and D. V. S. Muthu J. Appl. Phys., Vol. 72, p. 4963, 1992.

88   H. Hofmeister, F.Huisken, and B. Kohn, Eur. Phys. J., Vol. 9, p. 137-140, 1999.

89   G. Ledoux, O. Guillois, D. Porterat, C. Reynaud, F. Huisken, B. Kohn, and V. Paillard, Phys. Rev. B, Vol. 62, p. 15942, 2000.

90   M. Hyeonsik, M. Cheong, W. Paul, S. P. Withrow, J. G. Zhu, J. D. Budai, C. W. White, and D. M. Hembree Jr., Appl. Phys. Lett., Vol. 68, p. 87, 1996.

91   L. Patrone, D. Nelson, V. I. Safarov, M. Sentis, W. Marineb, and S. Giorgio, J. Appl. Phys., Vol. 87, p. 3830, 2000.

92   www.pvd-coating.co.uk

93   D. B. Geohegan, A. A. Puretzky, G. Duscher, and S. J. Pennycook, Appl. Phys. Lett., Vol. 72, p. 2987, 1998.

94   M. Ehbrecht, B. Kohn, F. Huisken, M. A. Laguna, and V. Paillard, Phys. Rev. B, Vol. 56, p. 6958, 1997.

95   M. L. Ostraat, M. Brongersma, H. A. Atwater, and R. C. Flagan, Solid State Sciences, Vol. 7, p. 882-890, 2005.

96   J. J. Wu, H. V. Nguyen, and R. C. Flagan, Langmuir, Vol. 3, p. 266, 1987.

97   S. Schuppler et al., Phys. Rev. B, Vol. 52, p. 4910, 1995.

98   K. A. Littau, P. J. Szajowski, A. J. Muller, A. R. Kortan , and L. E. Brus, J. Phys. Chem., Vol. 97, p. 1224-1230, 1993.

99   D. J. DiMaria, J. R. Kirtley, E. J. Pakulis, D. W. Dong, T. S. Kuan, F. L. Pesavento, T. N. Theis, J. A. Cutro, S. D. Brorson, J. Appl. Phys., Vol. 56, p. 401, 1984.

100   M. L. Hitchman and J. Kane, J. Crys. Grow, Vol. 55, p. 485, 1981.

101   M. Fukuda, K. Nakagawa, S. Miyazaki, and M. Hirose, Appl. Phys. Lett., Vol. 70, p. 2291, 1997.

102   A. Nakajima, Y. Sugita, K. Kawamura, H. Tomita, and N. Yokoyama, J. Appl. Phys., Vol. 80, p. 4006, 1996.

103   H. Takagi, H. Ogawa, Y. Yamazaki, A. Ishizaki, and T. Nakagiri, Appl. Phys. Lett., Vol. 56, p. 2379, 1990.

104   N. Chaâbane, V. Suendo, H. Vach and P. Roca i Cabarrocasa, Appl. Phys. Lett., Vol. 88, p. 203111, 2006.

105   T. Inokuma, Y. Wakayama, T. Muramoto, R. Aoki, Y. Kurata, and S. Hasegawa, J. Appl. Phys., Vol. 83, p. 2228, 1998.

106   F. Iacona, G. Franzò, and C. Spinella, J. Appl. Phys., Vol. 87, p. 1295, 2000.

107   S. Guha, S. B. Qadri, R. G. Musket, M. A. Wall, and T. Shimizu-Iwayama, J. App. Phys., Vol. 88, p. 3954, 2000.

108   A. Hryciw, A. Meldrum, K. S. Buchanan, and C. W. White, Nucl. Instr. and Meth. in Phys. Res. B, Vol. 222, p. 469, 2004.

109   U. S. Sias, L. Amaral, M. Behar, H. Boudinov, E. C. Moreira, and E. Ribeiro, J. Appl. Phys., Vol. 98, p. 034312, 2005.

110   G. Franzò, E. C. Moreira, D. Pacifici, F. Priolo, F. Iacona, C. Spinella, Nucl. Instr. and Meth. in Phys. Res. B, Vol. 175-177, p. 140, 2001.

111   M. Carrada, A. Wellner, V. Paillard, C. Bonafos, H. Coffin and A. Claverie, Appl. Phys. Lett., Vol. 87, p. 251911, 2005.

112   M. Fujii, S. Hayashi, and K. Yamamoto, in Recent Research Development in Applied Physics, ed. S. G. Pandalai, (Transworld Research Network, Trivandrum), Vol. 1, p. 193, 1998.

113   M. Fujii, M. Yoshida, S. Hayashi, and K. Yamamoto, J. Appl. Phys., Vol. 84, p. 4526, 1998.

114   G. Conibeer *et al.*, Thin Solid Films, Vol. 511-512, p. 654, 2006.

115   M. Ohring, Academic Press, San Diego, CA, 1992.

116   S. Furukawa and T. Miyasato, Phys. Rev. B, 38, Vol. 38, p. 5726, 1988.

117   S. Hayashi, Y. Kanzawa, M. Kataoka, T. Nagareda, and K. Yamamoto, Z. Phys. D, Vol. 26, p. 144, 1993.

118   M. Fujii, K. Imakita, K. Watanabe, and S. Hayashi, J. Appl. Phys., Vol. 95, p. 272, 2004.

119 B. H. Sullivan, D. J. Lockwood, H. J. Labbé, and Z. H. Lu, Appl. Phys. Lett., Vol. 69, p. 3149, 1996.

120 H. Seifarth, R. Grötzschel, A. Markwitz, W. Matz, P. Nitzsche, and L. Rebohle, Thin Solid Films, Vol. 330, p. 202, 1998.

121 J. von Behren, T. van Buuren, M. Zacharias, E. H. Chimowitz, and P. M. Fauchet, Solid State Commun., Vol. 105, p. 317, 1998.

122 C. Ternon, PhD thesis, Universtité de Caen, 2002.

123 D. Amans, O. Guillois, G. Ledoux, D. Porterat, and C. Reynaud, J. Appl. Phys., Vol. 91, p. 5334, 2002.

124 S. Guha, J. App. Phys., Vol. 84, p. 5210, 1998.

125 S. Takeoka, K. Toshikiyo, M. Fujii, S. Hayashi, and K Yamamoto, Phys. Rev. B, Vol. 61, p. 15988, 2000.

126 G. V. Prakash, M. Cazzanelli, Z. Gaburro, L. Pavesi, F. Iacona, G. Franzò, and F. Priolo, J. Modern Optics, Vol. 49, p. 719, 2002.

127 L. Pavesi, L. Dal Negro, C. Mazzoleni, G. Franzò, and F. Priolo, Nature, Vol. 408, p. 440, 2000.

128 R. J. Walters, P. G. Kik, J. D. Casperson, H. A. Atwater, R. Lindstedt, M. Giorgi, and G. Bourianoff, Appl. Phys. Lett., Vol. 85, p. 2622, 2004.

129 V. Yu. Timoshenko *et al.*, JETP Letters, Vol. 17, p. 423, 2006.

130 L. Wang, V. Reipa, and J. Blasic, Bioconjugate Chem., Vol. 15, p. 409, 2004.

131 W. J. Parak, T. Pellegrino, and C. Plank, Nanotechnology, Vol. 16, R9-R25, 2005.

132 H. S. Han, S. Y. Seo, and J. H. Shin, Appl. Phys. Lett., Vol. 79, p. 4568, 2001.

133 J. P. Biersack and L. J. Haggmark, Nucl. Instr. Meth., Vol. 174, p. 257, 1980.

134 F. Cichos, J. Martin, and C. von Borczyskowski, Phys, Rev. B, Vol. 70, p. 115314, 2004.

135 B. R. Fisher, H. J. Eisler, N. E. Stott, and M. G. Bawendi, J. Phys. Chem. B, Vol. 108, p. 143, 2004.

136 G. Schlegel, J. Bohnenberger, I. Potapova, and A. Mews, Phys. Rev. Lett., Vol. 88, p. 137401, 2002.

137 J. Linnros, N. Lalic, A. Galeckas, and V. Grivickas, J. Appl. Phys., Vol. 86, p. 6128, 1999.

138 O. Guillois, N. Herlin-Boime, C. Reynaud, G. Ledoux, and F. Huisken, J. Appl. Phys., Vol. 95, p. 3678, 2004.

139 A. F. van Driel, PhD thesis, Universiteit Utrecht, 2006.

140 C. Delerue, G. Allan, C. Reynaud, O. Guillois, G. Ledoux, F. Huisken, Phys. Rev. B, Vol. 73, p. 235318, 2006.

141   E. Wendler, U. Hermann, W. Wesch, and H. H. Dunken, Nucl. Instr. and Meth. In Phys. Res. B, Vol. 116, p. 332, 1996.

142   G. G. Ross, R. Smirani, V. Levitcharsky, Y. Q. Wang, G. Veilleux, R. G. Saint-Jaques, Nucl. Instr. and Meth. in Phys. Res. B, Vol. 230, p. 198, 2005.

143   R. G. Elliman, M. J. Lederer, and B. Luther-Davies, Appl. Phys. Lett., Vol. 80, p. 1325, 2002.

144   Y. M. Niquet, G. Allan, C. Delerue, and M. Lannoo, Appl. Phys .Lett, Vol. 77, p. 1182, 2000.

145   A. Wellner, V. Paillard, H. Coffin, N. Cherkashin, and C. Bonafos, J. Appl. Phys., Vol. 96, p. 2403, 2004.

146   M. Benyoucef, M. Kuball, J. M. Sun, G. Z. Zhong, and X. W. Fan, J. Appl. Phys., Vol. 89, p. 7903, 2001.

147   L. Khriachtchev, O. Kilpelä, S. Karirinne, J. Keränen, and T. Lepistö, Appl. Phys. Lett. B, Vol. 78, p. 323, 2001.

148   V. Paillard, P. Puech, M. A. Laguna, R. Carles, B. Kohn, and F. Huisken, J. Appl. Phys., Vol. 86, p. 1921, 1999.

149   V. Paillard, P. Puech, and P. Roca i Cabarrocas, J. Non-Cryst. Solids, Vol. 299–302, p. 280, 2002.

150   A. Wellner, V. Paillard, C. Bonafos, H. Coffin, A. Claverie, B. Schmidt, and K. H. Heinig, J. Appl. Phys., Vol. 94, p. 5639, 2003.

151   S. Cheylan, N. Langford, and R. G. Elliman, Nucl. Instr. and Meth. in Phys. Res. B, Vol. 166-167, p. 851, 2000.

152   G. H. Li, K. Ding, Y. Chen, H. X. Han, and Z. P. Wang, J. Appl. Phys., Vol. 88, p. 1439, 2000.

153   S. P. Withrow, C. W. White, A. Meldrum, J. D. Budai, D. M. Hembree Jr., and J. C. Barbour, J. Appl. Phys., Vol. 86, p. 396, 1999.

154   A. R. Wilkinson and R. G. Elliman, J. Appl. Phys., Vol. 96, p. 4018, 2004.

155   S. Cheylan and R.G. Elliman, Nucl. Instr. and Meth. in Phys. Res. B, Vol. 175-177, p. 422, 2001.

156   A. R. Wilkinson and R. G. Elliman, Appl. Phys. Lett., Vol. 83, p. 5512, 2003

157   K. S. Min, K. V. Shcheglov, C. M. Yang, H. A. Atwater, M. L. Brongersma, and A. Polman, Appl. Phys. Lett., Vol. 69, p. 2033, 1996.

158   T. Shimizu-Iwayama, D. E. Hole, and I. W. Boyd, J. Phys.: Condens. Matter, Vol. 11, p. 6595, 1999.

159   M. L. Brongersma, A. Polman, K. S. Min, E. Boer, T. Tambo, and H. A. Atwater, Appl. Phys. Lett., Vol. 72, p. 2577, 1998.

160   R. J. Walters, J. Kalkman, A. Polman, H. A. Atwater, and M. J. A. de Dood, Phys. Rev. B, Vol. 73, p. 132302, 2006.

161   U. Kaiser, J. Biskupek, and K. Gärtner, Phil. Mag. Lett., Vol. 83, p. 253, 2003.

162   A. Heft, E. Wendler, J. Heindl, T. Bachmann, E. Glaser, H. P. Strunk, and W. Wesch, Nucl. Instr. and Meth. in Phys. Res. B, Vol. 113, p. 239, 1996.

163   F. Huisken, G. Ledoux, O. Guillois, and C. Reynaud, Adv. Mater., Vol. 14, p. 1861, 2002.

164   H. Koyama, T. Ozaki, and N. Koshida, Phys. Rev. B, Vol. 52, p. 561, 1995.

165   F. Priolo, G. Franzo, D. Pacifici, V. Vinciguerra, F. Iacona, and A. Irrera, J. Appl. Phys., Vol. 89, p. 264, 2001.

166   M. L. Brongersma, P. G. Kik, A. Polman, K. S. Min, and H. A. Atwater, Appl. Phys. Lett., Vol. 76, p. 351, 2000.

167   P. D. J. Calcott, K. J. Nash, L. T. Canham, M. J. Kane, and D. Brumhead, J. Lumin., Vol. 57, p. 257, 1993.

168   J. Heitmann, F. Müller, L. Yi, M. Zacharias, D. Kovalev, and F. Eichborn, Phys. Rev. B, Vol. 69, p. 195309, 2004.

169   M. Dovrat, Y. Goshen, J. Jedrzejewski, I. Balberg, and A. Sa'ar, Phys. Rev. B, Vol. 69, p. 155311, 2004.

170   A. Yu. Kobitski, K. S. Zhuravlev, H. P. Wagner, and D. R. T. Zahn, Phys. Rev. B, Vol. 63, p. 115423, 2001.

171   D. Kovalev, H. Heckler, G. Polisski, and F. Koch, Adv. Mater., Phys. Stat. Sol. B, Vol. 215, p. 871, 1999.

172   G. A. Kachurin, S. G. Yanovskaya, D. I. Tetelbaum, and A. N. Mikhailov, Semiconductors, Vol. 37, p. 713, 2003.

173   A. Mimura, M. Fujii, S. Hayashi, D. Kovalev and F. Koch, Phys. Rev. B, Vol. 62, p. 12625, 2000.

174   S. Sen, J. Siejka, A. Savtchouk, and J. Lagowski, Appl. Phys. Lett., Vol. 70, p. 2253, 1997.

175   G. Cantele, E. Degoli, E. Luppi, R. Magri, D. Ninno, G. Iadonisi, and S. Ossicini, Phys. Rev. B, Vol. 72, p. 113303, 2005.

176   M. Fujii, Y. Yamaguchi, Y. Takase, K. Ninomiya, and S. Hayashi, Appl. Phys. Lett., Vol. 87, p. 211919, 2005.

177   D. Pacifici, G. Franzò, F. Priolo, F. Iacoma, and L. Dal Negro, Phys. Rev. B, Vol. 67, p. 245301, 2003.

178   K. Watanabe, M. Fujii, and S. Hayashi, J. Appl. Phys., Vol. 90, p. 4761, 2001.

179   G. Franzò, V. Vinciguerra, and F. Priolo, Appl. Phys. A, Vol. 69, p. 3, 1999.

180 S. Takeoka, M. Fujii, S. Hayashi, and K. Yamamoto, Phys. Rev. B, Vol. 58, p. 7921, 1998.

181 L. Rebohle, J. von Borany, R. A. Yankov, W. Skorupa, I. E. Tyschenko, H. Fröb, and K. Leo, Appl. Phys. Lett., Vol. 71, p. 2809, 1997.

182 Y. Maeda, Phys. Rev. B, Vol. 51, p. 1658, 1995.

183 Y. Kanemitsu, H. Uto, Y. Masumoto, and Y. Maeda, Appl. Phys. Lett., Vol. 61, p. 2187, 1992.

184 G. A. Kachurin, L. Rebohle, I. E. Tyschenko, V. A. Volodin, M. Voelskow, W. Skorupa, and H. Froeb, Semiconductors, Vol. 34, p. 23, 2000.

185 P. K. Giri, R. Kesavamoorthy, B. K. Panigrahi, and K. G. M. Nair, Solid State Commun., Vol. 133, p. 229, 2004.

186 K. S. Min, K. V. Shcheglov, C. M. Yang, H. A. Atwater, M. L. Brongersma, and A. Polman, Appl. Phys. Lett., Vol. 68, p. 2511, 1996.

187 W. S. Lee, J. Y. Jeong, H. B. Kim, K. H. Chae, C. N. Whang, S. Im, and J. H. Song, ,Mater. Sci. Eng. B, Vol. 69-70, p. 474, 2000.

188 G. Kartopu, V. A. Karavanskii, U. Serincan, R. Turan, R. E. Hummel, Y. Ekinci, A. Gunnaes, and T. G. Finstad, Phys. Stat. Sol. (a), Vol. 202, p. 1472, 2005.

189 C. Delerue, G. Allan, and M. Lannoo, J. Lumin., Vol. 80, p. 65, 1999.

190 K. Toshikiyo, M. Tokunaga, S. Takeoka, M. Fujii, and S. Hayashi, J. Appl. Phys., Vol. 89, p. 4917, 2001.

191 M. Fujii, D. Kovalev, J. Diener, F. Koch, S. Takeoka, and S. Hayashi, J. Appl. Phys., Vol. 88, p. 5772, 2000.

192 H. -Ch. Weissker, F. Furthmüller, and F. Bechstedt, Phys. Rev. Lett., Vol. 90, p. 85501, 2003.

193 Y. M. Yang, X. L. Wu, G. S. Huang, D. S. Hu, and G.G. Siu, Phys. Lett. A, Vol. 338, p. 379, 2005.

194 G. A. Baratta, G. Strazzulla, G. Compagnini, and P. Longo, Appl. Surf. Sci., Vol. 226, p. 57, 2004.

195 Y. Kanemitsu, J. Lumin., Vol. 100, p. 209, 2002.

196 K. Koike, M. Nakagawa, C. Koike, H. Chihara, M. Okada, M. Matsumura, T. Awata, K. Atobe, and J. Takada, Planet. Space Sci., Vol. 54, p. 325, 2006.

197 C. Koike, H. Chihara, K. Koike, M. Nakagawa, M. Okada, A. Tsuchiyama, M. Aoki, T. Awata, and K. Atobe, Meteorit. Planet. Sci., Vol. 37, p. 1591, 2002.

198 L. Skuja, T. Suzuki, and K. Tanimura, L. Skuja, T. Suzuki, and K. Tanimura, Phys Rev. B, Vol. 52, p. 15208, 1995.

199 Ch. Mühlig, W. Triebel, S. Bark-Zollmann, and D. Grebner, Nucl. Instr. and Meth. in Phys. Res. B, Vol. 166-167, p. 698, 2000.

Appendix A

Ref.	Production technique	Production characteristic		nc-Si state	Size determination method	Size (nm)	Photo-luminescence	λ_{PL} (nm)
Ehbrecht *et al.* (1997)	Laser pyrolysis of silane	Nucleation of Si generated by laser decomposition of silane in a gas flow reactor. A nozzle and a chopper placed inside the resulting aerosol flow achieve a size separation for the final deposit.	The deposit films were conserved in Argon	Free nc-Si	Time-of-flight mass spectrometry (TOFMS), confirmed by Raman spectroscopy.	3.6 ± 0.9 - 4.7 ± 1.2	Ar⁺-laser at 448 nm Kr-laser at 647 nm	700 – 830
Ledoux *et al.* (2000 ; 2001)]			The deposit films were oxidized by **exposition to air**	Free nc-Si covered with a SiO$_2$ layer	Non-oxidized clusters sizes were determined by TOFMS. They were in good agreement with sizes obtained by atomic force microscopy (AFM) of fresh deposited samples.	2.8 – 4.5	Nd:Yag laser at 266 nm, <1 µJ/cm²	610 - 895
Ledoux *et al.* (2002)			The deposit films were oxidized by **exposition to air**	Free nc-Si covered with a SiO$_2$ layer	Non-oxidized clusters size were determined by TOFMS, and confirmed by AFM. Sizes of oxidized nc-Si were evaluated by a reduction of 8 to 16% of the non-oxidized clusters size. This factor is the relative SiO$_2$ layer thickness of the total core-shell structure found by **TEM**.	2.8 - 7.5	Nd:Yag laser at 266 nm, <1 µJ/cm²	610 - 895
Patrone *et al.* (2000)	Pulsed-laser ablation	Synthesis by pulsed laser ablation of a single silicon crystal in a high-purity He gas chamber to avoid oxidation. A size separation was achieved by the fact that, after the laser irradiation, the Si particles plasma expands perpendicularly to the deposit target in a form of a plume, where the smallest nc-Si are scattered and consequently deposited at longer distances whereas the largest clusters are deposited closer to the laser spot. The PL spectra were performed immediately after preparation.		Free nc-Si	AFM confirmed by **HRTEM**	1.3 – 3.8	Xe lamp	353 - 727

Reference	Method	Description	Structure	Characterization	Size (nm)	Excitation	PL (nm)
Orii *et al.* (2003)	**Pulsed-laser ablation**	nc-Si are resulting from the ablation of a single silicon crystal by a pulsed laser, and subsequently **annealed** at 900 °C and separated in size by a differential mobility analyzer and finally deposited on a substrate.	Free nc-Si covered with a SiO$_2$ layer	**HRTEM** / cross section The relative SiO$_2$ layer thickness was around 51% for the smallest nc-Si and 29% for the largest ones of the total core-shell structure	2.1 – 4.9	Ar$^+$-laser at 514.5 nm He-Cd laser at 325 nm, 0.25 W/cm²	691 - 923
Schuppler *et al.* (1995)	**Aerosol technique**	Nucleation of Si atoms generated by pyrolysis of disilane in a high-pressure flow of He at 700 - 1000 °C with a subsequent **oxidation in O$_2$** at 700-1000 °C during 30 ms. The resulting aerosol is bubbled through ethylene glycol to be finally separated in size by precipitation.	Free nc-Si covered with a SiO$_2$ layer	**TEM** / cross section / dark-field The relative SiO$_2$ layer thickness was around 29% for the smallest nc-Si and 9% for the largest ones of the total core-shell structure.	1.1±0.1 - 7.8±1.7	~2 mW/cm²	665 - 890
Ostraat *et al.* (2005)	**Aerosol technique**	Nucleation of Si from pyrolysis of silane in an oxygen-free furnace at 950 °C. Nc-Si form for 30 ms in a gas flow of N$_2$ and are extracted out of the reactor. Particles, in the so-formed aerosol, are positively charged with a Kr ion gas and migrate radially in the presence of a negative electric field. A size separation is realized according to the principle that the particles mobility depends only on the nc-Si mass. Particles are subsequently passivated with a tetraethylorthosilicate (TEOS)-derived oxide. The Si nanoparticle aerosol passes over liquid TEOS in a temperature controlled evaporator (300 to 1000 °C).	Free nc-Si covered with a SiO$_2$ layer	**TEM** / dark-field The relative SiO$_2$ layer thickness represented around 40% of the total core-shell structure.	8 & 12	Ar$^+$-laser at 257 nm, 1 mW/mm²	1094
Takagi *et al.* (1990)	**Microwave decomposition of SiH$_4$ & H$_2$**	Nucleation of nc-Si from decomposition of silane and H$_2$ (MPCVD). A nozzle placed inside the resulting aerosol flow achieves a size separation for the final deposit. Nc-Si films are first surrounded with an amorphous layer of polysilane but exhibited no-PL. After **oxidization** by exposition to a **humid atmosphere** (85%) at 60 °C, the films are covered by a SiO$_2$ layer and exhibit PL.	Free nc-Si covered with a SiO$_2$ layer	XRD: size dependence on the half width of the (111) crystalline silicon line (Sherrers´ formula)	2.9 – 4.7	Lamp	759 - 877

Reference	Method	Description	Annealing condition	Material	Technique	Size (nm)	Excitation	Peak (nm)
Inokuma *et al.* (1997)	**PECVD (SiH₄ & N₂O)**	Condensation of a silicon suboxide $SiO_{x<2}$ films, produced by PECVD, by **annealing** from 650 °C to 1100 °C in an N₂ atmosphere during one hour to precipitate the excess of silicon in nc-Si.		nc-Si embedded in SiO_2	**TEM**	2.5; 3.4	Ar⁺-laser at 488 nmn	754; 783
Vinciguerra *et al.* (2000)	**PECVD (SiH₄ & N₂O)**	Condensation of a silicon suboxide $SiO_{x<2}$ films, produced by PECVD, by an **annealing** at 1200 °C in N₂ during one hour to precipitate the excess of silicon in nc-Si.		nc-Si embedded in SiO_2	**TEM** / plan view	2.2±0.8 - 4.6±2.4	Ar⁺-laser at 488 nm, 5 - 500 mW, 55 Hz.	800 - 910
Iacona *et al.* (2000)	**PECVD (SiH₄ & N₂O)**	Condensation of a silicon suboxide $SiO_{x<2}$ films, produced by PECVD, by an **annealing** at high temperature (1000 – 1300 °C) in N₂ during one hour to precipitate the excess of silicon in nc-Si.		nc-Si embedded in SiO_2	**TEM** / plan view	1.3 - 4.2	Ar⁺-laser at 488 nm, 50 mW, 55 Hz.	835 - 945
Prakash *et al.* (2002)	**PECVD (SiH₄ & N₂O)**	Condensation of a silicon suboxide $SiO_{x<2}$ films, produced by PECVD, by an **annealing** at 1250 °C in N₂ to precipitate the excess of silicon in nc-Si.		nc-Si embedded in SiO_2	**TEM**	3 – 4.2	Ar⁺-laser at 488 nm, 10 mW	793 - 930
Kanzawa *et al.* (1997)	**Magnetron co-sputtering**	Condensation of a silicon suboxide $SiO_{x<2}$ films, produced by magnetron cosputtering, by an **annealing** at 1100 °C in N₂ during 30 min. to precipitate the excess of silicon in nc-Si.		nc-Si embedded in SiO_2	**HRTEM** / cross section	2.7±0.3 – 3.8±0.8	Ar⁺-laser at 458 nm, 3 W/cm²	805 - 865
Mimura *et al.* (1999)	**Cosputtering**	Condensation of a silicon suboxide $SiO_{x<2}$ films, produced by cosputtering, by an **annealing** at high temperature in N₂ atmosphere to precipitate the excess of silicon in nc-Si.	**Annealing** at 1100 °C during 30 min	nc-Si embedded in SiO_2	**HRTEM** / cross section	3.5	Ar⁺-laser at 458 nm, 1 to 30 mW	871
Takeoka *et al.* (2000)			-			4.7 – 9	Ar⁺-laser at 488 nm, 4mW/cm²	900 - 1005
Fujii *et al.* (1998) a,b			**Annealing** at 1100 °C			2.7 – 3.8	1.5 W/cm²	800 - 870

Reference	Method	Description	Structure	Characterization	Size (nm)	Excitation	Range
Conibeer et al. (2006)	Co-sputtering	Condensation of a silicon suboxide $SiO_{x<2}$ films, produced by cosputtering, by an **annealing** at 1100 °C during 30 min in N_2 atmosphere to precipitate the excess of silicon in nc-Si.	nc-Si embedded in SiO_2	**HRTEM** / cross section	2 ± 0.2 – 4.6 ± 0.5	-	730 - 930
Sa'ar et al. (2005)	Co-sputtering	Condensation of a silicon suboxide $SiO_{x<2}$ films, produced by cosputtering, by an **annealing** at 1150 °C during 30 min in N_2 atmosphere to precipitate the excess of silicon in nc-Si.	nc-Si embedded in SiO_2	**HRTEM** / cross section	3 ± 1 – 6.7 ± 2.6	Ar^+-laser at 488 nm	651 - 835
Kahler & Hofmeister (2001)	Reactive evaporation of SiO	Condensation of a silicon suboxide $SiO_{x<2}$ films, produced by reactive evaporation of SiO, by an **annealing** at 1000 °C in Ar to precipitate the excess of silicon in nc-Si.	nc-Si surrounded by a SiO_2 matrix	**TEM**	3 ± 0.3 – 4.3 ± 0.6	He-Cd laser at 325 nm	780 - 885
Carrada et al. (2006)	Low energy ion beam implantation in SiO_2	Condensation of a silicon suboxide $SiO_{x<2}$ films, produced by low-energy ion beam implantation in quartz, by an **annealing** at 1050 °C in N_2 during 30 min. and a post-annealing at 900 °C in an (N_2 + 1.5% O_2) atmosphere to precipitate the excess of silicon in nc-Si.	nc-Si embedded in SiO_2	**TEM** / plan view Energy loss spectroscopy (EELS)	1.8 ± 0.2 – 2.9 ± 0.2	Ar-laser at 488 nm, <0.2 mW	715 - 830
Garrido et al. (2004)	Ion implantation in SiO_2	Condensation of a silicon suboxide $SiO_{x<2}$ films, produced by ion implantation in quartz, by **annealings** at 1100 °C in N_2 and at 450 °C in an (N_2 + 5% O_2) atmosphere to precipitate the excess of silicon in nc-Si.	nc-Si embedded in SiO_2	**HRTEM** / cross section / dark-field	$2.7 - 7$	He-Cd laser at 325 nm	710 - 885
Sias et al. (2005)	Ion implantation in SiO_2	Condensation of a silicon suboxide $SiO_{x<2}$ films, produced by ion implantation in quartz, performed at room temperature and at 600 °C, by an **annealing** at 1100 °C in N_2 during one hour to precipitate the excess of silicon in nc-Si.	nc-Si embedded in SiO_2	**HRTEM** / cross section / dark-field	3; 3.8	Xe lamp, 20 mW/cm²	773; 800

Reference	Method	Description	Material	Characterization	Size	Laser	Value
Hryciw *et al.* (2004)	**Ion implantation in SiO₂**	Condensation of a silicon suboxide SiO$_{x<2}$ films, produced by ion beam implantation in quartz, by an **annealing** at 1100 °C in an (95% Ar + 5% H₂) atmosphere during one hour to precipitate the excess of silicon in nc-Si.	nc-Si embedded in SiO₂	**TEM** / cross section	1.5; 2.4	Ar$^+$-laser at 488 and 514 nm, 127 mW	793; 814
Franzò *et al.* (2001)	**Ion implantation in SiO₂**	Condensation of a silicon suboxide SiO$_{x<2}$ films, produced by ion implantation in quartz, by an **annealing** at 1100 °C in N₂ during one hour to precipitate the excess of silicon in nc-Si.	nc-Si embedded in SiO₂	**TEM** / plan view	1.8	Ar$^+$-laser at 488 nm, 50 mW	930
Guha (1998)	**Ion implantation in SiO₂**	Condensation of a silicon suboxide SiO$_{x<2}$ films, produced by ion implantation in quartz, by an **annealing** at 900 °C in N₂ for 30 min to precipitate the excess of silicon in nc-Si.	nc-Si embedded in SiO₂	**HRTEM**	2.8	Ar$^+$-laser at 458 nm	773
Guha et al. (2000)	**Ion implantation in SiO₂**	Condensation of a silicon suboxide SiO$_{x<2}$ films, produced by ion implantation in quartz, by an **annealing** at 1100 °C in N₂ to precipitate the excess of silicon in nc-Si.	nc-Si embedded in SiO₂	**HRTEM** / cross section	1.8 – 2.6	10 mW	650 - 825
von Behren *et al.* (1998)	**From porous silicon**	nc-Si result from porous silicon dissolved in a supercritical dried film. The porous silicon are produced by electrochemical etching of crystalline Si and subsequently deposited.	Passivated with Si-O bonds	Raman spectroscopy	2.4±0.6 – 4.3±0.25	He-Cd laser at 442 nm	1.54–1.73